Evaluating and Optimizing Raman Analytical Protocols for CO_2 Fluids

Penny E. Wieser[1*], Charlotte L DeVitre[1,2], Isabelle Susman[1]

[1] Earth and Planetary Sciences, University of California, Berkeley, CA 94270, USA

[2] Now at Department of Earth and Environmental Sciences, University of Ottawa, Ottawa, ON K1N 6N5, Canada

*penny_wieser@berkeley.edu

This paper was resubmitted to volcanica in May, 2026 following 3 helpful reviews.

This is a non-peer reviewed preprint submitted to EarthArxiv.

Please send any feedback to the lead author!

Abstract

Raman spectroscopy is a key method for determining CO_2 densities in geological fluids, yet acquisition, densimeter calibration, and spectral processing methodologies vary widely between laboratories. However, the precision of this method, and the broader applicability of densimeters generated in a single lab, are still debated. This study describes a series of tests to determine how different instrument and acquisition parameters affect CO_2 densities and errors on any given Raman instrument, allowing users to determine analytical best practices for their specific analytical set up. First, we discuss the effect of spectral non-linearity, demonstrating that shifts in the selected acquisition window and the choice of Ne lines used for drift correction can generate a diversity of densimeters even on a single instrument. However, our repeat measurements of natural fluid inclusion (FI) standards over ~3 years yield a 1σ variation of <0.01 g/cm³, indicating that when consistent methodologies are applied to calibration data and unknowns, Raman analyses are highly reproducible over many years. We investigate the play off between peak fitting error and parameters such as acquisition time, laser power, and sample positioning, rebutting recent suggestions that Raman analyses are associated with very large peak-fitting errors. We show that although high laser powers greatly improve signal:noise ratios (and thus peak fitting errors), natural fluid inclusions hosted in olivine show changes in density outside analytical error with increasing powers (density changing by ~0 to 0.09 g/cm^3 per 10 mW of increased power). We show that the amount of heating of the trapped fluid, and thus the change in density, varies drastically based on the absorption coefficient of the host (with melt inclusions and low Fo olivines showing significant more heating than higher Fo olivines). We recommend analyses of fluids withi high optical absorption phases at low laser powers (<3-4 mW), and offer practical strategies to optimize signal without raising laser power, noting that small changes in focus and X–Y position can greatly increase signal intensity.

1. Introduction

Traditionally, the density of CO_2-rich fluids in geological samples have been measured using Microthermometry, a technique in which phase changes are observed during heating and cooling of trapped inclusions. Starting in the 1930s, it was recognised that CO_2 fluid/gas/vapour has a distinct signal when analysed by Raman spectroscopy, with two strong peaks at ~1285 and ~1388 cm^{-1} (Fermi, 1931; McLennan F.R.S. and Smith M.A., 1932). These peaks are collectively called the Fermi diad. For brevity, we refer to the lower wavenumber peak of CO_2 as diad 1 (also v- or 2v2), and the higher wavenumber peak as diad 2 (also v+ or v_1+2v_2). In the 1970s, the distance between the two peaks – referred to as the Fermi diad separation, splitting, peak splitting or diad splitting – was shown to be related to the density of CO_2 (Wright and Wang, 1973). These findings

opened up the possibility of using Raman spectroscopy to quantify the density of CO_2 fluids, an important parameter for many geological research questions (Rosso and Bodnar, 1995).

The relationship between diad splitting and CO_2 density on a given Raman instrument is described using a densimeter, which is typically modelled as a polynomial function of Nth degree. A number of groups have developed experimental apparatus to determine densimeters for different instruments (DeVitre et al., 2021; Fall et al., 2011; Kawakami et al., 2003; Lamadrid et al., 2017; Rosso and Bodnar, 1995; Song et al., 2009; Wang et al., 2019, 2011; Yamamoto and Kagi, 2006, see Supporting Table 1). Not only do densimeters vary widely between Raman instruments (e.g. Lamadrid et al. 2017, DeVitre et al. 2021); changes in hardware on a single instrument have also been shown to affect the densimeter. For example, Lamadrid et al. (2017) show that the densimeter on a single instrument can be shifted by changing the laser wavelength (e.g. a ~0.02 g/cm^3 shift from 514 nm to 632 nm at 2400 g) or the instrument grating (e.g., a 0.02-0.04 g/cm^3 shift from 600-2400 g at 632 nm). They conclude that the same wavelength and grating must be used for calibration and analysis of unknowns.

In contrast, recent work has argued that densimeters may be more universally applicable than previously thought. Remigi et al. (2021) generate a calibration using natural fluid inclusion (FI) standards with densities between 0.37-1.08 g/cm^3 and then compare their densimeter to published densimeters using bootstrapping techniques to better account for uncertainty in densimeter regressions. They suggest that published Raman densimeters fall into two main categories – those collected on instruments with higher spectral resolution (~0.4 cm^{-1}/pixel) and those collected on instruments with lower spectral resolution (~1-1.5 cm^{-1}/pixel). For CO_2 densities > 0.3-0.4 g/cm^3, they show that published densimeters within the high- or low-resolution category are within error of each other. They suggest that because the spectral resolution is related to the ability of a Raman spectrometer to discriminate overlapping bands, and that a change in the spectral resolution shifts peak center positions in a systematic way. They conclude that instrument-specific densimeters may not be required if a densimeter exists for the spectral resolution of interest.

For the remainder of this paper, we refer to the parameter Remigi et al. (2021) term spectral resolution to describe the wavelength range recorded in each pixel as pixel resolution (following Hagiwara et al. 2023). This is not the same as the true *spectral resolution,* which is the smallest width of peak that can be resolved, typically estimated from the full width half maximum (fwhm) of very sharp emission lines such as Ne or Ar, or calcite. These two resolution parameters are not equivalent on many Raman instruments, and there is no simple way to deduce one parameter

from the other. For example, using a 1200 grooves/mm grating (g), the pixel resolution reported by Hagiwara et al. (2023, Table 1) is 0.482 cm^{-1}/pixel while the spectral resolution estimated from the fwhm of the Ne emission line at 1449 cm-1 as 1.59 cm^{-1}. However, using the 1800g, they report a pixel resolution is 0.284 cm^{-1}/pixel vs. a spectral resolution of 0.29 cm^{-1}. In Hagiwara et al. (2020), the 1800g yields a pixel resolution of 0.29 cm^{-1}/pixel but a spectral resolution of 1.1 cm^{-1} estimated from the fwhm of calcite. The vast majority of studies do not report their spectral resolution (Supporting Table 1), which makes it very hard to assess if there truly is a resolution is controlling the densimeter equation.

It is also notable that published densimeters differ the most for analyses of gaseous CO_2 at room temperature (ρ~ 0-0.2 g/cm^3; Lamadrid et al. 2017), while Remigi et al. (2021) only consider densities >0.3 g/cm^3. At low densities, offsets between densimeters can be a factor of 2 or more. This has major implications in igneous petrology, because many melt inclusion vapor bubbles have CO_2 densities below 0.2 g/cm^3 (see Fig. 21 of Wieser et al., 2025). Accurate measurements of these low density vapor bubbles are essential for reconstructing the CO_2 contents of magmas, with implications for determining magma storage depths and the cause of explosive eruptions (Allison et al., 2021; DeVitre et al., 2023b; Moore et al., 2015). However, studies published after the Lamadrid et al., (2017) paper advocating for instrument-specific densimeters still report densities for CO_2 fluids with low densities using calibrations published in other laboratories (e.g. Howe et al., 2025; Venugopal et al., 2020). In this study, we critically evaluate sources of densimeter variability, to evaluate whether generic calibrations based on a simple instrument parameters can replace instrument-specific calibrations.

Another recent discussion of the utility of Raman spectroscopy for quantifying CO_2 densities was provided by Bakker (2021). This work assessed the uncertainties associated with various parts of the Raman method (e.g., peak fitting, instrument drift, etc) and suggested that errors in the position of each diad propagate through to very large errors in diad splitting (±0.26-0.27 cm^{-1}) and thus CO_2 density (~±0.1 g/cm^3). The large quoted errors of Bakker (2021) are in contrast to the very low theoretical errors for analyses of CO_2 within a high pressure optical cell suggested by Yamamoto and Hagiwara, (2024, 0.0005 cm^{-1}, 0.00015 g/cm^3). Thus, it is imperative to evaluate these contrasting statements, and determine the analytical errors associated with analyses of natural melt and fluid inclusions.

Overall, the Bakker (2021) and Remigi et al. (2021) papers demonstrate that while a lot of progress has been made in recent years on optimizing Raman analyses of CO_2 fluids (DeVitre et al., 2023a, 2021; Fall et al., 2011; Lamadrid et al., 2017; Le et al., 2021; Wang et al., 2011), there

are still some fundamental disagreements in the community regarding the applicability of densimeters, and the accuracy and precision of the Raman method when applied to natural samples. In this study, we investigate the effect of acquisition and data processing strategies on the precision and accuracy of CO_2 fluid measurements on a WITec alpha300 R in the Department of Earth and Planetary Science, University of California, Berkeley (hereafter, UCB WITec). We describe a series of tests that readers can apply to their own instruments to guide the development of laboratory-specific best practices, with the aim that this leads to a greater understanding in the community of which sensitivities are instrument and hardware dependent, and which are globally applicable.

2. Methods

We acquire Raman spectra on natural FI and melt inclusions (MI) hosted in olivine using the UCB WITec. The Ultra-High-Throughput-Spectrometer (UHTS600) was calibrated using a Hg-Ar lamp using the WITec control software. The CCD chip (1024X127 pixels) was Peltier cooled to -60°C. We use a green solid-state laser with a wavelength of 532.046 nm, and a Ne lamp in the beam path to correct for instrument drift. For measurements of the CO_2 Fermi diad, the 1800 grooves/mm grating yields a pixel resolution ranging from 0.57- 0.51 cm^{-1}/pixel from wavenumbers of 1042-1592 cm^{-1}. The spectral resolution estimated from the width of Ne lines is ~0.75-0.86 cm^{-1} (Supporting Fig. 1). To convert diad splitting into CO_2 density, we use the densimeter developed for our instrument by DeVitre and Wieser (2024) using a gas cell calibration device (adapted from DeVitre et al. 2021). This calibration line is valid for CO_2 densities spanning 0.0096-1.04 g/cm^3.

The laser was focused on the sample with a variety of objectives depending on the sample size and heating set up; an Olympus 40X objective (0.6 NA, 2.7-4 mm working distance), a Zeiss 50X objective (x0.55NA, 9.1 mm working distance), or a Zeiss 100X objective (0.95 NA, 4 mm working distance). Laser power was controlled using the WITec TruePower module, which measures the laser power in the optical fiber, and allows the user to enter values between 0-50 mW with ±0.1 mW precision. We independently verify the laser power after it has left the fibre optic and passed through the optical head using a ThorLabs S121C sensor attached to a PM100D2 optical power meter. There is a strong linear correlation between the measured power through different objectives, and the instrument TruePower, with intercepts close to 1 (Supporting Fig. S2). Placing the power meter at the opening of the objective turret with no objective screwed in yields laser powers that are 85% of the TruePower value. For the 5-100X objective, we measure the power by focusing on the laser power meter in the normal sample position (i.e. after passing through 1

cm of air). This yields powers that are 80% (5X), 79% (20X), 77% (40X), 62% (50X) and 43% (100X) of the TruePower value (Supporting Fig. S2). Unlike our previous work examining the effects of laser power which report TruePower values (DeVitre et al., 2023a), in this study all subsequent mention of laser power uses the laser power at the sample, calculated using the correction factors mentioned above:

$$Power_{sample} = Power_{TruePower} \text{ X loss} \quad \text{[Eq 1]}$$

For example, if we set the TruePower value to 10 mW in the software, we report a power of 4.3 mW for 100X (10X0.43). This allows greater comparison between studies performed on different instruments.

Various methods were used to heat samples above the critical temperature of CO_2 to ensure a single homogenous fluid was being analysed (DeVitre et al., 2023a). For most analyses, samples were placed on a glass slide in crystalbond and placed on a Peltier heating stage mounted within a custom aluminium holder with a central hole for transmitted light illumination (Supporting Fig. S3). Temperature was monitored using a type K thermocouple taped to the slide with electrical tape. The voltage to the peltier plate was adjusted to yield a sample temperature of 37 °C, matching the gas cell calibration temperature for this instrument (DeVitre and Wieser, 2024). When sample temperature was being directly investigated (Section 3.6), crystals were double polished and placed in a Linkam THMSG600 stage (Supporting Fig. S4). To achieve the long working distance required to see through the stage lid, we initially made measurements using the LWD 40X Olympus objective with a cover slip correction collar. After doing tests with and without the top lid, we found that the stage lid cut out ~50% of the signal, and that there was no difference in sample heating between heating series performed with and without the stage lid (Supporting Fig.S5). Thus, later analyses were performed using the Zeiss 50X objective without the stage lid, but with the small silver cap still placed on top of the sample to help with temperature stability (Supporting Fig. S4).

All peak fitting and data processing was performed in the open-source Python3 tool DiadFit (Wieser and DeVitre, 2024) using psuedovoigt peaks, except when investigating peak fit shapes. Versions <v1.0.18 of DiadFit prior to March 2026 use an unweighted least squares routine to fit peaks, resulting in each pixel contributing equal weight to the fit. As part of this work, we revise DiadFit (>v.1.0.19+) to use weighted least squares, with weights assigned to each pixel proportional to the inverse square root of the background-subtracted intensity, consistent with the expected errors from Poisson counting statistics. Uncertainties in peak fit parameters are

estimated from the covariance matrix, with the lmfit option scale_covar=True applied to rescale parameter uncertainties such that the reduced chi-squared value is unity. The peak positions do not change within the original uncertainties estimated by v<1.0.18, but the errors on each peak position range from 10 to 80% higher than estimates using unweighted least squares (Supporting Fig. S6-9).

3. Results and Discussion

3.1 Neon line corrections and spectral non-linearity

Instrument drift during a Raman session is commonly assessed using repeated analyses of the spectral emission of Neon generated by a Ne lamp (e.g. DeVitre et al., 2021; Lamadrid et al., 2017. Fig. 1a). Two emission lines bracketing the CO_2 Fermi diad are selected. The theoretical distance between these lines is calculated from the published wavelength of the *observed* emission spectra of Neon in air from the NIST webbook (https://webbook.nist.gov/), converted to wavenumber using the wavelength of the laser outputted by the WITec software (a fixed value for each instrument).

$$\tilde{v}_{line\,1} = 10^7\left(\frac{1}{\lambda_o} - \frac{1}{\lambda_{line\,1}}\right)$$

$$\tilde{v}_{line\,2} = 10^7\left(\frac{1}{\lambda_o} - \frac{1}{\lambda_{line\,2}}\right)$$

Where $\tilde{v}_{line\,1}$ is the wavelength of Ne line 1, $\lambda_{line\,1}$ is the Ne emission wavelength of line 1, and λ_o is the laser wavelength. No vacuum to air conversions were applied to the stated laser wavelength. We note that the choice of laser wavelength cancels out, so knowing this value precisely does not affect the correction factor:

$$\Delta\tilde{v}_{Ne} = \tilde{v}_{line\,2} - \tilde{v}_{line\,1} = 10^7\left(\frac{1}{\lambda_{line\,1}} - \frac{1}{\lambda_{line\,2}}\right)$$

The calculated theoretical distance between two Ne lines is then compared to the measured distance in the acquired spectra. For example, if the theoretical distance between Ne lines is 330.4776 cm^{-1}, and the measured distance is 331.0587 cm^{-1}, the correction factor is $\frac{\text{Theoretical distance (330.4776)}}{\text{measured distance (331.0587)}} = 0.9982$. If the diad splitting was measured at 103 cm^{-1}, the corrected diad splitting would be 0.9982*103 = 102.8192 cm^{-1}.

It has been suggested that the common method of correcting for instrument drift using the distance between two Ne lines (e.g. Lamadrid et al., 2017) does not fully capture the complex non-linearity of Raman spectrometers. Non-linearity arises from the mapping between detector

pixel position and wavelength, which is typically ‘calibrated’ using numerous peaks of known position. On our WITec instrument, this calibration is performed by the WITec control software using a Hg-Ar lamp. Ideally, if spectrometer calibration was perfect, the measured wavelengths of all reference spectrum (e.g. Neon and Argon lamps, benzonitrile, 4-aceamidophenol etc, Liu and Hennelly, 2024) would match the true wavenumbers of these peaks within peak fitting error. However, non-linearity is the norm rather than the exception, and Raman spectra show clear offsets between measured and preferred peak positions, with the offset often varying in linear or sinusoidal patterns as a function of wavenumber (Bakker, 2021; Liu and Hennelly, 2024, Fig. 1b).

We investigate spectrometer non-linearity, and the effect of this non-linearity on instrument drift and calculated densities using data collected on the UCB WITec, and two additional alpha 300R spectrometers at Cornell using data from DeVitre et al. (2021). On the UCB instrument, we first perform 50 consecutive repeated acquisitions of the emission spectrum of Neon. We fit pseudovoigt curves to the 6 major Ne lines within the spectral window for each acquisition using DiadFit. For brevity, we refer to these lines using the calculated wavenumber positions rounded to the nearest integer for the 532.046 nm laser wavelength used in this study (565.66588 nm ≈1117 cm^{-1}, 568.98163 nm ≈1220 cm^{-1}, 571.92248 nm≈1310 cm^{-1}, 574.82985 nm≈1399 cm^{-1} 576.44188 nm≈1447 cm^{-1}, and 580.44496 nm≈1567 cm^{-1}, Fig. 1a, Kramida and Ralchenko, 1999). For the line at 1117 cm^{-1}, we iteratively fit two pseudovoigt functions to resolve the smaller peak on the shoulder. Fig. 1b shows the fitted Ne line position divided by the theoretical position calculated from the laser wavelength (532.046 nm) and the theoretical positions in air. This comparison demonstrates that the spectrometer is indeed non-linear, with the correction factor varying across the acquisition window (Fig. 1b). Spectral non-linearity has been noted as a serious issue when trying to compare spectra collected between instruments, as it persists after performing the wavelength calibration methods built into Raman acquisition software (Liu and Hennelly, 2024).

As Bakker (2021) correctly points out, the 'line segment' Ne correction method assumes that the correction factor at any given point between two lines is the same. They suggest that a ‘bracketing technique’ should be used instead, where a polynomial model is developed to describe how the position of each Ne line deviates from the theoretical position as a function of wavenumber. This polynomial allows a correction factor to be calculated for diad 1 and diad 2. These corrected peak positions are used to calculate the splitting, rather than applying a correction factor to the splitting as in the line-segment method.

The polynomial fit through these correction factors is shown for the 'bracketing technique' (grey curve, Fig. 1c) for a single Ne acquisition. Correcting for the position of the CO_2 diad using this curve this would yield a corrected splitting for the diad position shown by blue dotted lines that would be equivalent to a line segment correction factor of 0.9977. The 'line segment' technique for drift correction can be visualized by drawing a straight line between any two datapoints (circles) on this polynomial curve (Fig. 1c). If the gradient of this linear segment is the same as the gradient of a line drawn between where the x positions of the diad intercept the polynomial, the line segment technique and bracketing techniques would give the same result. The line segment method applied to the 1220-1399 cm^{-1} lines results in a very similar correction factor to the bracketing technique (0.9976 vs. 0.9977). The disadvantage of choosing this pair is that the 1220 cm^{-1} line is relatively small, resulting in larger fitting errors, meaning that correction factors show substantially more variability in each run than using the 1117-1447 cm^{-1} pair (see error bar on Fig. 1c). The 1117-1447 cm^{-1} pair used by our laboratory yields a reasonably similar correction factor to the bracketing technique (0.9982 vs. 0.9977). However, applying the line segment technique to the 1220-1567 cm^{-1} lines (red dashed segment) would result in a Ne correction factor that is far smaller than that determined using the bracketing technique (0.9991 vs. 0.9977), yielding a higher apparent diad splitting ($\Delta_{CO2}^{Corr,brack}$=103.450 cm^{-1} vs. $\Delta_{CO2}^{Corr,seg}$=103.648 cm^{-1}).

The differences in correction factor mean that the choice of Ne line pair does indeed affect the corrected splitting, and the relationship between CO_2 density and corrected splitting (i.e. the densimeter). To demonstrate this, we take the CO_2 and Neon spectra from the analytical sessions used to calibrate the UCB densimeter, which was originally calibrated from corrected splitting calculated using correction factors from the 1117-1447 cm^{-1} line pair (DeVitre et al., 2021; DeVitre and Wieser, 2024, black dotted line, Fig. 2a-b). We reprocess the data using 4 new pairs of Ne lines: ~1220-1447 cm^{-1} (dashed red line, Fig. 2a, c), ~1117-1399 cm^{-1} (dashed blue line), 1220-1398 cm^{-1} (solid cyan line), and 1220-1567 cm^{-1} (solid magenta line, Fig. 2a-b). For each CO_2 spectrum collected on a fluid of known density in the calibration cell, this gives us 5 different corrected splitting values (one for each Ne line pair). Using three polynomial fits for low, medium and high densities (following DeVitre et al. 2021), we calibrate coefficients for 5 different densimeter equations using these 5 sets of corrected splitting values (Fig. 2a-b). Despite being collected on a single instrument using the same calibration dataset, the densimeters differ by up to ~0.08 g/cm^3 simply based on the Ne line pair used for data reduction. To put the magnitude of these offsets into context, we underlay the densimeters collected on a wide variety of Raman instruments (Fall et al., 2011; Kawakami et al., 2003; Lamadrid et al., 2017; Wang et al., 2011,

2011; Yamamoto and Kagi, 2006), colored using the high (grey) and low (salmon) resolution classifications from Remigi et al. (2021). This demonstrates that the variability from a single instrument introduced through the choice of a Neon line pair is as large as the differences between Raman instruments, despite being collected at a single spectral resolution.

If a gas cell apparatus is available for calibration of a specific instrument, the offsets between densimeters determined using different Ne line corrections are only problematic if they yield different results when analysing unknowns. We test whether this is the case using data collected on FI from Fogo volcano collected by DeVitre and Wieser (2024), where there are independent constraints on CO_2 density from microthermometry. We process the FI data using each of the 5 different Ne line pairs (Fig. 2b), generating 5 values of corrected splitting for each spectrum, and input these values into the densimeter corresponding to each Ne line pair (e.g. data reduced using correction factors for the 1220-1399 pair was fed into the 1220-1399 densimeter). To visualize the differences between these data reduction strategies, we subtract the density calculated using each line pair from that calculated using the 1117-1447 pair, which was shown to correlate very well with Microthermometry (DeVitre and Wieser, 2024). The error bar on each datapoint shows the combination of the peak fitting error, drift correction error, and uncertainty on the densimeter. Densities for the 4 other line combinations are within error of the data reduced using the 1117-1447 cm^{-1} line pair. We also overlay lines showing the 1σ uncertainty associated with Microthermometry assuming a 0.1 ℃ and 0.2 ℃ error in sample temperature (Bakker, 2021). This analysis demonstrates that the uncertainties in the choice of data reduction strategies are small, and comparable to the errors associated with the stage temperature when performing Microthermometry.

Repeated acquisitions of Neon lines at UCB in April 2022 and October 2024 shows that the non-linearity response curve shifts up and down with time, but the shape is maintained (Fig. 4a, solid lines). We also tested recalibrating the UCB spectrometer in April 2024 using a Hg-Ar lamp (WITec's default calibration routine), and the same pattern is observed. Thus, while spectrometer non-linearity is clearly significant, and likely introduces diversity in published densimeters, as long as calibration and natural data is processed in the same way, the non-linearity introduces a consistent offset through time, and choice of Ne line will not cause systematic offsets. This stability also means that the bracketing technique is not necessary, and given the additional computation steps, likely results in a larger uncertainty due to the large fitting errors associated with the weaker Ne lines (e.g. 1310 cm^{-1}). However, if a laboratory wishes to change drift correction strategy, they would need to reprocess their calibration data to use the same strategy.

This analysis demonstrates that not only does a densimeter need to be generated for each instrument, but that each densimeter is only valid for a specific detector calibration and drift reduction protocol. Supporting Table 1 shows that a wide variety of calibration and drift correction routines are being used by different laboratories publishing densimeters. This can be expected to generate a wide variety of non-linearity responses, and thus we speculate that a lot of the diversity in measured densimeters in the literature is a result of spectral non-linearity, both in its original effect on the diad splitting, and the compounding effect of the use of a line-segment Ne line correction. It is possible that performing a polynomial fit like that suggested by Bakker (2021) would resolve offsets between densimeters calibrated in different laboratories; extensive testing using different Raman instruments for standards with known densities would be a promising avenue for future research.

3.1.1 The effect of changing the spectral window

The significant non-linearity in the spectrometer response shown in Fig. 1b has other implications for the densimeter equation determined for a given instrument. When setting up a Raman spectrometer, the user must define the wavelength range that is recorded on the CCD. On the three WITec instruments considered here, this is specified by stating the spectral center—the wavenumber at the center of the acquisition window. Along with the grating, this center position determines the range of wavenumbers collected in a single spectral acquisition. Shifting the center means that the photons at a specific wavenumber are collected on a different pixel on the charge-coupled device (CCD) detector within the spectrometer. On other instruments, the window edges rather than center may be the tuneable parameter.

Given the strong spectral non-linearity shown in Fig. 1b, it is worth investigating whether shifting the spectral center affects the measured splitting, because each pixel of the diad would shift to a different part of the polynomial in Fig 1b (see also Bakker 2021). We perform repeated acquisitions on an olivine-hosted CO_2-rich FI from Fogo Volcano with a bulk density of ~0.62 g/cm^3 using different spectral centers. We started at the spectral center used for calibration of the Berkeley densimeter (1325 cm^{-1}), then decreased the spectral center (1325→1320→1275→1250→1225 cm^{-1}, magenta colors, Fig. 3a). To help resolve changes from the spectral center vs instrument drift, we increased (green colors), decreased (yellow colors) and then increased (cyan) the spectral center throughout the day (Fig. 3a). We acquired a Neon line at the same spectral center as each FI measurement to correct each spectra (using the 1117-1447 cm^{-1} line pair). For each individual acquisition, we calculated the corrected splitting using

the Ne line acquired at the same spectral center. Lastly, we calculated density using the UCB densimeter developed using a spectral center of 1325 cm^{-1}.

The uncorrected splitting of the diad increases by ~0.22 cm^{-1} as the spectral center is increased from 1225 to 1350 cm^{-1} (~0.0017 cm^{-1} per cm^{-1} of center shift, Fig. 3b). The change in splitting for spectral center shifts of only ~ 25 cm^{-1} apart is far larger than the variation at a given spectral center throughout the day (e.g. instrument drift). After correcting each acquisition using the Neon line collected at the same spectral center, the change in splitting is smaller, but still notable (~0.15 cm^{-1} across the window, 0.0012 cm^{-1} per cm^{-1} of shift, Fig. 3c). Calculated CO_2 densities after a line segment Ne line correction change by 0.08 g/cm^3 across the window (Fig. 3c), which is far outside the ~0.01-0.02 g/cm^3 uncertainty of the Raman method at the densities of interest (Dayton et al., 2023; DeVitre and Wieser, 2024). Overall, this test indicates that even just shifting the spectral window on a given instrument can generate a new densimeter, and that unknowns must be analysed at the same spectral center/spectral window at which the calibration was performed.

To further illustrate the influence of spectral center, we compare the densimeter developed on the UCB WITec alpha300R with densimeters developed in two laboratories at Cornell University (Cornell Center for Materials Research CCMR and Cornell Mass Spectrometry Facility CMaS, DeVitre et al., 2021). These two laboratories were calibrated with a gas cell that is very similar to that at UCB (following the design of DeVitre et al., 2021), and the Raman hardware for all three instruments is very similar: a ~532 nm laser wavelength, 1800 grating, and Ultra-High-Throughput-Spectrometer UHTS600. All data was reduced with the 565.66588 - 576.44188 nm Neon line pair (corresponding to 1117-1447 for the UCB 532.046 nm laser wavelength). Comparing the fitted neon line positions to the theoretical positions (Fig. 4a) shows that each spectrometer has its own unique signature of non-linearity.

Despite CMaS and CCMR having more similar non-linearity responses, the CCMR densimeter shows the biggest offset in densimeter equation relative to UCB and CMaS. We suggest that this is because the UCB densimeter and the CMaS densimeter were both calibrated using a spectral center of 1325 cm^{-1}, while the CCMR densimeter was calibrated with a spectral center of 1340 cm^{-1}. The absolute difference between these densimeters reaches ~0.04 g/cm^3 (Fig. 4c). Again, these densimeter differences cannot be explained by differences in resolution as advocated by Remigi et al. (2021), because the pixel resolution of all three of these WITec instruments is identical.

3.2 Densimeter stability as a function of time

The above tests make it apparent that small changes in instrument hardware can shift the densimeter. It is interesting to assess whether temporal shifts occur when using identical acquisition conditions and spectrometer settings. We evaluate repeated analyses of internal fluid inclusion standards from Fogo volcano (FG04-A1-4, N=280 and FI FG04-101-A, N=96) collected at the start and end of analytical sessions over 2.5 years. The standard deviation calculated from the 280 repeats on A1-4 is 0.008 g/cm^3 (Fig. 5a) and for the 96 repeats of 101A is 0.0070 g/cm^3. For both inclusions, microthermometry measurements are within 0.01 g/cm^3 of these long-term averages and lie within or extremely close to the 1σ envelope around the mean Raman measurement. Overall, this small deviation and lack of coherent trends with time indicates that at least on the WITec, changes in spectrometer non-linearity does not cause any notable drift in the densimeter, and densimeters are remarkably stable once calibrated. Repeated acquisitions of a natural fluid inclusion in a similar manner to that performed here can be used to assess the point at which the instrument may require a densimeter recalibration.

While the Neon method is clearly robust, even with variations in non-linearity, it is worthwhile to determine whether it actually helps correct for drift between and within runs. Yamamoto and Hagiwara (2024) show that over short timescales (minutes) where drift is not controlled by temperature, periodicity is seen in CO_2 peak positions that is not seen in Ne line acquisitions. We reprocess the repeated FI acquisitions using the median Ne correction factor for all the standard analyses, rather than the correction factor calculated by regressing Ne correction factors as a function of time in each analytical run. The standard deviation of both FIs is extremely similar with and without an analysis-specific Ne correction. Interestingly, for FG04 one outlier is generated using a Ne line correction specific to that analysis that goes away using the average correction factor (Fig. 5a), while the opposite is true for standard FG19_101 (one outlier is generated using the median Ne correction). However, it is noteworthy that after the instrument recalibration in April 24, the Raman was moved to a newly renovated laboratory where the HVAC system yields temperature variations of <±1 ℃ per day, which means temperature variations are minimal, which could explain the small differences between the correction methods. We investigate the ability of line segment Ne line corrections to help minimise drift during larger temperature variations in section 3.3 below.

3.3. Densimeter stability within a single analytical session

It is well know that changes in temperature can cause considerable drift in peak positions, intensities and peak widths during Raman analyses (e.g.,Hagiwara et al., 2018; Inoue et al., 2023; Jakubek and Fries, 2022; Lamadrid et al., 2017; Mestari et al., 1997). For example, Fukura et al.

(2006) track peak positions in ruby and napthalene, showing periodic fluctuations in peak positions of ~ 0.1 cm^{-1} with temperature fluctuations of 0.8 ℃. However, they show that the multiple peaks of Napthalene follow a similar trend, and the difference between two peak positions, which is of most relevance for measurements of CO_2 fluids, is ~8 X smaller than the absolute peak shift. In contrast, Mestari et al. (1997) perturb room temperature by 1-2 ℃ and track the relative positions of different Neon lines and show the wavenumber shifts are not identical for different lines and diverge further as the experiment proceeds. This study also shows that amount of relative wavenumber shift between two lines differs drastically as a function of the acquisition conditions.

Hagiwara et al. (2018) investigate the effect of both room and sample temperature on CO_2 density measurements to isolate the effect of each. They show no notable change in splitting as sample temperature is perturbed by 21-26 ℃, but an abrupt shift in splitting of ~0.05 cm^{-1} as the room temperature is raised by 7℃. The splitting then rapidly shifts back to its original value again. As the authors do not plot splitting against room temperature, it is difficult to determine exactly when this perturbation happens relative to the onset of room heating. They suggest the splitting change reflects thermal expansion induced misalignment of the spectrometer, as thermal expansion of the host mineral will be negligible. The Neon line correction routines of Lamadrid et al. (2017) and Lin et al. (2007) do not mitigate the change in splitting during this perturbation, and suggest that repeated measurement a CO_2 standard may provide a better drift correction strategy.

Given the differential response to temperature Mestari et al. (1997) report using different instrument settings on a single instrument, and conflicting reports of whether different lines moves together (Mestari et al. 1997 vs. Fukura et al. 2006), we investigate the effect of room temperature variations and whether the Ne line segment technique can minimise the effect on measured splitting on the UCB WITec alpha300R. We turned off the room heating and cooling system the night before a day that was forecast to be particularly warm for the San Francisco Bay area (~28-30℃). We started the test at ~ 6:30 am when the laboratory temperature was 23.5 ℃, 30 mins after the laser and Neon were turned on and the spectrometer set to cool, Two Icelandic fluid inclusions (Kahl et al., 2025) were double polished and placed in the Linkam THM600 stage with a silver lid on top of the sample to keep the sample temperature fixed at 37±0.1 ℃ throughout the day. We do not use the top lid of the stage, as it cuts out a large proportion of the Raman signal (see Supporting Fig. S4). As the room warmed up, the two FI were analysed repeatedly, with a Ne line acquisition collected after each measurent of the two FI. Room temperature was

measured using an Aranet4 sensor located on the table with the Raman and Ne lamp (Fig. 6a). At around 3pm, the room temperature had stabilized at around 26 ℃ as the outside temperature peaked. To get a larger temperature rise, a temporary heater was switched on. At 5 pm, the temperature began to level out again, so a second heater was turned on, causing the laboratory temperature to rise to 28 ℃ at ~ 7:30 pm. Two air filters with a combined clean-air delivery rate of 500 cubic feet per minute were used to circulate air within the room to help homogenize laboratory temperature. The laser power recorded by the WITec TruePower stays between 5.95 and 6.2 mW with no obvious correlation with room temperature, showing similar variability to analytical days where temperature is stabilized (Supporting Fig. S11).

The peak positions of the 1117, 1220, 1400, 1447, and 1567 lines increase by ~0.2-0.3 cm-1 over 5℃, which is very similar to the 0.3 cm^{-1} shift of the peak position of GaN observed over 5℃ of room warming by Guo et al. (2020). Interestingly, the proportional change in peak position is extremely similar for all the Ne lines (position at t=i/position at t=0), so the absolute change is largest for the 1567 line and smallest for the 1117 line (Supporting Fig. S12). While the Ne correction factors differ for each Ne line pair, the proportional change in correction factor is within uncertainty for all Ne line pairs (Supporting Fig. S12). This indicates that the magnitude of the drift correction using Ne lines is independent of the choice of line pair.

Given the similar response of all Ne lines and their correction factors, for simplicity, we only discuss the effect of the 1117-1447 line pair. The 1117-1447 correction factor shows a strong anticorrelation with temperature (Fig. 6a, note the flipped y axis for temperature). By parametrizing temperature vs. time and Neon correction factor vs. time using high order polynomials (Fig. 6a), a laboratory temperature and correction factor was calculated for each FI measurement. We calculate the corrected splitting using the Ne correction model (blue line, Fig. 6a) and compare this to corrected splitting calculated using the first Ne acquisition at the start of the day (Ne1, Fig. 6a). Fitting a linear regression for calculated density vs. laboratory temperature yields a far stronger correlation when using a constant Ne correction factor vs. the Ne correction model (0.57 vs. 0.14 for B30, and 0.74 vs. 0.39 for B23). This indicates that during large temperature swings, the line segment Ne line correction does help correct for instrument drift, keeping the rate of change within ~0.01 g/cm^3 for 10 ℃ of laboratory heating, while not using a Ne lamp would generate ~0.03-0.04 g/cm^3 of drift.

In our experience with our hardware and specific analytical protocol, on a day without such extreme temperature perturbations, measuring a Neon line every 40-60 mins is generally sufficient. However, we have found that our Ne line acquisitions have helped us identify days

where the HVAC system was malfunctioning and frequent Ne line acquisitions have allowed us to use the data collected on those days, whereas with less frequent acquisitions we would have had to recollect. Given the differing results reported for Raman temperature sensitivity in the literature, we suggest using room temperature logs to determine typical daily temperature changes in any given laboratory to decide an appropriate interval at which to measure Ne lines. In laboratories with large temperature swings, performing room temperature tests similar to that described here on their instrument can help identify the best drift correction strategy. If other Raman systems behave like ours during temperature pertubations, where very large temperature swings can be corrected using Ne lines so the analytical error only doubles (from an already small value, ~0.01 g/cm^3), this is excellent news for universities who want to conduct Raman measurements but do not have access to temperature-controlled spaces.

3.4 Peak fitting errors

The above analysis shows that developing a densimeter for a specific analytical conditions and drift correction methods is key to remove the large systematic offsets between different densimeters and generate accurate measurements of CO_2 density. Now, we focus our discussion to optimizing the precision of Raman measurements.

Bakker (2021) raised concerns regarding precision, noting the discrete nature of Raman spectra, which comprise x coordinates (wavenumber) collected on the CCD with spacing defined by the grating and other hardware. At each x coordinate, an intensity value is recorded, the magnitude of which is highly dependent on the instrument. Bakker (2021) show that shifting the spectral window one pixel spacing at a time causes a lateral shift in the maximum peak intensity (Fig. 7). They suggest that the error on the peak center is equal to the magnitude of the spectral shift. For two different Raman set ups, they estimate a splitting error of ~ ±0.27 cm^{-1}. A splitting error of ±0.27 cm^{-1} yields an error of ±0.1 g/cm3 using the UCB densimeter. For a typical melt inclusion vapour bubbles with 3% bubble volume, this corresponds to an uncertainty of the amount of CO_2 held in the bubble of ±1111 ppm. When propagated through to calculate saturation pressure, this would introduce uncertainty of several kbar. Similarly, a FI with a density of 0.3±0.1 g/cm^3 corresponds to entrapment pressures spanning 0.5 to 1.25 kbar (Span and Wagner, 1996). Peak fitting errors of the magnitude suggested by Bakker (2021) would render Raman spectroscopy entirely unsuitable for melt and FI barometry, so it is essential to assess these statements.

We obtain the spectra shown in Fig. 18 of Bakker (2021) and fit them with pseudovoigt peaks for the diads and hotbands. These spectra were collected as the spectral window was shifted ~3 cm^{-1} in steps of 0.137 cm^{-1} on a LabRamHR (600 grating, pixel resolution of 0.62 cm^{-1}/pixel). To help

visualize the shift in the maximum y pixel intensity, we vertically stack the acquisitions collected using different spectral centers after normalizing the intensity for ease of visualization (Fig. 7a). The positions of diad 1 and diad 2 do indeed move by significant amounts as the window is shifted (Fig. 7b). Bakker (2021) state that the total error on the splitting is '*by definition, the sum of the uncertainties of the lower and upper band (i.e. peak) of* CO_2', i.e. the amount of shift of each peak. For this dataset, both diad1 and diad2 shift by 0.226 cm^{-1} as the window is moved (red error bar, Fig. 7c), which would yield a total uncertainty of ~0.45 cm-1 following their logic (and 0.32 cm^{-1} propagating errors in quadrature). However, it is crucial to recognise that diad 1 and diad 2 move in the same direction (Fig. 7b), such that the calculated splitting varies very little and shows no systematic change as the spectral window is shifted (cyan diamonds, Fig. 7c). The overall variation in calculated splitting is well within the estimated error combining the peak fitting errors on diad 1 and diad 2 from lmfit in quadrature within DiadFit (Newville et al., 2016). Thus, the splitting errors suggested by Bakker (2021) are overestimated, because shifting the window causes the position of diad1 and diad2 to move in the same direction, with no notable change in the splitting.

Bakker (2021) also suggest that the choice of different probability density functions (PDFs, e.g. Voigt, PseudoVoigt, Gaussian) return different center positions, and that the errors on these parameters are hard to estimate. Fortunately, modern peak fitting packages such as Fityk (Wojdyr, 2010), and peak fit packages in python such as sklearn or lmfit (used in DiadFit, Newville et al., 2016) provide an estimate of the uncertainty on the peak center using the covariance matrix obtained during the peak fitting process. We assess the difference in peak position using different fits for Raman data collected on natural FIs from Fogo Volcano, Cabo Verde and Kilauea, Hawaii (DeVitre and Wieser, 2024). We consider Voigt, PseudoVoigt, and Pearson4 functions, as these were identified as the most physically-plausible peak shapes for CO_2 fluids by Yuan and Mayanovic (2017). Peak positions obtained from different fits overlap within the calculated uncertainty on the peak center (Fig. 8, Supporting Fig. S13). This can be shown more formally, by dividing the absolute difference between models by the fitting error combined in quadrature (Fig. 8c-d). Y values <1 on this plot show that the difference between functions is less than the 1 σ estimated error. This analysis demonstrates that for a wide range of CO_2 densities and signal intensity, differences between physically plausible peak fit shapes are within the stated error on each model, and that quoted peak fitting errors are realistic.

It is notable that the errors on the PseudoVoigt peak position are twice as large for diad 1 as diad 2, consistent with its lower intensity and slightly higher full width half maximum (Fig. 9a). Errors

are also larger at lower CO_2 densities. However, for all inclusions, peak fitting errors are still significantly smaller than the 0.1-0.3 cm^{-1} estimated by Bakker (2021). Comparing Raman measurements with Microthermometry measurements provides another opportunity to assess precision (and accuracy, Fig. 9b). We use data from N=58 FI from Fogo volcano from DeVitre and Wieser (2024) supplemented with N=39 new microthermometry and Raman measurements from the Galápagos using the same methods. The Raman error was estimated from Diadfit, by combining the peak fitting errors with the uncertainty from the Neon line correction model and the densimeter. This error was combined in quadrature with the uncertainty in microthermometry homogenization temperature (±0.2 ℃) to create the y error bar shown in Fig. 9b. On Fig. 9c, we perform the same analysis but now show error bars estimated from multiple repeats of FI analyses, rather than the DiadFit peak fitting error. On both plots, the two FI with the largest offset between Raman and Microthermometry have CO_2 densities very close to critical, where Microthermometry errors are hard to quantify. The majority of inclusions lie within the ~0.01-0.02 g/cm^3 error commonly quoted for the Raman method (red bars, Dayton et al., 2023; DeVitre and Wieser, 2024; Kobayashi et al., 2012; Remigi et al., 2021). In contrast, it is clear that when propagated to density, the splitting errors of ~0.2-0.3 cm^{-1} (grey dotted and dashed lines) from Bakker, (2021) are not consistent with this dataset.

Although the errors estimated from comparing Microthermometry and Raman (Fig. 9), and repeated measurements of standards (Fig. 5) are far smaller than that estimated by Bakker, (2021), it is noteworthy that the standard deviation in density obtained from averaging multiple repeats is about twice as large as the error estimated from DiadFit (using weighted least squares or unweighted least squares, Fig. 9). Similarly, the individual fitting errors on repeated measurements of FI standards (Fig. 5) are about half the total standard deviation in repeated measurements. This indicates that the DiadFit error accounting for uncertainty in peak position, Neon correction models, and the densimeter itself is not the only contribution to the density error. In Section 3.6, we suggest that a reasonable fraction of the unaccounted-for uncertainty comes from the temperature of the sample, and other sources of instrumental variability.

3.5. Optimizing Signals

While the above discussion indicates that peak fitting errors are far smaller than those indicated by Bakker (2021), it is still worthwhile investigating methods to reduce uncertainties as much as possible. This is particularly important for low density CO_2 fluids (i.e. melt inclusion vapour bubbles), where peak fitting errors can approach 50-100% near the instrument detection limit (~0.01-0.02 g/cm^3, Bearden et al., 2025). Peak fitting errors are highly dependent on both the

instrument hardware (e.g., spectrometer efficiency, spectral resolution, read and dark noise from the CCD), analytical conditions (e.g., laser power, acquisition time, number of accumulations averaged), and sample characteristics (e.g., density of CO_2, size of inclusion).

On most instruments, users can adjust the acquisition time (time spent collecting a single spectrum) and the number of accumulations (number of individual spectra that are collected and averaged). We investigate the interplay between these two parameters using a variety of samples with low CO_2 densities (which have the largest peak fitting errors). We collect N consecutive individual acquisitions of variable duration using the 'slow series' option in the WITec acquisition software. This mode keeps the laser on continuously, and collects and outputs spectra every Xs. This is analogous to a single accumulation when run in the regular mode. To simulate the software collecting two accumulations of time Xs, we average the 1st and 2nd collected spectra to get one averaged spectra and then fit that spectra. We then average the 2-3rd acquisition, the 3-4th and so forth. For N=14 acquisitions collected, this yields 13 averaged spectra that we fit (shown as individual dots on Fig. 10a). We also calculate the average and standard deviation of each peak parameter for the 13 averaged spectra. To simulate 3 accumulations, we average the 1-2-3rd spectra, 2-3-4th, and for 4 accumulations, the 1-2-3-4th spectra, 2-3-4-5th spectra etc. Tests were performed for different integration times (30s, 45s, 60s, 90s, 120s and 200s).

Fig. 10 shows a CO_2 capillary tube with a CO_2 density of 60 MPa, corresponding to ρ=0.011±0.011 g/cm^3 (Le et al., 2021). Supporting Fig. S16-S17 shows the same plot for a low density melt inclusion vapour bubble from Mauna Ulu, Kīlauea (Wieser et al., 2019). Each 'averaged spectrum' is shown as a semi-transparent dot on panel a-b, and the overall average for combinations yielding N accumulations is shown as a cross with an error bar. For a single spectra, the errors are smaller for 90s compared with 45s, as expected given the more intense spectra, and higher signal to noise ratio (Fig. 10c vs 11d). The peak fit error for diad1 is about twice as large as for diad 2. The error drops quickly as the number of accumulations is increased, and then the trend flattens out (Fig. 10a-b). In terms of assessing ways to optimize instrument time, it is useful to compare the errors in the context of the total acquisition time (Fig. 10e). There are no clear differences in error outside of uncertainty the same total time for acquisitions 45s or greater. For the two melt inclusion vapour bubbles, 30s acquisitions to return errors that are slightly higher than all other times.

These observations can be understood when considering the factors that influence the uncertainty in the intensity of each pixel collected on the CCD (Hagiwara et al. 2023). The error for each pixel is a function of the shot noise (i.e., the Raman photons being delivered to the detector), dark noise

(arising from thermally produced electrons in the detector) and read noise (introduced during conversion of charge to voltage during readout). Shot noise (${\sigma_{shot}}^2$) is proportional to counts, dark noise (${\sigma_{dark}}^2$) is proportional to exposure time, and read noise is proportional to the number of times the detector is read (i.e., the number of accumulations). Increasing the time spent collecting each spectrum will decrease σ_{shot}, but increase σ_{dark}, while performing more integrations will increase the total contribution from read noise (σ_{read}).

We collect 20 accumulations of 2s, 5s, 10s, 30s and 60s with the laser and room lights off using the WITec slow series option. For each pixel (wavenumber) we calculate the variance after rejection of cosmic rays and then calculate the median variance for all pixels. Plotting this variance (${\sigma_{signal}}^2$) against exposure time yields a straight line (Supporting Fig. S19). We assume that the noise in the signal is given by ${\sigma_{signal}}^2 = {\sigma_{read}}^2 + Dt$, where D is the dark current rate in counts^2 per second. We estimate these parameters from the intercept and gradient of a linear regression. For our conditions, ${\sigma_{read}}^2$~ 5.8 cts^2 per read, and D = 0.014 cts^2 per second (Supporting Fig. S19). Our detector has a gain factor (K) of 2.55, meaning that a measure signal of one intensity unit corresponds to 2.55 electrons. Shot noise can be expressed as ${\sigma_{shot}}^2 = N_{counts}$/K. As shot noise scales with $\sqrt{counts}$ (the noise), and Raman signals increase proportionally with counts and thus t (the signal), the signal to noise ratio from shot noise improves with time following $\sqrt{t}$, and errors decreases proportional to $1/\sqrt{t}$. This means for a theoretically perfect detector with no read or dark noise, the total acquisition time will control the signal to noise ratio, which will be the same for 10s X 6 accumulations as 1X60s. The relatively low read and dark noise from our detector means that for strong signals, this is approximately true. For a single 120s accumulation, with a signal that is 1000 counts above background:

$${\sigma_{Total}}^2 = \frac{N_{counts}}{K} + {\sigma_{read}}^2 + Dt = 1000/2.55 + 5.8 + 0.014*120 = 399.6 \text{ cts}^2.$$

This yields a signal to noise ratio of 50 ($1000/\sqrt{399.6}$). Shot noise accounts for 98.1% of the error, dark noise 0.4% and read noise 1.5%. This is an expected result on modern, cooled CCDs where shot noise dominates (Liu et al., 2018). In contrast, for the same total acquisition time but with n accumulations, if the spectrum was collected for 30s X 4, the signal would be 4* weaker (250 cts), yielding the following errors:

$${\sigma_{Total}}^2 = \frac{N_{counts}}{nK} + \frac{{\sigma_{read}}^2}{n} + \frac{Dt}{n} = 250/(4*2.55) + 5.8/4 + 0.014*30/4 = 26 \text{ cts}^2$$

This yields a signal to noise ratio of 49. Shot noise is 94% of the error, dark noise 0.4% and read noise 5.6%. The small increase in read noise accompanying more accumulations is relatively negligible for strong signals, explaining why the # of accumulations has relatively little influence on the signal to noise ratio, and thus the overall peak fitting error in Fig. 10. However, if we consider now a scenario where the 120s accumulation has a signal only 100 cts above background (e.g. Supporting Fig. S17), a single 120sX1 accumulation has a signal to noise ratio of 14.6 (83% shot noise, 3.6% dark noise and 12.4% read noise) while 30sx4 accumulations with a signal of only 25 cts above background have a signal to noise ratio of 12.5 (61% shot noise, 2.6% dark noise and 36% read noise). If there was no read or dark noise, these signal to noise ratios would be the same. However, for very weak signals, the penalty of multiple accumulations and the associated increase in read noise become significant.

Overall, these equations explain why peak fitting errors declines with $1/\sqrt{t}$ for strong signals, and there is little difference between different combinations of accumulations and acquisition times for the same total analysis time. However, for the very weakest signals, acquisition times of 30s generate noticeably larger errors (Supporting Fig. S16-17). On our system, because of the decline in error following $1/\sqrt{t}$, we find that analysis times beyond about 4 minutes results in rapidly diminishing returns. Longer acquisition times also run the risk of real drift due to changes in laboratory temperature, Raman laser wavelength, and changing sample and focus positioning. As errors will vary as a function of the Raman hardware and characteristics of the samples being targeted (e.g. density, fluid size etc), we suggest that performing these tests on each specific Raman instrument can help inform an analytical strategy and total acquisition time that reduce peak fitting error while remaining cost and time-effective.

3.6 Sample Temperature

It is important to investigate the effect of sample temperature on calculated densities. This has implications for how the sample should be heated during Raman analyses. Heating samples above the critical point of CO_2 (31.1 ℃) ensures that a homogenous fluid can be analysed, which removes issues associated with analysis of a mixture of gaseous and liquid phases (see DeVitre et al. 2023). We use a low cost heating apparatus consisting of a $60 DC power supply, a $41 Peltier plate with a hole in it to maintain the ability to use transmitted light for sample navigation, and a $24 type K thermocouple with a precision of ±2 ℃ attached to the surface of the sample with electrical tape (Supporting Fig. S3). However, the limited precision of type K thermocouples means that the sample may be at 35 ℃ or 39 ℃, even if the display reads 37 ℃. Determining the error in splitting and density that results from this uncertainty in sample temperature is important

to determine whether higher precision thermocouples or a more sophisticated heating apparatus is needed (i.e. a Linkam stage with a precision of ±0.1 ℃).

A number of studies have investigated how sample (and thus fluid) temperature affects diad splitting. Kawakami et al. (2003) measured CO_2-rich FIs with densities of ~1 g/cm^3 in mantle xenoliths and found that splitting stayed remarkably constant between 20-200 ℃ (see their Fig. 10). Thus, they deduce that splitting is sensitive only to density, and is insensitive of temperature. Wang et al. (2011) investigate splitting vs. temperature for a CO_2-rich FI (0.72 g/cm^3) and a H_2O-CO_2 FI (see their Fig. 11). Both these FI exhibit a drop in splitting of ~0.2 cm^{-1} between ~40 and 200 ℃, corresponding to a drop in calculated density of 0.08 g/cm^3. As well as making measurements on natural FIs with specific densities, Wang et al. (2011) also investigated temperature sensitivity using a high-pressure optical apparatus where the analyte CO_2 gas was held at a controlled pressure and temperature. Their acquisitions at 21, 25, 50, 100, 150 and 200 ℃ indicated that Δ decreases for a given CO_2 density as temperature increases (their experiments span densities between ~0.2 and 0.7 g/cm^3).

More recently, Wang et al. (2019) use a high pressure optical cell to investigate the relationship between splitting and density for a pure CO_2 fluid between -20 and 360℃, and pressures of 0.51 to 50 MPa. Their parameterization of how temperature affects splitting is shown in Fig. 11a. We can also calculate the change in density that would occur if the splitting measured on a fluid heated at higher temperatures was converted into density using the 37℃ densimeter (Fig. 11d). This is a scenario which may occur if a natural sample is analysed at a different temperature to the densimeter, because of a lack of heating apparatus, an issue with the thermocouple on a heating apparatus, or the heating of the fluid by the laser itself (see section 3.4). The Wang et al. (2019) model predicts that the effect of temperature is largest for densities of ~0.5-0.6 g/cm^3 (Fig. 11d).

Sublett et al. (2021) also performed analyses on pure CO_2 in a high-pressure optical apparatus at 22 ℃, 50 ℃, 100 ℃, 200 ℃ and 350 ℃, for pressures spanning 10-500 bars. Their parameterization (Fig. 11b) is broadly similar to that of Wang et al. (2019), except it shows a larger sensitivity to temperature at the lowest densities, and the change in calculated density vs. true density is more linear with increasing density (Fig. 11c). Finally, Hagiwara et al. (2021, hereafter H2021) investigate the sensitivity of higher density fluids, using pressures from 7-250 MPa for 23 ℃-200 ℃, yielding densities of ~0.65-1.2 g/cm^3 (Fig. 11c). This confirms the downward trend in temperature sensitivity towards higher densities indicated by Wang et al. (2019).

To assess these model predictions (Fig. 11c), we perform heating tests on natural olivine-hosted FIs with densities spanning 0.4-0.9 g/cm^3 (Fig. 11 d-i). Double polished wafers were placed within a LinkamTHMS600 stage and spectra were acquired with the TruePower meter set to 6 mW for temperatures between 37 ℃ and 70 ℃. Over this temperature window, thermal expansion of the olivine induces negligible volume and thus density changes (<0.1 % following the approach of Hagiwara et al., 2018; see also Yamamoto and Kagi, 2008). To account for the possibility of instrument drift, analyses were run with increasing temperature and then decreasing temperature (2 repeats made at each temperature). We fit a linear regression to temperature vs. apparent density calculated using the UCB densimeter, and extrapolate this regression to calculate the density at 37 ℃ (Fig. 12). For each acquisition, we then subtract this calculated 37 ℃ density from the density calculated from the measured splitting using the 37 ℃ densimeter, and compare this to the prediction of the three models (Fig. 11d, Fig. 12).

As predicted by all three models, heating causes the 37 ℃ densimeter to underestimate the true density, and the density change is largest for FI with densities of ~0.4-0.7 g/cm^3, and smallest for ones at 0.9 g/cm^3. The Wang et al. (2019) model does a very good job of predicting the density change for 6 fluid inclusions (Fig. 11d, Fig. 12).

These temperature-density gradients can be used to assess the uncertainty introduced by measuring the sample temperature. The ±2 ℃ error introduced from the thermocouple plus offsets of 1-2 ℃ we observed based on the type of tape used to stick the thermocouple down and the exact positioning of the thermocouple contributes an additional error of ~±0.0016-0.0048 g/cm^3, (depending on the density of the fluid being analysed). For FG04-A1-A4, the average analytical error calculated in DiadFit is ~0.004 g/cm^3, while the standard deviation of hundreds of acquisitions over many years is 0.0085 g/cm^3. Assuming the worst-case scenario of temperature contributing the full 0.0048 g/cm^3, this leaves a residual error of 0.0057 g/cm^3 unaccounted for. The remaining variability may reflect subtle variations in laser wavelength with time, laser positioning within the sample, and temperature drift which is not fully accounted for by Ne line corrections (e.g. Fig. 6). However, to a first order estimate, peak fitting errors are a good estimate of the uncertainty of Raman analyses within a factor of two, and are certainly not several orders of magnitude too small (c.f. Bakker, 2021).

3.7. Laser Power

These heating tests give us a framework to assess the effect of laser power on CO_2 density. This has been a topic of extensive debate in the literature. Fall et al. (2011) suggest that the laser doesn't heat the inclusion more than a few 10ths of a degree, based on observations that many

inclusions analysed in their laboratory which homogenized during microthermometry at temperatures very close to laboratory temperature still showed distinctive liquid and gaseous phases when analysed by Raman spectroscopy. However, Hagiwara et al. (2021b) simulate laser heating with a numerical model, concluding that even laser powers of 10 mW can cause the temperature to rise tens or hundreds of degrees. Specifically, they show that the absorption coefficient of the host mineral is the most important parameter for determining the amount of heating, because the CO_2 inclusion itself has very little absorption at the wavelengths of the laser. They perform Raman analyses at varying laser powers, and use a thermometer based on hot bands to determine the laser heating coefficient B (℃ per mW of laser power) for FIs in olivine, orthopyroxene, clinopyroxene, spinel and quartz. It is notable how much lower their B values are for quartz (0.010-0.014 ℃/mW) vs. mafic minerals such as olivine (0.02-1 ℃/mW). In their tests, as laser power is changed from 4-14 mW, the olivine FI shows a ~0.02 g/cm^3 decrease in density while the quartz inclusion shows no change outside uncertainty. Thus, while Fall et al. (2011) do not note the host mineralogy of the inclusions they draw their conclusions based on, the inclusion shown in their figure that they reference as evidence for a lack of laser heating is hosted in quartz. If the Fall et al. (2011) observations are from quartz inclusions, they are not in conflict with the results of Hagiwara et al. (2021b) who predict minimal heating for quartz. DeVitre et al. (2023) also demonstrate the effect of laser heating on calculated CO_2 densities through the analyses of olivine-hosted melt inclusion vapour bubbles with densities of ~0.3, 0.5 and 0.6 g/cm^3. They show a clear drop in splitting (and thus density) with increasing power (~0.1 g/cm^3 from 0-20 mW using TruePower readings).

It is vital to determine the effect of laser heating in different samples and bring some consensus to the literature, because it is very tempting to use high laser powers for analysis to obtain strong signals and small peak fitting errors. For example, Supporting Figure. S20 shows the peak fitting error associated with the analysis of FIs and vapour bubbles using laser powers ranging from ~5-35 mW. A laser power of ~5 mW yields a peak fitting error 2-3X higher than a laser power of 35 mW. This reduction in error is highly beneficial for low density samples like melt inclusion vapour bubbles (often 0.02-0.04 g/cm^3), where peak fitting errors can introduce an uncertainty of 20-50% in density, but this is only true if the higher laser powers do not change calculated density.

We perform analyses using TruePower values of ~5 to 50 mW (scaling to <0-30 mW at sample depending on the objective) for 4 olivine-hosted melt inclusion vapour bubbles from Mauna Ulu, Kīlauea (Wieser et al., 2019) and the Cascades (Wieser et al., 2023), and 29 olivine-hosted FIs from Iceland (Kahl et al., 2025), Fogo volcano (DeVitre et al., 2023b), and American Samoa (kindly

supplied by Drew Downs). We also analyse 3 pyroxene-hosted FI from the Galápagos (Gleeson et al., 2025). These MI and FI span a wide range of CO_2 densities (Fig. 13). Microthermometry measurements and broad wavelength scans performed by the studies cited above demonstrate that the vast majority of these inclusions are pure CO_2 (e.g. Fogo and Iceland, DeVitre and Wieser, 2024; Kahl et al., 2025). Some of the Galápagos fluid inclusions show anomalously low freezing temperatures but no other Raman-active peaks, so are inferred to contain small amounts of Raman-inactive noble gases (Gleeson et al., 2025). We also perform power series on the FI and melt inclusion vapour bubbles that were used for heating series (Fig. 14). As for temperature, we analyse each FI with increasing then decreasing laser power.

We also conduct a series of tests to determine if a steady state is reached, given that Hagiwara et al. (2021b) show that the time it takes for an inclusion to reach 90% of its max temperature upon laser heating is 18.5s, and that this time is heavily dependent on the boundary condition. Using the WITec slow series function where the laser remains on during the entire interval, we collect 15 spectra spaced between 5s and 30s, and fit each of these spectra individually. There are no significant and consistent decreases in CO_2 density or changes with increasing # of acquisitions (Supporting Fig. S21). The power series show the area ratio of the sum of the two hotbands relative to the sum of the two diads increases with increasing laser power, providing evidence that the laser is increasing the internal temperature of the inclusion (Supporting Fig. S22). There is no notable change in the hotband to diad ratio during the slow series acquisitions, also indicating that a steady state is reached quickly, and doesn't affect our conclusions regarding heating rates using our typical 45s x5 accumulations.

The vast majority of fluid inclusions show a notable drop in CO_2 density as the laser power is increased (Figure, 13, Supporting Fig. S23-26). We calculate the gradient of a linear regression between the laser power at the sample and CO_2 density, and find highly variable gradients for different samples (~0 to -0.006 g/cm^3 per mW, Fig. 13a). In general, FIs show weaker negative gradients than melt inclusions from the same samples (see also Supporting Fig. S27). However, FIs show great diversity in gradients. One fluid inclusion (FI 101C from Fogo volcano) shows a very large change in density (~0.95 to 0.8 g/cm^3, Fig. 13d). This corresponds to a change in calculate depth of 8 km in the crust. The three Icelandic FI shown in Fig. 12c-e show density change varies from -0.08 g/cm^3 to -0.018 g/cm^3 for a 30 mW change in laser power. The drop in density for B22_1_FIA corresponds to a change in calculated depth of ~ 3 km (Fig. 12c, RH axis). These changes in density are far larger than the uncertainty on each Raman measurement (see error bars, Fig. 12c-e).

Hagiwara et al., (2021b) suggest that the absorption coefficient of the host phase is the most important parameter affecting laser heating. A wide variety of absorption coefficients for olivine have been reported in the literature, making it hard to quantitatively model the heating process. For their laser heating simulations, Hagiwara et al. (2021) use an olivine absorption coefficient of 1.14 cm^{-1} based on measurements of a hydrothermal olivine from the Cola Peninsula, Russia (Fo_{95} Taran and Matsyuk, 2013). In contrast, Chassé et al. (2015) report an olivine absorption coefficient at wavenumbers corresponding to a 532 nm green laser (~18800 cm^{-1}) of 11 cm^{-1} (the Fo content is not given). Other papers have shown that the absorption coefficient of olivine is sensitive to the Fo content, and the crystallographic orientation of the host (Hazen et al., 1977; Taran and Matsyuk, 2013; Ullrich et al., 2002). For example, at 532 nm, a Fo_{90} crystal has an absorption coefficient of ~6 cm^{-1} parallel to a vs. 3 cm^{-1} parallel to b (Ullrich et al. 2002). For Fo_{10}, the coefficient parallel to the b axis is ~97 cm^{-1} and 76 cm^{-1} parallel to c. For comparison, Chassé et al. (2015) show absorption coefficients for basaltic glass and melt inclusions of ~100 cm^{-1} at 532 nm. The order of magnitude higher absorption coefficient of basaltic glass vs. typical igneous olivine forsterite contents (70-90) account for the higher rates of heating seen in melt inclusions vs. fluid inclusions.

We investigate the relationship between heating rates and host forsterite contents for a subset of Icelandic and American Samoa crystals that have had the host chemistry analysed, given the expected increase in absorption coefficient as the olivine becomes more Fayalitic. Our data shows a strong correlation between the measured gradient and the Fo content (Fig. 13b), indicating that the absorption coefficient of the host is strongly controlling the amount of heating. However, olivine chemistry cannot explain all the variability in laser heating rates. Crystal 101 from Fogo volcano contains three FI in the same secondary trail within ~100 µm of each other. FIC experiences a very dramatic drop in density, from ~0.93 g/cm^3 to ~0.75 g/cm^3 over 30 mW of heating (gradient of -0.0053 g/cm^3 per mW). In contrast, FIB experiences no change in density outside of uncertainty (gradient of -0.0001 g/cm^3 per mW), and FIA experiences a minor change, with a gradient of -0.001 g/cm^3 per mW (Supporting Fig. S26). Hagiwara et al. (2021b) show that in addition to absorption coefficient, the host crystal thickness and radius can also affect heating rates, with higher heating coefficients for larger crystals, and lower heating rates for larger host radius. However, these parameters are also the same for these three fluid inclusions. We initially speculated that the extreme heating experienced by FIC may result from its proximity to the surface (~6 µm depth). However, when the crystal was flipped over and a power series was performed from the other side (~68 µm depth), the gradient was almost identical (Supporting Fig. S30). However, 3D mapping reveals that 101C contains carbonate (Supporting Fig. S31). It has

been suggested that microparticles which are not visible optically can enhance the laser heating effect (e.g. Burke, 2001), so it is possible that carbonate is playing this role in this inclusion. The two Icelandic samples that show higher heating than expected based on their Fo contents (Fig. 12b) also contain notable carbonate in 3D maps. However, of the three FI from American Samoa (pink edges, Fig. 12b), the two which follow the gradient-Fo trend defined by the Icelandic samples contain abundant carbonate, while the one with more negative gradients contains no carbonate. The three Mg# 79 pyroxenes also show very variable heating amounts (Supporting Fig. S32), despite the fact these samples are very homogenous and there are no apparent color differences between crystals (Gleeson et al., 2025).

As predicted from the modelling of Hagiwara et al., (2021b), we also note that the gradient depends on the heating apparatus used, which controls the boundary condition by which the crystal loses heat. When FI 101C is heated when embedded in crystalbond on a glass slide, it experiences an even greater heating rate (gradient of ~0.008 g/cm3/mW) than when placed on the Linkam stage (Supporting Fig. S31). Overall, these power series demonstrate that while laser heating can be partially predicted based on the absorption coefficient of the host, the extreme change in density experienced by very specific FI, replicated across different analytical sessions in our lab, is worrying. Given that many melt and FIs are analysed prior to knowing the Fo content (as that is often the final step of measurement) and that we cannot diagnose why a few FI show such extreme heating, this work demonstrates that it is absolutely vital to use low laser powers, as the heating response is currently not entirely predictable. Thus, we recommend each laboratory investigate laser heating using similar tests to those performed here for new sample suites to determine the correct laser power to use, as the heating response is currently not predictable.

Performing laser heating and laser power tests on the same FI within the Linkam stage allows us to estimate the heating coefficient, B (℃/mW of laser power) for this specific apparatus; B values will likely vary depending on the exact mounting mechanism used and the boundary conditions they induce. For each FI, we subsample the power series to be within the range of densities seen in the heating series, and calculate the gradient of density vs. temperature, and density vs. laser power. On Fig. 14 (and Supporting Fig. S34), we adjust the power and temperature scale such that the gradients of the two datasets align. We calculate B as:

$$\text{B } (℃/mW) = \frac{Grad\ (\frac{g}{cm3} / mW)}{Grad\ (\frac{g}{cm3} / ℃)} \text{ [Eq 2]}$$

B value errors were calculated from the error on the gradient of each linear regression calculated from ordinary least squares regression from scipy stats linregress propagated in quadrature. B values mostly span ~0.3-0.7 ℃/mW, although a few exceed 1 (Supporting Fig. S34). This compares to 0.02-1℃/mW from Hagiwara et al. (2021), and ~0.36 ℃/mW from Wang et al. (2024).

3.5. Other strategies to optimize signal.

Having to use low laser powers to minimise heating is a real issue in terms of getting enough signal to minimise peak fitting errors. In addition to optimizing the acquisition times (Fig. 10), it is worth thinking about other ways to optimize signals. Our repeated measurements of FI standards (Fig. 5) not only allow us to track the stability of the densimeter, but also the intensity of signals with time. If the FI standard returns lower peak heights than normal, we analyse a Si chip which yields ~2000 cts for a 10s acquisition when the system is well aligned. We use the oscilloscope feature ('live spectra' on HORIBA) to perform micro adjustments on the pinhole position to enhance laser transmission through the fibre to achieve these counts. We find that these adjustments can easily increase signals by a factor of 2-3. We typically adjust the system every few weeks, although sometimes it goes months with no decline in signal, and other times we have to readjust after a few days. Typically, after HVAC failures where the temperature of the laboratory has fluctuated, adjustments are needed, suggesting this adjustment is required based on thermal expansion/contraction of components. On a mirror-based instrument, mirror alignments will have a similar effect.

Once the system's optics are optimized, it is worth considering the analytical geometry. The depth of the FI within the sample has been discussed in a variety of papers. Frezzotti et al. (2012) note that the depth resolution of Raman spectroscopy degrades with depth in the sample, so it is best to analyse FI within 30 μm of the surface. Burke (2001) states that '*usually one strives to analyse inclusions as near the surface as possible' inclusions deeper than 50 μm start to give problems, especially if their density is not too high'*. To assess the influence of FI depth, we individually ground 3 olivine-hosted FI down, performing analyses after each round of grinding and polishing. We measure the depth by focusing on the surface of the sample in RL, and then focusing down to the melt inclusion. We correct the movement of the Z stage to true depth accounting for the refractive index of olivine ($N_{olivine}$ ~1.7, 1.64-1.67 for Fo, 1.84-1.89 for Fa).

True depth = $N_{olivine}\, Z_{stage\ movement}$ [Eq 3]

We use the WITec autofocus function at each depth. Surprisingly, we find no coherent trends in signal intensity (quantified here using the area of diad 2) or the error on calculated density with

increasing depth in the sample (Fig. 15a, Supporting Fig. 35-37). However, we do find big changes with minor changes in focus at a single sample depth. To demonstrate this, we perform acquisitions at different focuses when the FI was 91.8 μm deep in the sample. We first find the optical focus yielding a sharp inclusion edge (yellow box and spectra, Fig. 15). We then use the WITec autofocus feature at our maximum laser power. This collects spectra for ~3 s at various depths to find the maximum intensity in user-selected spectral window. The z position was ~ 2 μm close to the surface than the best optical focus and yielded very similar signal strengths (black spectra and box). We then used the oscilloscope function to manually scroll through Z positions to find the best signal (pink box and spectra). The 6 focus positions between -14.1 μm and 0 μm all yield optically reasonable images, and yet the signal strength varies by a factor of 3. Interestingly, the blue focus position (+2.3 μm) yields an optically poor image, but still a better focus than the oscilloscope feature found. This comparison clearly demonstrates that focus has far more effect on spectral strength than changing the depth in the sample by ~250 μm (Fig. 15 c-d).

This result was replicated for several inclusions (Supporting Fig. S35-S37). We also find that the signal can vary quite considerably spatially, and small shifts in x-y position can also result in stronger signals. This becomes very apparent when taking 2D transects through and across FI (Supporting Fig. S38-39). We suggest that when signals are weak, the autofocus or oscilloscope feature should be used to investigate different x-y-z positions around the optimal focus. We perform these tests at high laser power (49 mW) for speed, and the drop the power to perform the analyses at the optimal Z position. Variability in signal strength can also be seen by performing 2D and 3D maps of signal intensity.

Conclusions

In summary, we investigate the effect of several instrument parameters and data reduction methods on the accuracy and precision of Raman analyses. Our findings can be summarized as follows:

1. Spectral non-linearity means that the spectral window/center and drift correction method (e.g. choice of Ne and Ar lines) used for densimeter calibration must be replicated when analysing unknowns in future sessions. Spectral resolution alone cannot account for the diversity in published densimeters, shown by the fact even a single instrument can generate a wide variety of densimeter relationships. We instead speculate that densimeter diversity in the literature is likely related to non-linearity, causing the splitting to vary depending on which CCD pixels the CO_2 diad is projected onto.

2. Estimates of peak fitting error from pseudovoigt curves, combined with uncertainty in the Ne line correction model, account for approximately half the scatter seen in repeated Raman analyses of the same inclusion over ~ 2.5 years (~0.004 g/cm^3 for FI with densities of >0.6 g/cm^3). These low uncertainties make suggestions of very large peak fitting errors untenable. The additional 0.004 g/cm^3 of scatter seen in repeated standard acquisitions likely results from uncertainty in the temperature of the sample and room, combined with variations in laser wavelength and other parameters with time.
3. We recommend tracking the density of a single standard during every run to ensure there has been no drift from the laboratory densimeter relationship. These standards also help to track the efficiency of the instrument (e.g. checking the peak heights are as high as previous days), so the user knows when re-alignment is required.
4. In a temperature-controlled laboratory, drift during and between analytical sessions is minimal using an WITec alpha300R Raman. However, when the laboratory temperature is perturbed, the Ne line correction helps to reduce instrument drift by a factor of ~3. Thus, while it is better to have a Raman in a temperature-controlled laboratory, it is not essential. Large temperature swings of +5 ℃ result in an additional uncertainty of <0.01 g/cm^3 if Ne lines are used for drift correction.
5. Laser heating is a significant issue, particularly for materials with higher optical absorption coefficients (e.g., silicate glass, lower Fo olivine). However, variable absorption coefficients alone are not enough to explain the large variability in heating response seen. <4-8 mW of laser power at the sample seems a good way to minimise heating for all but the most strongly laser-heated samples, while still providing sufficient signal to obtain good peak fits.
6. To help counteract the relatively weak signals achieved using low laser powers, the analyst should investigate the play off between uncertainty and acquisition time for their specific instrument. They should experiment with different focuses using an autofocus/live spectra function of the oscilloscope at high power to find the optimum signal within the fluid. Focus has a far larger effect than depth to the fluid within the sample (even at depths of ~250 μm).

We suggest that prior to performing density measurements in natural samples with a Raman spectroscopy set up, users conduct the various tests here to optimize analytical conditions:

1) Choose a spectral window over which to collect data, and if for any reason you want to change this after calibration, investigate the impact of this change on the density of a natural or synthetic FI
2) Use a temperature logger to explore variations in laboratory temperature. If the temperature fluctuates by several degrees, perform repeated analysis of a natural or synthetic fluid inclusion, and test whether the selected drift correction method (Ne lines or repeated standard measurements) minimises this drift or not.
3) Investigate the relationship between laser power and signal using the available power options, and between analytical errors and acquisition time and accumulations
4) For the samples of interest (with their different absorption coefficients), investigate the effects of laser heating to choose a laser power that gives sufficient signal without inducing density changes.

Acknowledgments

PW and CD acknowledge funding from NSF EAR 2217371, EAR 2342156, the Sloan foundation, the Berkeley Rose Hills Innovator Program and the Berkeley Heising Simons Faculty Fellowship. IS was funded through a SURF and Ramsden summer fellowship at UCB. The authors are very grateful to the producers of lmfit, without which this study would not have been possible. We thank Maren Kahl for supplying the Icelandic samples, Drew Downs for the American Samoa samples, and Matthew Gleeson for the Galápagos samples. We are grateful to Alex Bearden for his early contributions to investigating laser heating in some Mauna Loa vapour bubbles. We thank Charles le Losq and two anonymous reviewers for extremely detailed comments and suggestions that greatly improved the manuscript.

Supporting Information

All data and Jupyter Notebooks needed to recreate the figures in this study are provided in the Github repository. We also supply a supporting spreadsheet containing processed data for each figure (e.g. peak fits etc).

PennyWieser/Raman_Best_Practices: Code for Raman best practices paper by Wieser et al.

Author Contributions

PW and CLD conceived the project. PW, CLD and IS collected the Raman data and performed peak fitting. PW wrote the manuscript. All authors contributed to the discussion of ideas and the editing of the manuscript.

Figure Captions

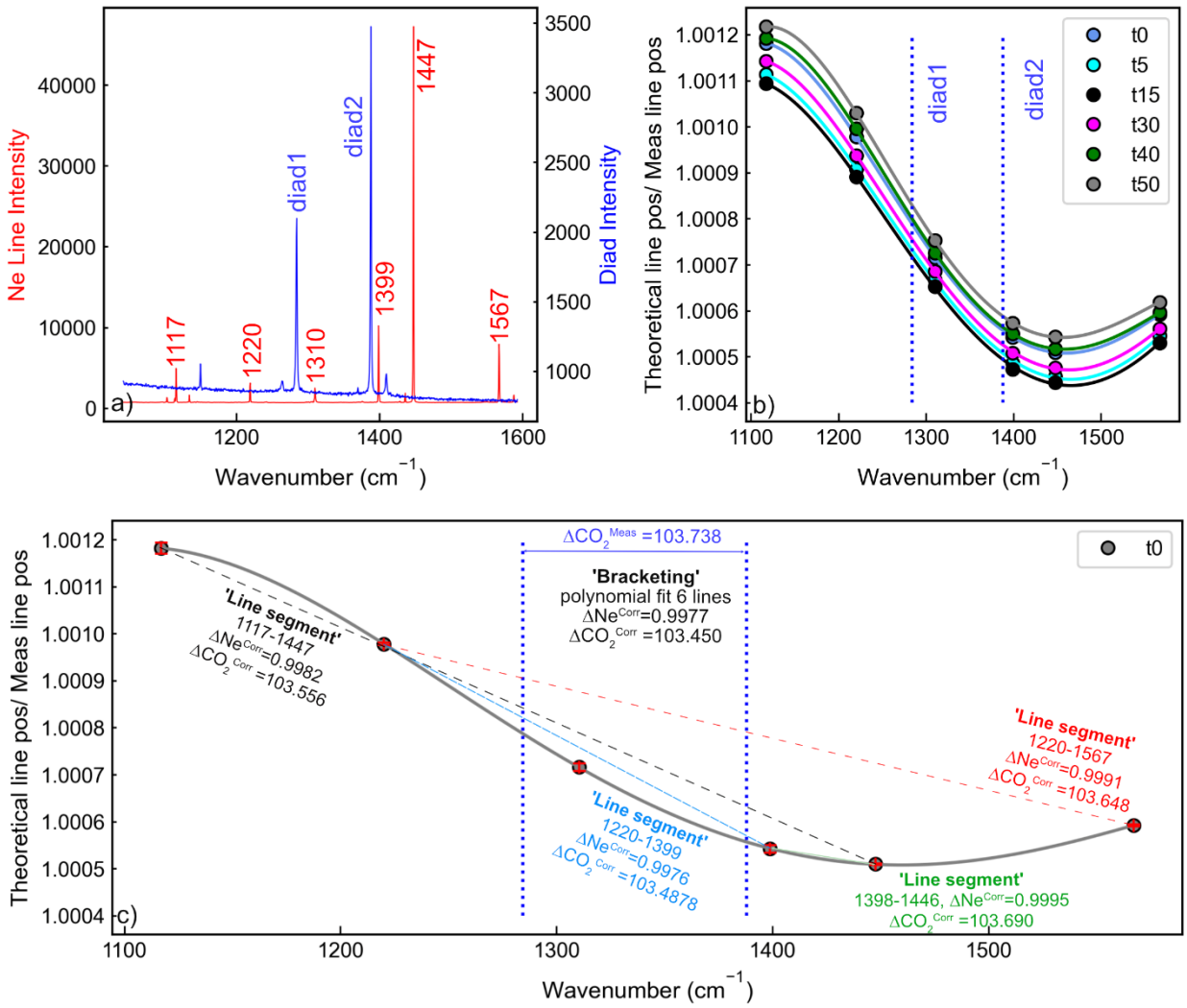

Figure 1 – Examining the difference between the Line segment method and the bracketing method when correcting instrument drift using Ne lines. a) An example Ne line acquisition compared to a diad. Note that the intensity of the Ne (left hand axis) is almost 10X stronger than the diad (right hand axis). This is different from Fig. 8 of Bakker 2021 where Ne lines show very low intensities. b) For repeated acquisitions of Ne lines through the day, the actual peak position is compared to the theoretical peak position. For each line acquisition, a polynomial has been fitted through the data. c) For the first acquisition (t0), we show the polynomial fit through the 6 Ne peaks. The 'Bracketing technique' would correct each diad position based on the value for the polynomial at that wavenumber (where the blue dotted lines intersect the grey line). The 'Line segment' method will give similar results if the gradient drawn between two points is parallel to the intersection of the dotted blue and grey lines.

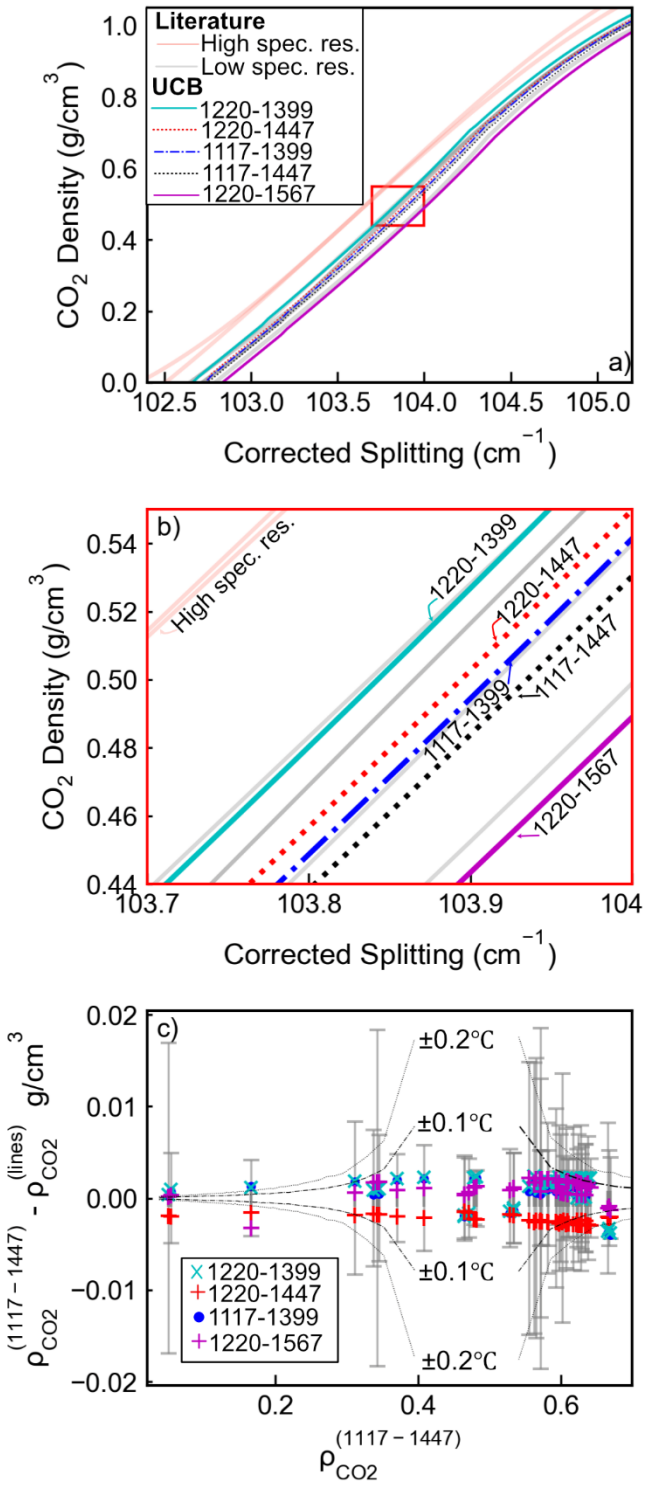

Figure 2 – Assessing the effect of different Ne line reduction routines on densimeters and densities calculated for natural FIs. a) The relationship between corrected splitting and CO_2 density (i.e. the densimeter) was determined using 5 different pairs of Neon lines for the same UCB calibration dataset. This variation is compared to other literature densimeters (grey = high precision, salmon – low precision based on the definitions of Remigi et al. 2021). b) Inset of area in red box in a). c) Natural FI data from DeVitre and Wieser, (2024) was reduced using these different Neon correction routines and densimeters. The y axis shows the difference in density for the default 1117-1447 line option compared with other data reduction strategies. The grey error bar shows the uncertainty on the 1117-1447 density. This demonstrates densities are within uncertainty as long as spectra from unknowns and calibration data are drift-corrected in the same way. For reference, we overlay the uncertainty associated with Microthermometry for ±0.1 and 0.2 ℃ in sample temperature.

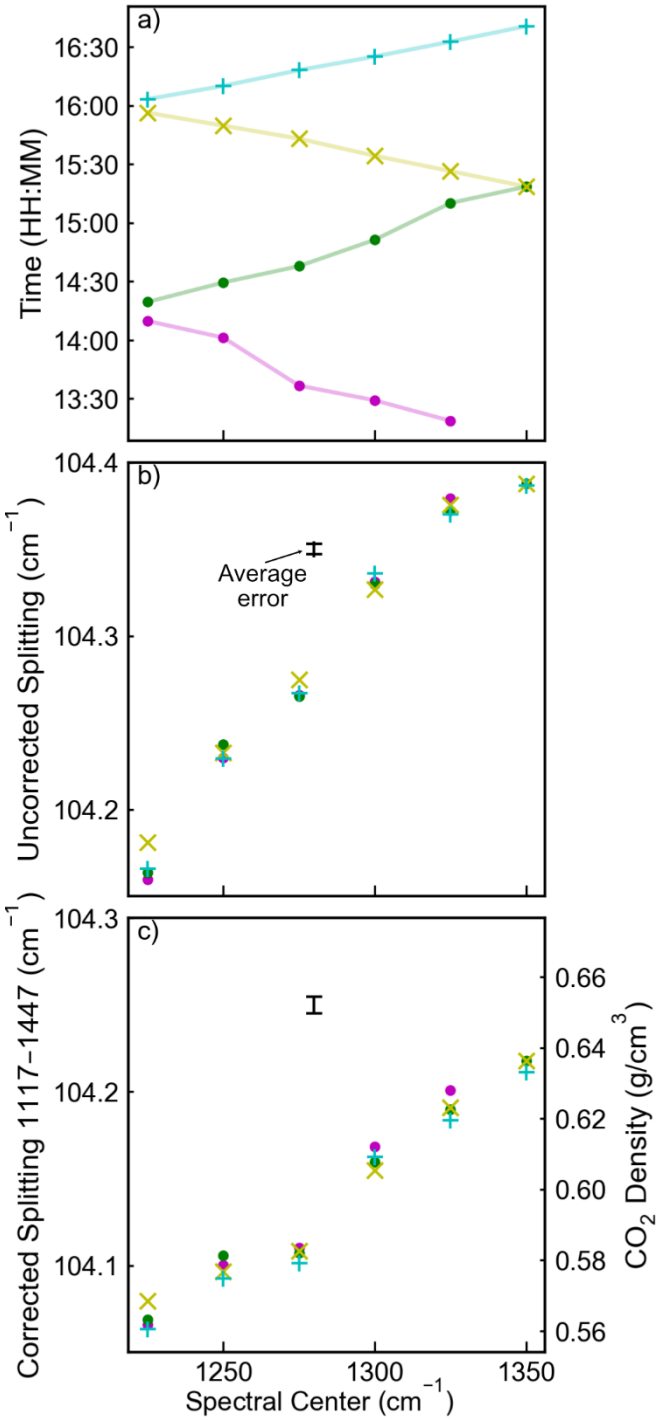

Figure 3 – Change in splitting and calculated density for a single FI as a function of the spectral center. a) The four symbol colors show 'up' and 'down' cycles changing the spectral center as a function of time through the day. b) Uncorrected splitting vs. spectral center and c) corrected splitting, using Ne lines collected at the same spectral center as the diad. The black error bars show a representative error for the splitting (b) and corrected splitting (c) respectively (offset from trend for clarity). The density axis in c is calculated using the densimeter developed for a spectral center of 1325 cm-^{1}.

1065

1066

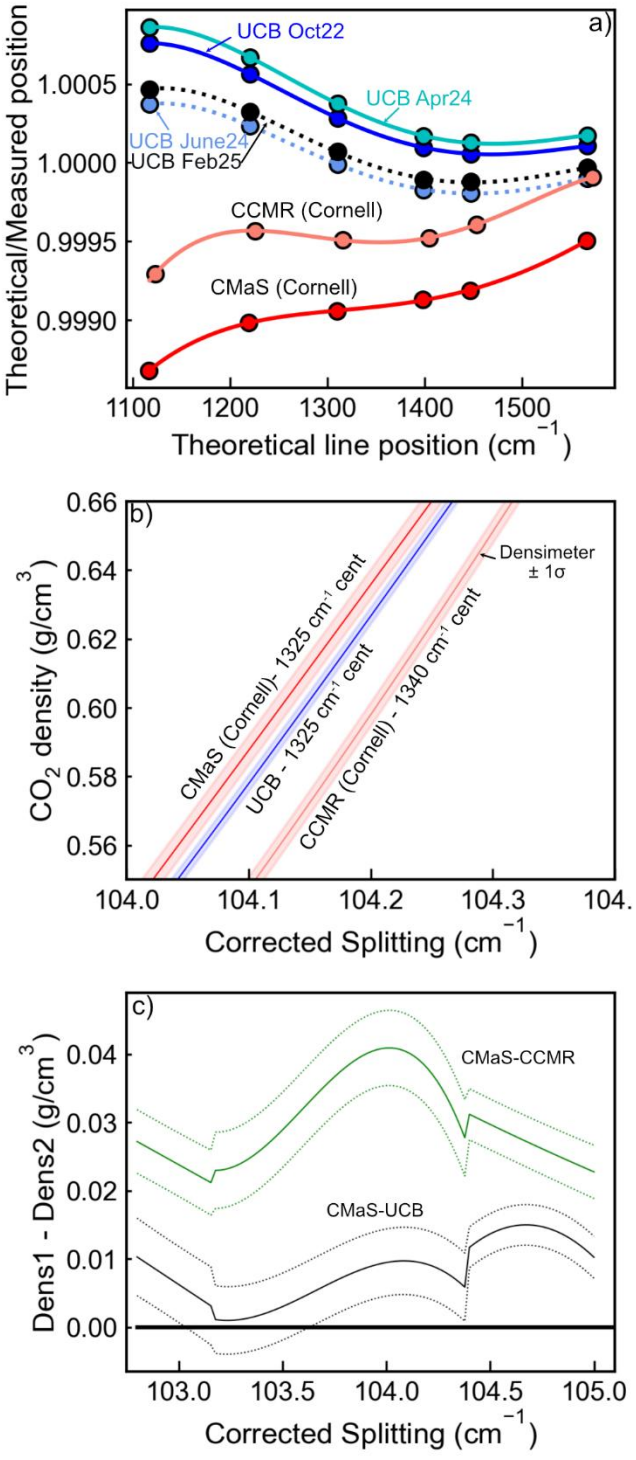

Figure 4 – a) Comparison of spectral non-linearity determined from Ne line acquisitions for three different WITec alpha300R instruments. b) Comparison of the densimeters across a smaller density range showing that UCB and CMaS are more similar than CCMR and CMaS, despite CCMR-CMaS showing much more similar spectral non-linearities (a). c) Difference between densimeters as a function of splitting. The filled lines on b) show the 1σ errors on the densimeter fit, combined in quadrature and shown as dashed lines in c).

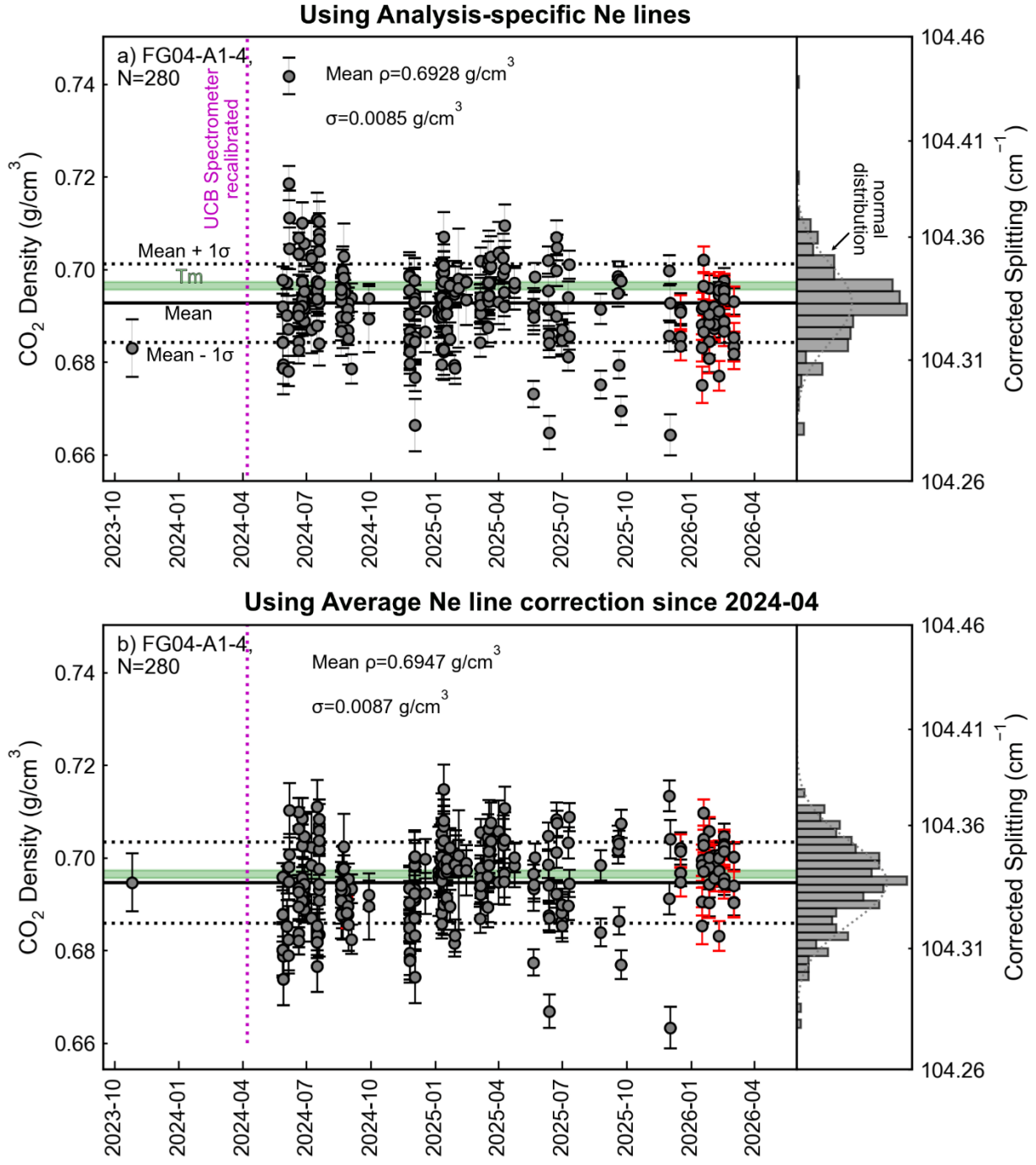

1081

1082 Figure 5- Long-term variability in standard value for FI FG04-A1-4 collected at UCB. a) Data
1083 reduced using a Ne drift correction model for each analytical session. b) Data reduced using the
1084 average Ne line correction factor for all standard acquisitions after the spectrometer recalibration
1085 (marked with a magenta line). The green bar shows the density determined by Microthermometry,
1086 accounting for the uncertainty in the temperature reading of the stage. The black solid line shows

the mean Raman value for the standard, and the dotted black lines ±1 σ. The distribution of densities is shown as a histogram, compared to a normal distribution based on the mean and standard deviation. Supporting Fig. S10 shows the same plot for a second standard run less frequently at UCB. Grey error bars use unweighted least squares, red error bars used weighted least squares routines from newer versions of DiadFit.

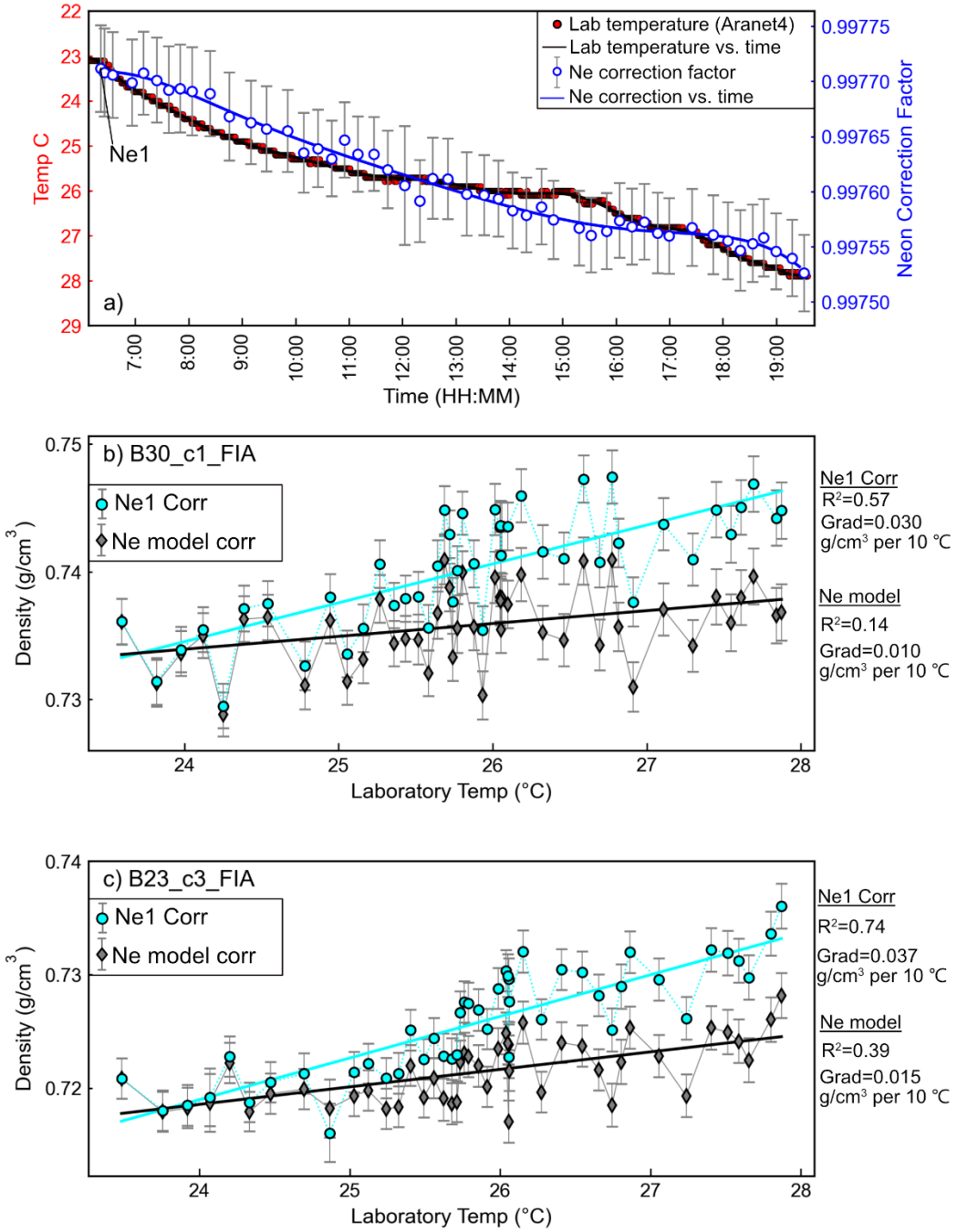

Figure 6 – Testing the sensitivity of Raman acquisitions to large fluctuations in room temperature. a) Temperature log from an Aranet4 logger (red dots) against time. The white circles with blue dots show the Ne correction factor calculated for each Ne line acquisition. These series were fitted with a regression (black and blue lines) to calculate temperature and Ne correction factor for each FI acquisition. b) Change in density of FI B30_c1_FIA as a function of laboratory temperature. The grey diamonds are corrected based on the Ne line correction model (blue line in a), while the cyan circles use the correction factor for the first Ne acquisition (to replicate not applying a drift correction through time). The straight lines represent linear regressions, with the statistics shown on the right. c) Same for B23_c3_FIA. Error bars from weighted least squares fits.

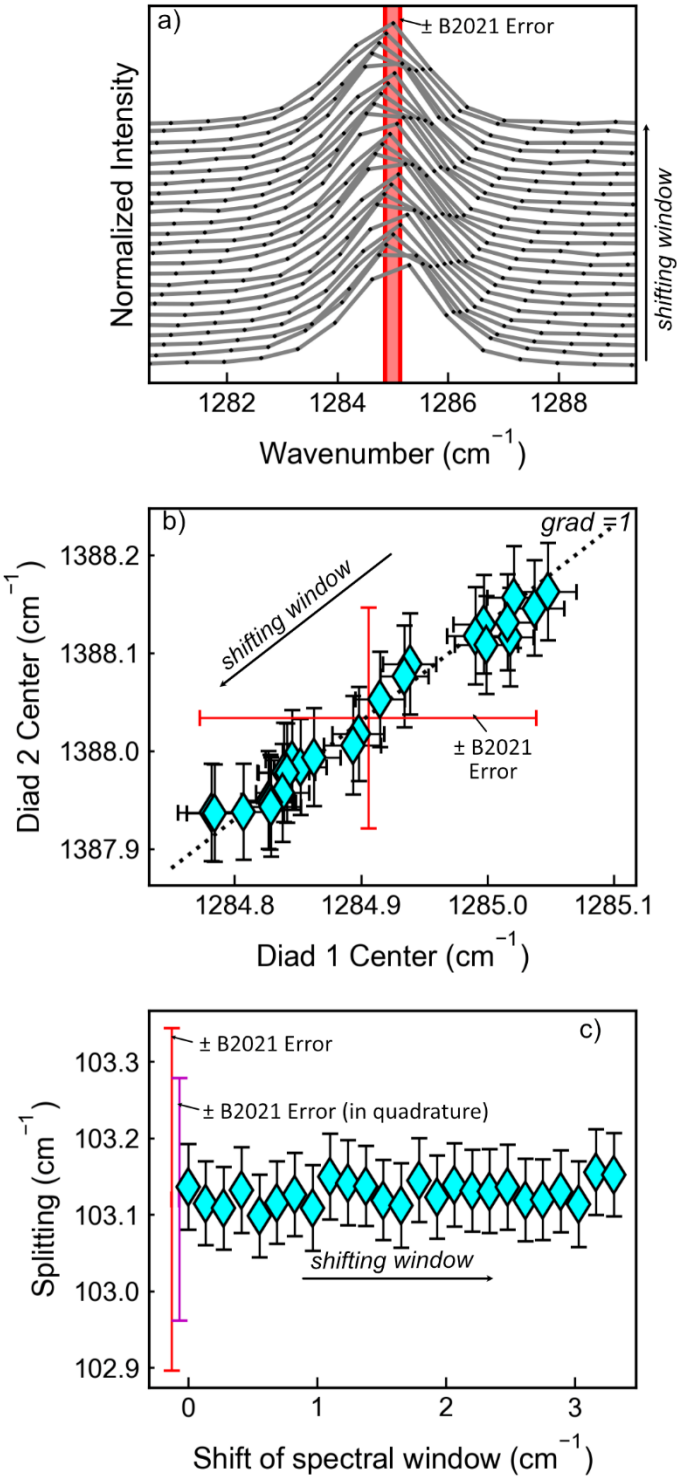

Figure 7 a) Stacked spectra collected as the spectral window was progressively shifted by Bakker (2021). The red band shows their stated error on the peak position, based on the wavenumber shift in the window. b) Plot showing the changing position of diad1 and diad2 for each acquisition shown in a). The black dashed line has a gradient of 1 to emphasize that diad1 and diad2 shift by equal amounts. The error bar shows the 1 sigma error estimated by lmfit from the peak fit c) Change in splitting as a function of the shift of the window. Errors estimated by Bakker (2021) are shown in red, and purple shows their stated error on each peak combined in quadrature. The black error bar

shows the uncertainty based on the lmfit peak positions propagated in quadrature using a weighted least squares routine.

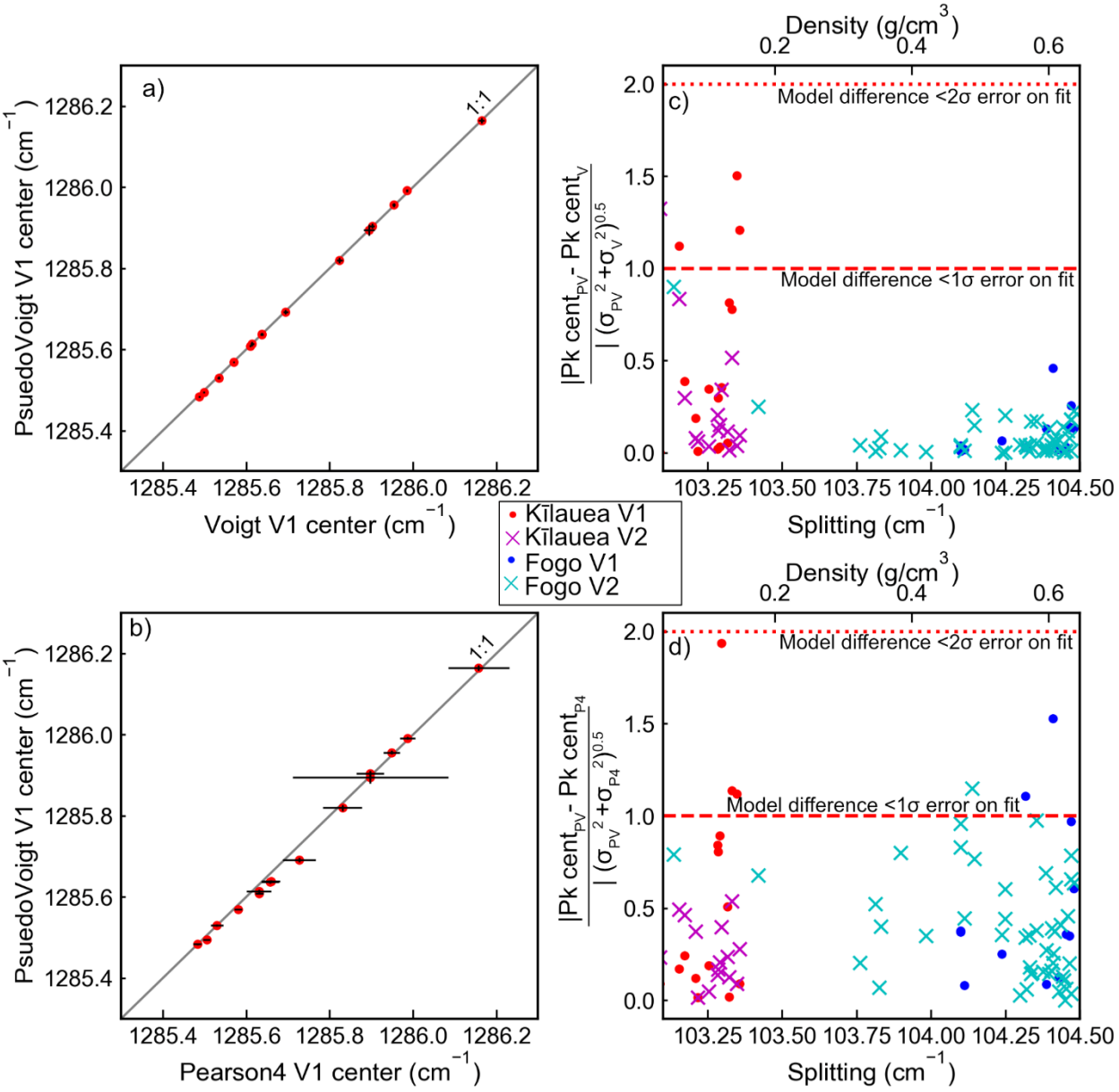

Figure 8 - Comparison of peak centers obtained with Voigt (V), Psuedovoigt (PV) and Pearson4 (P4) peak fits for Diad 1 (V1) and Diad2 (V2) for natural FIs from Fogo and Kīlauea Volcano. a-b) Comparison of Diad 1 position for Kīlauea FI, with errorbars showing the 1σ error on each peak fit from lmfit. c-d) The absolute difference between the peak center for each model is divided by the error on each model combined in quadrature. For datapoints lying below 1, the absolute

difference between the models is smaller than the 1σ on each model. All differences are <2 σ. Comparison of PDF fits for the Fogo inclusions like in a-b) are shown in Supporting Fig. S13.

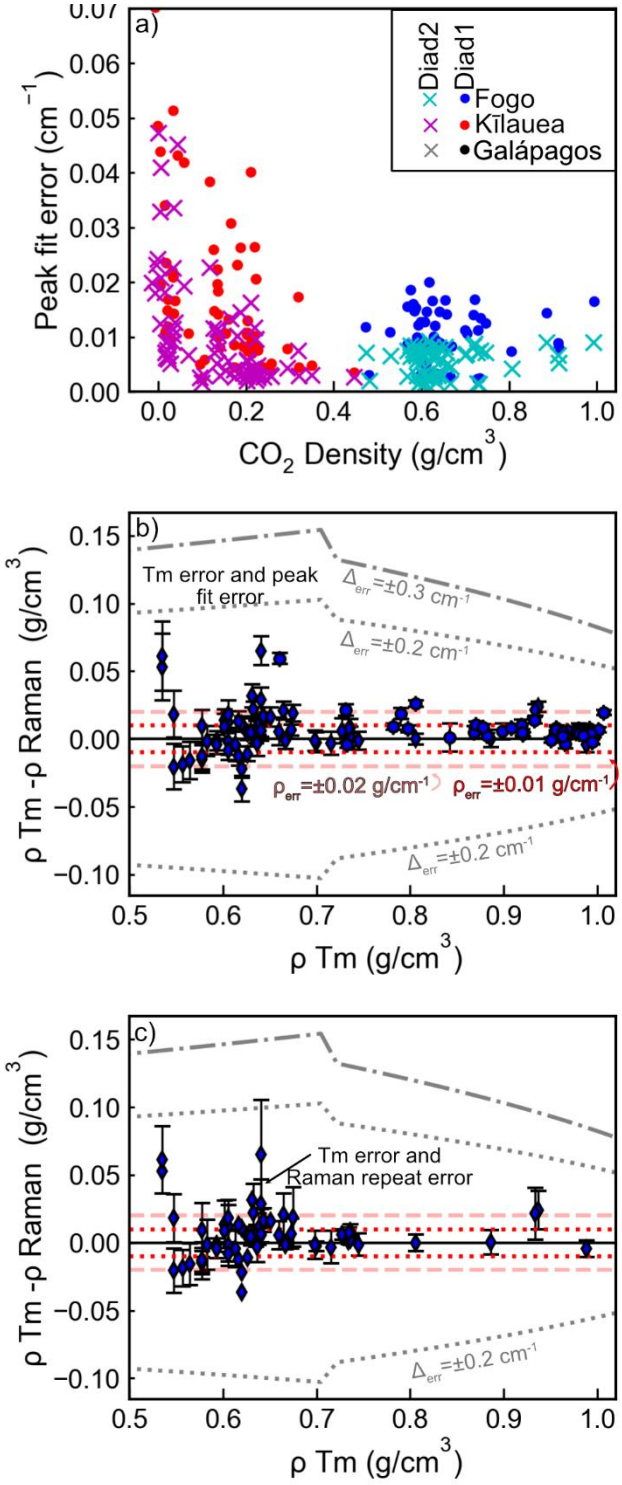

Figure 9 –Assessment of Raman errors using natural FIs with independent density constraints from microthermometry a) Errors on each peak position obtained from lmfit for low and high density FIs from DeVitre and Wieser (2024) from Fogo and Wieser et al. (2025) from Mauna Loa. b) Comparison of densities obtained from Raman spectroscopy and Microthermometry. The error bars show 1 sigma errors estimated from peak fitting, analytical drift and densimeter uncertainty for Raman spectroscopy and Microthermometry combined in quadrature. c) Same comparison but using standard errors calculated from repeated Raman measurements (only FI with repeated analyses are shown). On b-c), we overlay the ±1 σ error bounds that would result from the splitting errors suggested by Bakker (2021). We also overlay red lines showing the ±0.01-0.02 g/cm^3 errors that numerous studies comparing the two methods have stated.

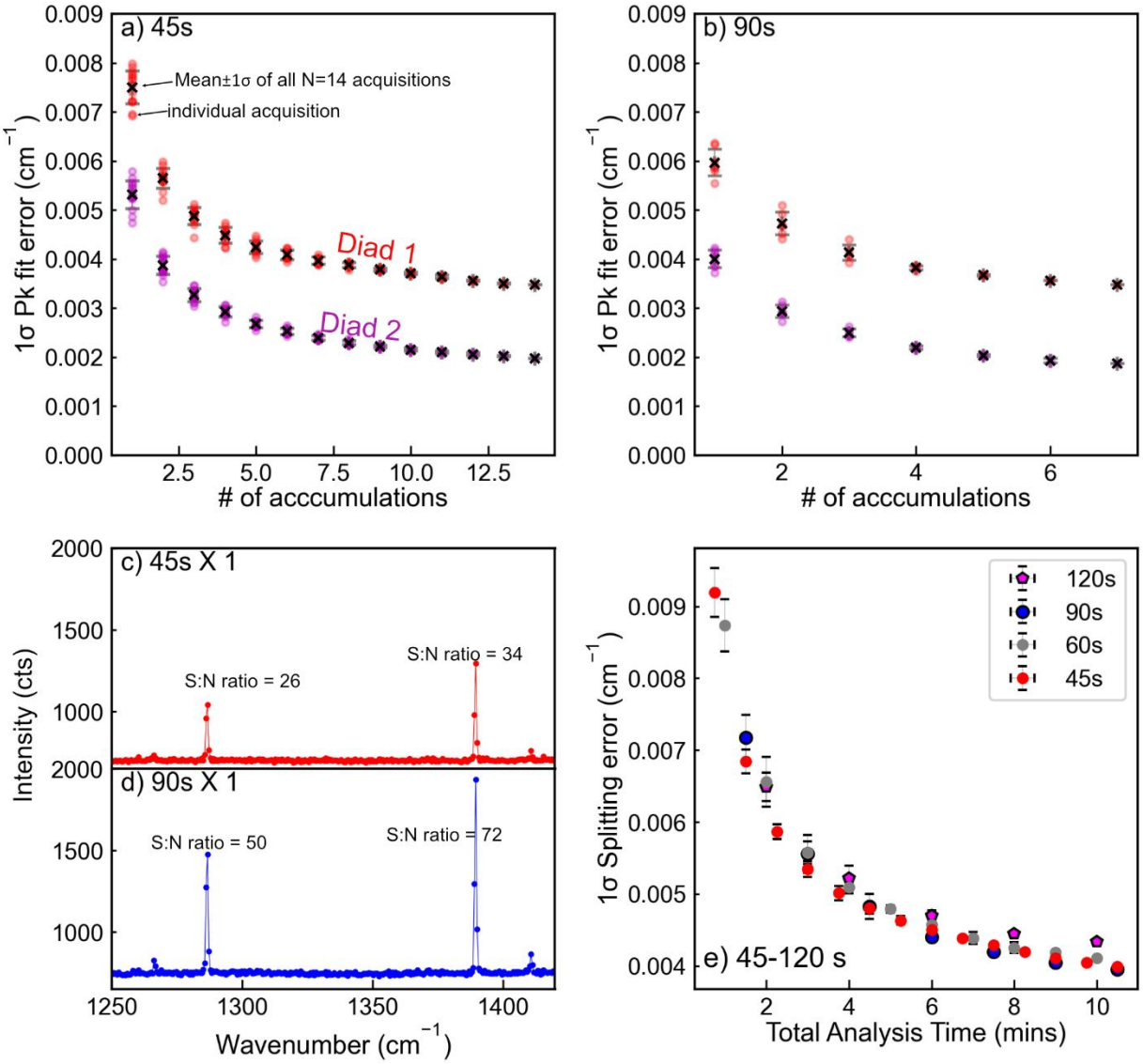

Figure 10 – Investigating peak fitting error as a function of integration time and accumulations using a low density capillary tube (~0.01 g/cm^3, Le et al., 2021). a-b) Error on the peak position of diad1 and diad2 for 45 and 90s acquisitions. The x axis shows the number of spectra that were averaged prior to fitting the peaks (analogous to accumulation). The dots show an individual fitted spectra (e.g. spectra 1 to 14 for accumulations =1, average of spectra 1-2, 2-3 3-4 for n=2 accumulations etc.), and the cross and error bar show the mean and standard deviation of averaged spectra for each number of accumulations (e.g. 14 individually fitted spectra for n=1 accumulations). c-d) Example spectra for 45s x 1 and 90s x 1. The signal to noise (S:N) ratio is calculated as the height of the highest pixel divided by the standard deviation of the region between the two diads. e) Error on peak fitting as a function of total acquisition time. For example, five 120s acquisitions were averaged for the 10 minute total acquisition time. The same figure for a low density melt inclusion vapour bubble is shown in Supporting Fig. 4.

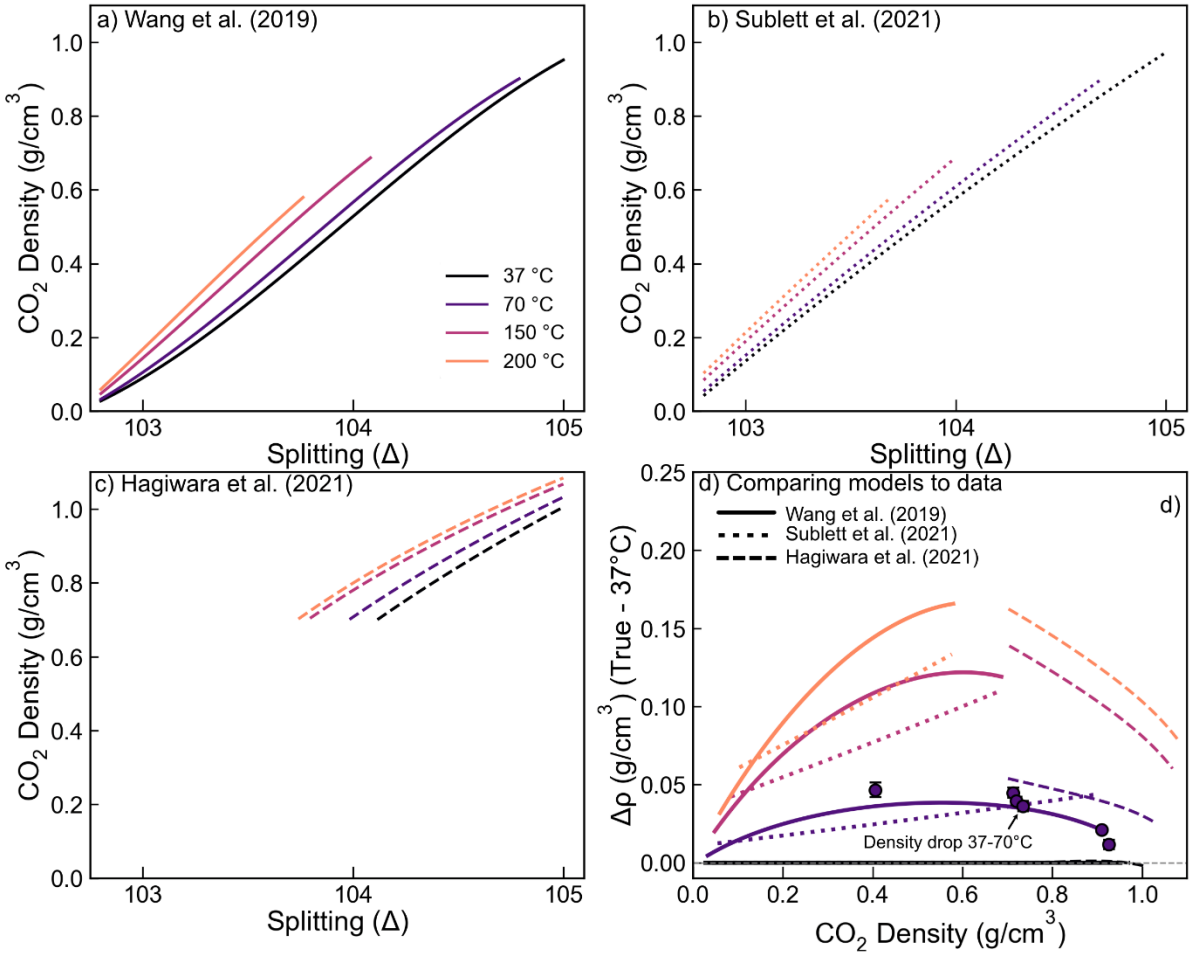

Figure 11 – Models describing the temperature sensitivity of the densimeter. a-c) Relationship between splitting and CO_2 for 4 temperatures calculated using equation 3 of Wang et al., (2019, W19, panel a) equation 8 of Sublett et al. (2021, S2021, panel b) and equation 2 of Hagiwara et al. (2021a, H2021, panel c). Lines are terminated outside the calibration range of each study. d) Difference between true density of a FI and the density calculated using the 37 ℃ when analysed at T=X ℃. We overlay the data from fluid inclusions we analyze at a variety of temperatures (See Figure 12).

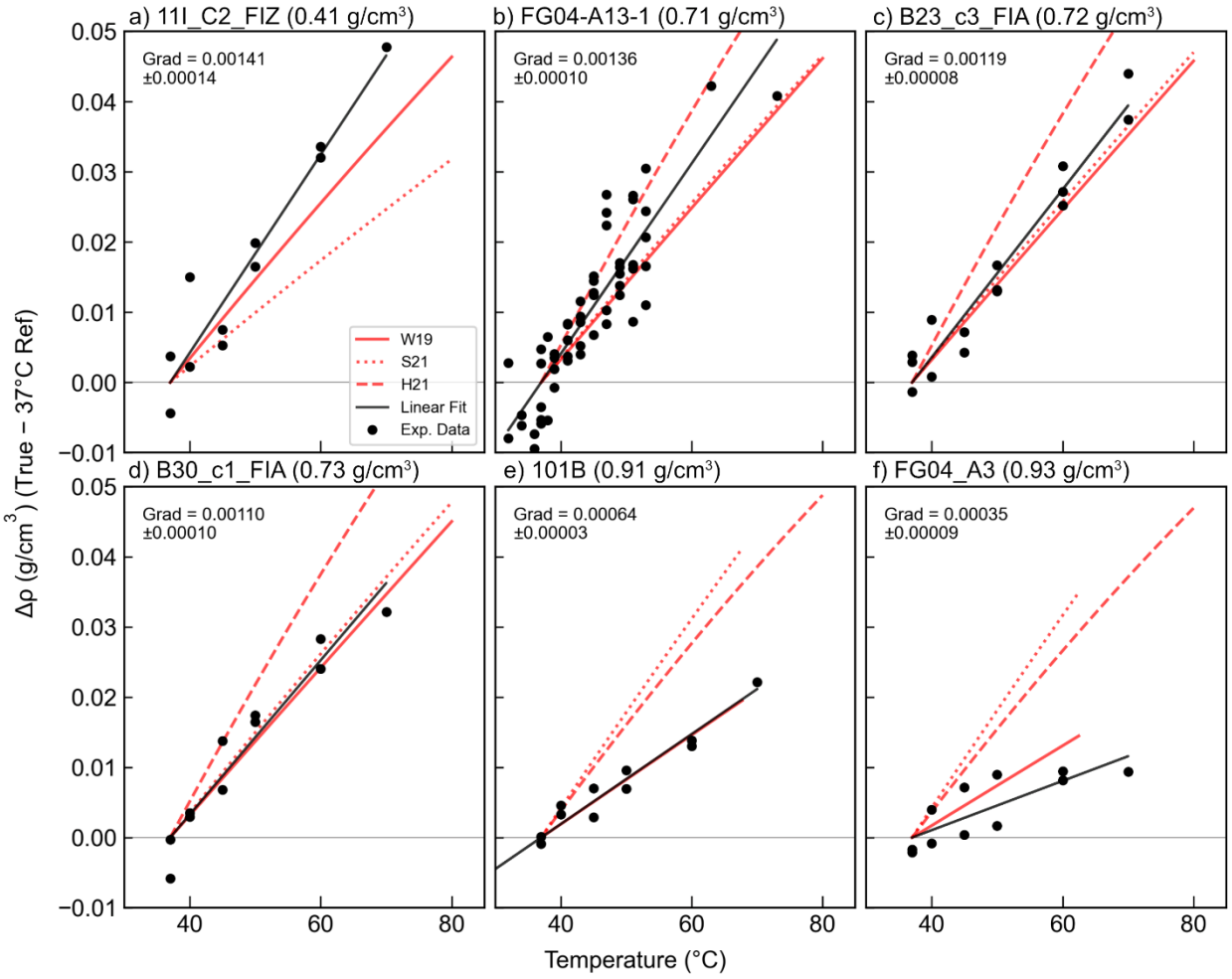

Figure 12 – Changes in apparent density calculated using the 37 ℃ densimeter for fluid inclusions heated in a linkam stage. The 'True' density of the inclusion was determined from a regression between density and temperature, taking the value at 37 ℃ (the temperature of our gas cell calibration). This was then compared to the calculated density at T=X℃ using the 37 ℃ densimeter (i.e. panel a, the density at 70 ℃ was 0.046 g/cm3 lower than the intercept at 37 ℃).

The solid, dotted and dashed lines show the predicted change in density using the models of W19, S21 and H21 respectively. The W19 model provides an excellent fit to all fluid inclusions.

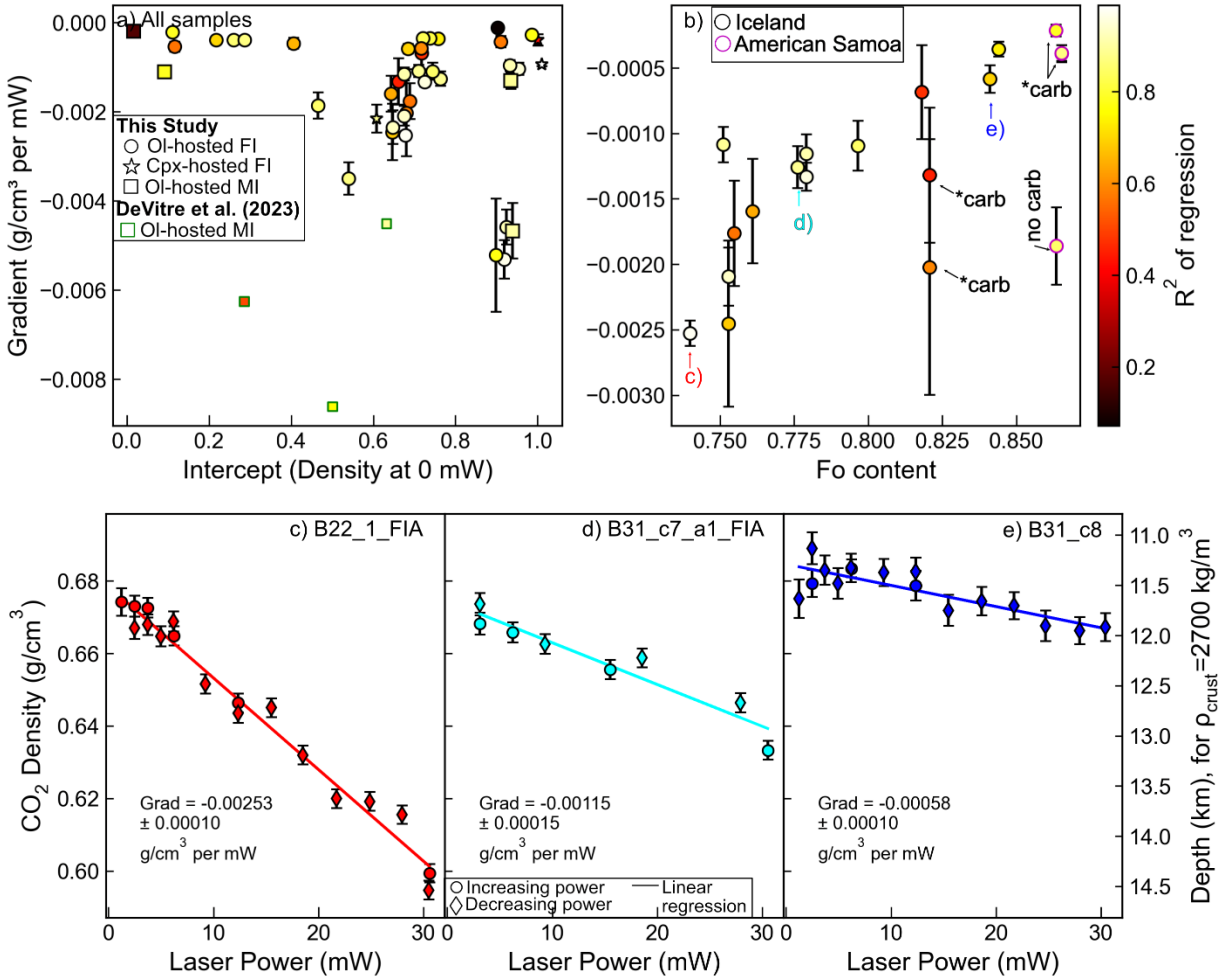

Figure 13 – Relationship between density and laser power at the sample. a) Gradient of laser power vs. density for all the heating tests conducted here (individual regressions shown in Supporting Figures). Symbol shapes show the host mineral and whether the sample is a fluid inclusion or melt inclusion. Squares with green edges show the three melt inclusions from DeVitre et al. (2023) b) Gradient of each power series vs. the forsterite content of the host crystal. FI with a carbonate are indicated with arrows. c-e) Laser power series on three Icelandic FI indicated by arrows in b). The circle symbols show data collected at increasing laser power, and the diamonds at decreasing laser power. The gradients for the best-fit linear regression are shown.

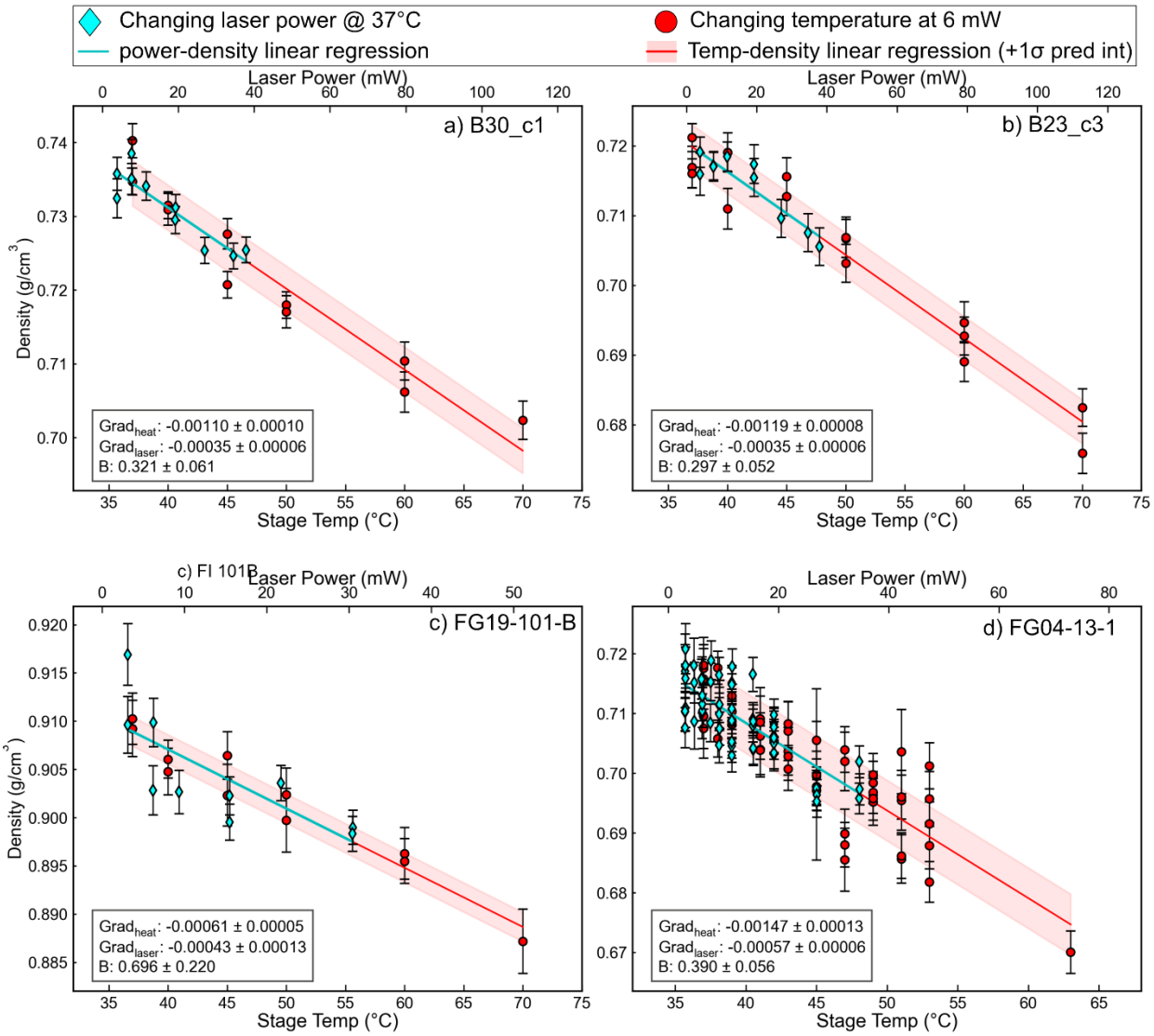

Figure 14 – Comparison of heating and laser power series. For each FI, we perform acquisitions at temperatures from 37-70 ℃ (red circles) at 6 mW, and at laser powers from 6 mW to ~50 mW with the sample temperature controlled at 37 ℃ (cyan diamonds). We adjust the limits of the two x axes such that the gradients of these two data series are identical. The gradient of each series is shown, along with the B value.

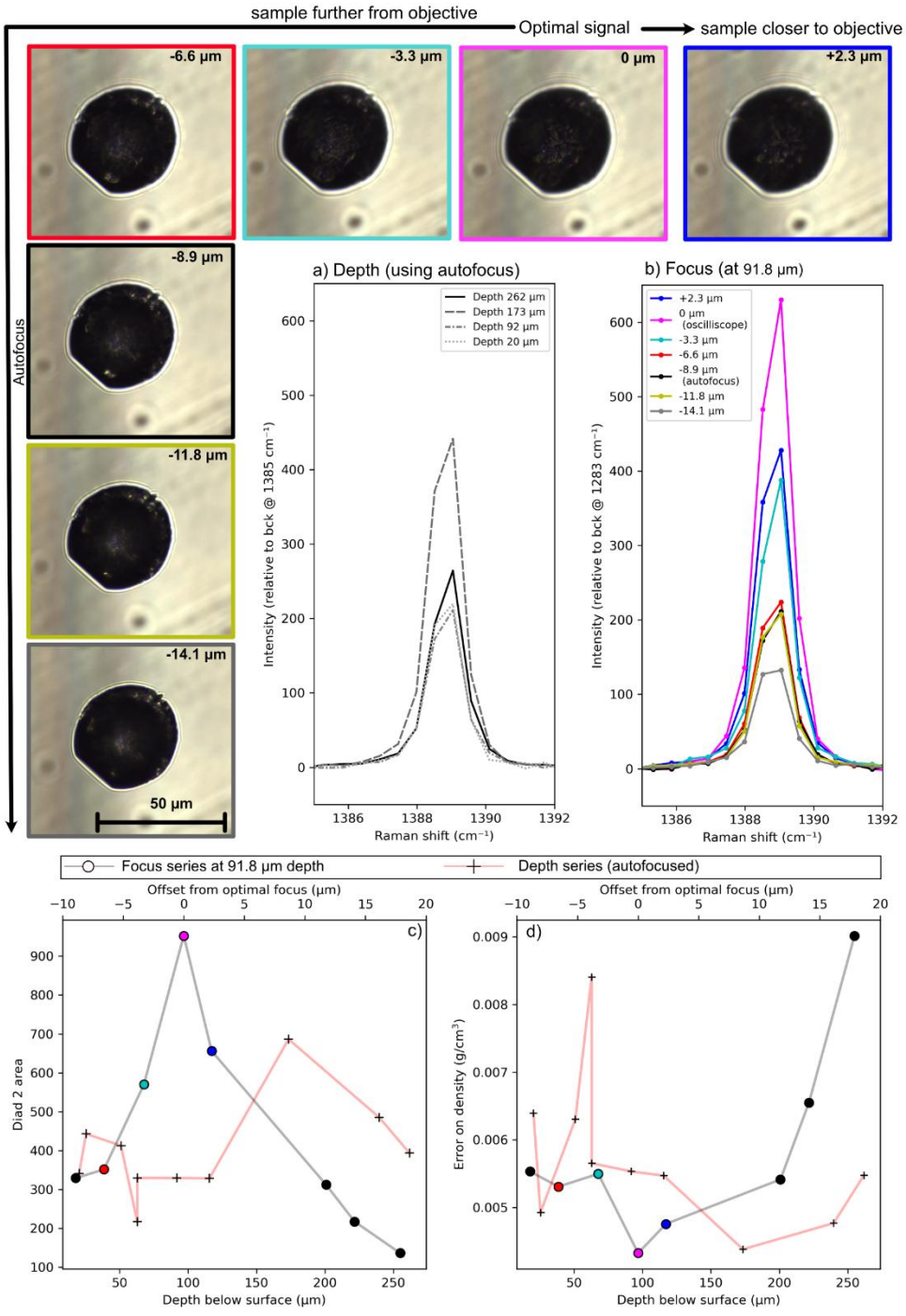

Figure 15 – Investigation of how signal strengths are affected by focus and depth in the sample. a) Spectra near Diad 2, showing the signal strength for different depths of the FI in the sample during serial sectioning. After each polishing round, the autofocus function was used to find the optimum depth. b) When the FI was at 91.8 µm depth in the sample, we acquire spectra at 7 different focus positions. The black spectra and dot represents the focus position found by the

autofocus, and the pink spectra and dot the best focus position using the oscilloscope feature. The images on the left-hand side show what the FI looked like at each focus. c) Change in diad 2 intensity and d) density error as a function of depth in the sample (circles) and focus (crosses).

References

Allison, C.M., Roggensack, K., Clarke, A.B., 2021. Highly explosive basaltic eruptions driven by CO2 exsolution. Nat. Commun. 12, 217. https://doi.org/10.1038/s41467-020-20354-2

Bakker, R.J., 2021. The perfection of Raman spectroscopic gas densimeters. J. Raman Spectrosc. 52, 1923–1948. https://doi.org/10.1002/jrs.6245

Bearden, A.T., Wieser, P.E., Rangel, B., DeVitre, C.L., Gleeson, M.L.M., Monteleone, B.D., Lynn, K.J., 2025. Volatile systematics and magma storage depths at Mauna Loa: a melt inclusion perspective., in: In Chapman Conference on Caldera-Forming Eruptions at Basaltic Volcanoes: Insights and Puzzles from Kīlauea and Beyond. AGU.

Burke, E.A.J., 2001. Raman microspectrometry of fluid inclusions. Lithos 55, 139–158. https://doi.org/10.1016/S0024-4937(00)00043-8

Chassé, M., Lelong, G., Van Nijnatten, P., Schoofs, I., De Wolf, J., Galoisy, L., Calas, G., 2015. Optical Absorption Microspectroscopy (µ-OAS) Based on Schwarzschild-Type Cassegrain Optics. Appl. Spectrosc. 69, 457–463. https://doi.org/10.1366/14-07628

Dayton, K., Gazel, E., Wieser, P., Troll, V.R., Carracedo, J.C., La Madrid, H., Roman, D.C., Ward, J., Aulinas, M., Geiger, H., Deegan, F.M., Gisbert, G., Perez-Torrado, F.J., 2023. Deep magma storage during the 2021 La Palma eruption. Sci. Adv. 9, eade7641. https://doi.org/10.1126/sciadv.ade7641

DeVitre, C.L., Allison, C.M., Gazel, E., 2021. A high-precision CO2 densimeter for Raman spectroscopy using a Fluid Density Calibration Apparatus. Chem. Geol. 584, 120522. https://doi.org/10.1016/j.chemgeo.2021.120522

DeVitre, C.L., Dayton, K., Gazel, E., Pamukçu, A., Gaetani, G., Wieser, P.E., 2023a. Laser heating effect on Raman analysis of CO2 co-existing as liquid and vapor in olivine-hosted melt inclusion bubbles. Volcanica 6, 201–219. https://doi.org/10.30909/vol.06.02.201219

DeVitre, C.L., Gazel, E., Ramalho, R.S., Venugopal, S., Steele-MacInnis, M., Hua, J., Allison, C.M., Moore, L.R., Carracedo, J.C., Monteleone, B., 2023b. Oceanic intraplate explosive eruptions fed directly from the mantle. Proc. Natl. Acad. Sci. 120, e2302093120. https://doi.org/10.1073/pnas.2302093120

DeVitre, C.L., Wieser, P.E., 2024. Reliability of Raman analyses of CO2-rich fluid inclusions as a geobarometer at Kīlauea. Geochem. Perspect. Lett. 29, 1–8. https://doi.org/10.7185/geochemlet.2404

Fall, A., Tattitch, B., Bodnar, R.J., 2011. Combined microthermometric and Raman spectroscopic technique to determine the salinity of H2O–CO2–NaCl fluid inclusions based on clathrate melting. Geochim. Cosmochim. Acta 75, 951–964. https://doi.org/10.1016/j.gca.2010.11.021

Fermi, E., 1931. Über den ramaneffekt des kohlendioxyds. Z. Für Phys. 71(3–4).

Frezzotti, M.L., Tecce, F., Casagli, A., 2012. Raman spectroscopy for fluid inclusion analysis. J. Geochem. Explor. 112, 1–20. https://doi.org/10.1016/j.gexplo.2011.09.009

Fukura, S., Mizukami, T., Odake, S., Kagi, H., 2006. Factors Determining the Stability, Resolution, and Precision of a Conventional Raman Spectrometer. Appl. Spectrosc. 60, 946–950. https://doi.org/10.1366/000370206778062165

Gleeson, M., Wieser, P.E., DeVitre, C.L., Shi, S.C., Millet, M.-A., Muir, D.D., Stock, M.J., Lissenberg, J., 2025. Persistent High-Pressure Magma Storage beneath a Near-Ridge Ocean Island Volcano (Isla Floreana, Galápagos). J. Petrol. 66, egaf031. https://doi.org/10.1093/petrology/egaf031

Guo, X., Mughal, A., Dunphy, D., Stone, G., Miller, D., Huh, S., 2020. Ambient Temperature–Corrected Mechanical Stress Mapping of Gallium Nitride and Aluminum Indium Gallium Phosphide Films by Raman Scattering Spectroscopy for Characterization of Light-Emitting Diodes. Phys. Status Solidi A 217, 1900776. https://doi.org/10.1002/pssa.201900776

Hagiwara, Y., Kawano, T., Takahata, K., Torimoto, J., Yamamoto, J., 2021a. Temperature dependence of a Raman CO_2 densimeter from 23°C to 200°C and 7.2 to 248.7 MPa: Evaluation of density underestimation by laser heating. J. Raman Spectrosc. 52, 1744–1757. https://doi.org/10.1002/jrs.6188

Hagiwara, Y., Sogo, Y., Takahata, K., Yamamoto, J., 2018. Temperature dependence of CO_2 densimetry using micro-Raman Spectrometry at laboratory conditions. Geochem. J. 52, 379–383. https://doi.org/10.2343/geochemj.2.0523

Hagiwara, Y., Torimoto, J., Yamamoto, J., 2020. Pressure measurement and detection of small H_2O amounts in high-pressure H_2O–CO_2 fluid up to 141 MPa using Fermi diad splits and bandwidths of CO_2. J. Raman Spectrosc. 51, 1003–1018. https://doi.org/10.1002/jrs.5865

Hagiwara, Y., Yokokura, L., Yamamoto, J., 2023. Unlocking ultimate precision of intensity and area ratio measurements in Raman spectroscopy: Insights from simulation, experimentation, and theory and implications for isotope ratio analysis. J. Raman Spectrosc. 54, 1440–1464. https://doi.org/10.1002/jrs.6594

Hagiwara, Y., Yoshida, K., Yoneda, A., Torimoto, J., Yamamoto, J., 2021b. Experimental variable effects on laser heating of inclusions during Raman spectroscopic analysis. Chem. Geol. 559, 119928. https://doi.org/10.1016/j.chemgeo.2020.119928

Hazen, R., Mao, H., Bell, P.M., 1977. Effects of compositional variatoin on absorption spectra of lunar olivine. Proc Lunar Sci Conf 8th 1081–1090.

Howe, T.A., Christopher, T.E., Moune, S., Tuffen, H., Schiavi, F., 2025. Melt inclusion bubbles provide new insights into crystallisation depths and CO2 systematics at Soufrière Hills Volcano, Montserrat. Front. Earth Sci. 12, 1509409. https://doi.org/10.3389/feart.2024.1509409

Inoue, Y., Okiyama, R., Hagiwara, Y., Yamamoto, J., 2023. Raman spectroscopic evaluation of precision of oxygen isotope ratio of carbon dioxide. Geochem. J. 57, 92–99. https://doi.org/10.2343/geochemj.GJ23007

Jakubek, R.S., Fries, M.D., 2022. Calibration of the temporal drift in absolute and relative Raman intensities in large Raman images using a mercury–argon lamp. J. Raman Spectrosc. 53, 137–147. https://doi.org/10.1002/jrs.6259

Kahl, M., Morgan, D.J., Wieser, P.E., Bali, E., Guðfinnsson, G.H., Neave, D.A., Walshaw, R., 2025. Crystal-mush remobilization timescales and magma storage depth in the Snæfellsnes Volcanic Zone (W-Iceland): insights from olivine Fe-Mg diffusion chronometry and fluid inclusion barometry. Bull. Volcanol. 87, 118. https://doi.org/10.1007/s00445-025-01892-3

Kawakami, Y., Yamamoto, J., Kagi, H., 2003. Micro-Raman Densimeter for CO_2 Inclusions in Mantle-Derived Minerals. Appl. Spectrosc. 57, 1333–1339. https://doi.org/10.1366/000370203322554473

Kobayashi, T., Yamamoto, J., Hirajima, T., Ishibashi, H., Hirano, N., Lai, Y., Prikhod'ko, V.S., Arai, S., 2012. Conformity and precision of CO_2 densimetry in CO_2 inclusions: microthermometry *versus* Raman microspectroscopic densimetry: Conformity and precision of CO_2 densimetry in CO_2 inclusions. J. Raman Spectrosc. 43, 1126–1133. https://doi.org/10.1002/jrs.3134

Kramida, A., Ralchenko, Y., 1999. NIST Atomic Spectra Database, NIST Standard Reference Database 78. https://doi.org/10.18434/T4W30F

Lamadrid, H.M., Moore, L.R., Moncada, D., Rimstidt, J.D., Burruss, R.C., Bodnar, R.J., 2017. Reassessment of the Raman CO 2 densimeter. Chem. Geol. 450, 210–222. https://doi.org/10.1016/j.chemgeo.2016.12.034

Le, V.-H., Caumon, M.-C., Tarantola, A., 2021. FRAnCIs calculation program with universal Raman calibration data for the determination of PVX properties of CO2–CH4–N2 and CH4–H2O–NaCl systems and their uncertainties. Comput. Geosci. 156, 104896. https://doi.org/10.1016/j.cageo.2021.104896

Lin, F., Bodnar, R.J., Becker, S.P., 2007. Experimental determination of the Raman CH4 symmetric stretching (v1) band position from 1–650bar and 0.3–22°C: Application to fluid inclusion studies. Geochim. Cosmochim. Acta 71, 3746–3756. https://doi.org/10.1016/j.gca.2007.05.016

Liu, D., Hennelly, B., O'Neill, L., Byrne, H.J., 2018. Investigation of wavenumber calibration for Raman spectroscopy using a polymer standard, in: Berghmans, F., Mignani, A.G. (Eds.), Optical Sensing and Detection V. Presented at the Optical Sensing and Detection, SPIE, Strasbourg, France, p. 79. https://doi.org/10.1117/12.2307574

Liu, D., Hennelly, B.M., 2024. Wavenumber Calibration Protocol for Raman Spectrometers Using Physical Modelling and a Fast Search Algorithm. Appl. Spectrosc. 78, 790–805. https://doi.org/10.1177/00037028241254847

McLennan F.R.S., J.C., Smith M.A., H.D., 1932. Raman effects with liquid and solid carbon dioxide. Can. J. Res. 7, 551–555. https://doi.org/10.1139/cjr32-104

Mestari, A., Gaufrès, R., Huguet, P., 1997. Behaviour of the calibration of a Raman spectrometer with temperature changes. J. Raman Spectrosc. 28, 785–789. https://doi.org/10.1002/(SICI)1097-4555(199710)28:10%253C785::AID-JRS148%253E3.0.CO;2-D

Moore, L.R., Gazel, E., Tuohy, R., Lloyd, A.S., Esposito, R., Steele-MacInnis, M., Hauri, E.H., Wallace, P.J., Plank, T., Bodnar, R.J., 2015. Bubbles matter: An assessment of the contribution of vapor bubbles to melt inclusion volatile budgets. Am. Mineral. 100, 806–823. https://doi.org/10.2138/am-2015-5036

Newville, M., Stensitzki, T., Allen, D.B., Rawlik, M., Ingargiola, A., Nelson, A., 2016. LMFIT: Non-linear least-square minimization and curve-fitting for Python. Astrophys. Source Code Libr. ascl-1606.

Remigi, S., Mancini, T., Ferrando, S., Frezzotti, M.L., 2021. Interlaboratory Application of Raman CO_2 Densimeter Equations: Experimental Procedure and Statistical Analysis Using Bootstrapped Confidence Intervals. Appl. Spectrosc. 75, 867–881. https://doi.org/10.1177/0003702820987601

Rosso, K.M., Bodnar, R.J., 1995. Microthermometric and Raman spectroscopic detection limits of C02 in fluid inclusions and the Raman spectroscopic characterization of C02. Geochim. Cosmochim. Acta 59, 3961–3975. https://doi.org/10.1016/0016-7037(95)94441-H

Song, Y., Chou, I., Hu, W., Robert, B., Lu, W., 2009. CO2 Density-Raman Shift Relation Derived from Synthetic Inclusions in Fused Silica Capillaries and Its Application. Acta Geol. Sin. - Engl. Ed. 83, 932–938. https://doi.org/10.1111/j.1755-6724.2009.00090.x

Span, R., Wagner, W., 1996. A New Equation of State for Carbon Dioxide Covering the Fluid Region from the Triple-Point Temperature to 1100 K at Pressures up to 800 MPa. J. Phys. Chem. Ref. Data 25, 1509–1596. https://doi.org/10.1063/1.555991

Sublett, D.M., Sendula, E., Lamadrid, H.M., Steele-MacInnis, M., Spiekermann, G., Bodnar, R.J., 2021. Raman spectral behavior of N_2, CO_2, and CH_4 in N_2–CO_2–CH_4 gas mixtures from 22°C to 200°C and 10 to 500 bars, with application to other gas mixtures. J. Raman Spectrosc. 52, 750–769. https://doi.org/10.1002/jrs.6033

Taran, M.N., Matsyuk, S.S., 2013. Fe2+, Mg-distribution among non-equivalent structural sites M1 and M2 in natural olivines: an optical spectroscopy study. Phys. Chem. Miner. 40, 309–318. https://doi.org/10.1007/s00269-013-0572-x

Ullrich, K., Langer, K., Becker, K.D., 2002. Temperature dependence of the polarized electronic absorption spectra of olivines. Part I - fayalite. Phys. Chem. Miner. 29, 409–419. https://doi.org/10.1007/s00269-002-0248-4

Venugopal, S., Schiavi, F., Moune, S., Bolfan-Casanova, N., Druitt, T., Williams-Jones, G., 2020. Melt inclusion vapour bubbles: the hidden reservoir for major and volatile elements. Sci. Rep. 10, 9034. https://doi.org/10.1038/s41598-020-65226-3

Wang, H., Lu, W., Wang, W., Liu, Q., Yamamoto, J., 2024. High-precision analysis of carbon isotopic composition for individual CO2 inclusions via Raman spectroscopy: Addressing issues arising from the laser-heating effects. Chem. Geol. 651, 122014. https://doi.org/10.1016/j.chemgeo.2024.122014

Wang, W., Caumon, M.-C., Tarantola, A., Pironon, J., Lu, W., Huang, Y., 2019. Raman spectroscopic densimeter for pure CO2 and CO2-H2O-NaCl fluid systems over a wide P-T range up to 360 °C and 50 MPa. Chem. Geol. 528, 119281. https://doi.org/10.1016/j.chemgeo.2019.119281

Wang, X., Chou, I.-M., Hu, W., Burruss, R.C., Sun, Q., Song, Y., 2011. Raman spectroscopic measurements of CO2 density: Experimental calibration with high-pressure optical cell (HPOC) and fused silica capillary capsule (FSCC) with application to fluid inclusion observations. Geochim. Cosmochim. Acta 75, 4080–4093. https://doi.org/10.1016/j.gca.2011.04.028

Wieser, P., Kent, A.J.R., DeVitre, C.L., Gazel, E., Till, C.B., Johnson, Emily, Wallace, Paul, Couperthwaite, F.K., 2023. Bubble Trouble: Raman measurements of Cascade melt inclusion vapour bubbles indicate substantial underestimation of magma storage depths in legacy data. Presented at the AGU Fall Meeting 2023. Poster No. 0203, id. V23D-0203.

Wieser, P.E., Edmonds, M., Maclennan, J., Jenner, F.E., Kunz, B.E., 2019. Crystal Scavenging from Mush Piles Recorded by Melt Inclusions. Nat. Commun.

Wieser, P.E., Lamadrid, H., Maclennan, J., Edmonds, M., Matthews, S., Iacovino, K., Jenner, F.E., Gansecki, C., Trusdell, F., Lee, R.L., Ilyinskaya, E., 2021. Reconstructing Magma Storage Depths for the 2018 Kīlauean Eruption From Melt Inclusion CO_2 Contents: The Importance of Vapor Bubbles. Geochem. Geophys. Geosystems 22. https://doi.org/10.1029/2020GC009364

Wieser, P.E., Shi, S.C., Gleeson, M.L.M., Rangel, B., DeVitre, C.L., Bearden, A.T., Lynn, K.J., Camille-Caumon, M., 2025. Fluid inclusion constraints on the geometry of the magmatic plumbing system beneath Mauna Loa — Part 1:lavas and tephras. Bull. Volcanol. 87, 89. https://doi.org/10.1007/s00445-025-01874-5

Wojdyr, M., 2010. *Fityk* : a general-purpose peak fitting program. J. Appl. Crystallogr. 43, 1126–1128. https://doi.org/10.1107/S0021889810030499

Wright, R.B., Wang, C.H., 1973. Density effect on the Fermi resonance in gaseous CO2 by Raman scattering. J. Chem. Phys. 58, 2893–2895. https://doi.org/10.1063/1.1679594

Yamamoto, J., Hagiwara, Y., 2024. Precision evaluation of Raman densimetry for carbon dioxide: improvement by correction for the drift effect. Appl. Opt. 63, 1402. https://doi.org/10.1364/AO.507939

Yamamoto, J., Kagi, H., 2008. Application of densimetry using micro-Raman spectroscopy for CO2 fluid inclusions: a probe for elastic strengths of mantle minerals. Eur. J. Mineral. 20, 529–535. https://doi.org/10.1127/0935-1221/2008/0020-1825

Yamamoto, J., Kagi, H., 2006. Extended Micro-Raman Densimeter for CO_2 Applicable to Mantle-originated Fluid Inclusions. Chem. Lett. 35, 610–611. https://doi.org/10.1246/cl.2006.610

Yuan, X., Mayanovic, R.A., 2017. An Empirical Study on Raman Peak Fitting and Its Application to Raman Quantitative Research. Appl. Spectrosc. 71, 2325–2338. https://doi.org/10.1177/0003702817721527

Supporting Information for: Evaluating and Optimizing Raman Analytical Protocols for CO_2 Fluids

Penny E. Wieser[1*], Charlotte L DeVitre[1, 2], Isabelle Susman[1]

[1] Earth and Planetary Sciences, University of California, Berkeley, CA 94270, USA

[2] Now at Department of Earth and Environmental Sciences, University of Ottawa, Ottawa, ON K1N 6N5, Canada

Supporting Table 1- Compilation of studies publishing densimeters, and the methods used to calibrate the spectrometer (which sets the non-linearity response seen in Fig. 1b) and correct data for drift during a run. n.d. indicates the publication did not say what method was used. It is not always clear if the Raman shift standard was used alone, or in addition to some form of instrument software calibration.

Reference	**Spectrometer Calibration method**	**Drift correction used**	**Pixel resolution**	**Spectral resolution**
Rosso and Bodnar, (1995)	Spectrometer position calibrated between analyses using Neon lines and a mercury line.		0.84 cm^{-1}/pixel	n.d.
Kawakami et al. (2003)	Raman shift calibrated with Naphthalene	n.d.	1.5 cm^{-1}/pixel	n.d.
Yamamoto and Kagi, (2006)	Raman shift calibrated with Naphthalene	n.d.	1.5 cm^{-1}/pixel	n.d.
Song et al. (2009)	Diamond (Raman shift standard)	n.d.	State spectral resolution of 1 cm-1, (doesn't clarify if resolution per pixel or the fwhm of a narrow line)	
Lamadrid et al. (2017) LabRam HR (800 mm)	Establish linearity of the spectrometer using the Laser line and Ne line at 1458.58 cm^{-1}	Ne lamp (lines at 1031.42 cm^{-1} and 1458.58 cm^{-1} for a 514 nm laser)	No specific data, state spectral resolution of different instruments ranges from 1.4-8 cm^{-1} (doesn't clarify if	

			resolution per pixel or the fwhm of a narrow line)	
Wang et al. (2011)	Co-collected diamond were used to calibrate the individual positions of each CO2 peak. Diad splits were corrected using the 1192.6 and 1598.9 cm-1 peaks of benzonitrile collected every 15 minutes.		State spectral resolution of 1 cm-1 (doesn't clarify if resolution per pixel or the fwhm of a narrow line)	
Fall et al. (2011)	n.d.	n.d.	n.d.	
Wang et al. (2019)	Neon Lamp	Neon Lamp using the L17 correction for the 1447 and 1613 cm-1 lines (532.06 nm laser)		
Le et al. (2019)	Say no need for absolute wavelength calibration of the spectrometer	n.d.	n.d.	1.67 cm^{-1} using fwhm of Ne peak at 2348 cm^{-1}
Le et al., (2020)	n.d.	n.d.	n.d.	1.6 cm^{-1} don't say method
Sublett et al. (2020)	No calibration method given ,but say they systematically subtract a X cm-1 offset for their peak positions of gases relative to other studies,	Ne peaks collected simultaneously to correct for spectrometer drift.	n.d.	n.d.
(Hagiwara et al., 2020)	Real-time wavelength calibration using 1449 and 1222 cm-1 Ne lines following Lamadrid and Lin et al.		0.29 cm-1/pixel	1.1 cm^{-1}

	n.d.	Ne lines at 1221.73 and 1449.19 cm-1.	0.28 cm-1/pixel	n.d.
Wieser et al., (2021)	Si chip	Repeated synthetic FI measurement	n.d.	n.d.
DeVitre et al. (2021)	Hg-Ar lamp (atomic emission line)	Neon lamp using the L17 correction for the 1116 cm^{-1} and 1447 cm^{-1} lines (532.067 nm laser)	n.d.	n.d.
Allison et al. (2021)	Raman shift calibrated using three calibration standards (cyclohexane, naphthalene, 1,4 bis (2-methylstyryl) benzene. Unclear if analysed repeatedly to correct for drift.		n.d.	n.d.
DeVitre and Wieser, 2024	Hg-Ar lamp (atomic emission line)	Neon lamp using the L17 correction for the lines at 1117 cm^{-1} and 1447 cm^{-1} (532.046 nm laser)	0.54 cm-1/pixel	n.d.

12

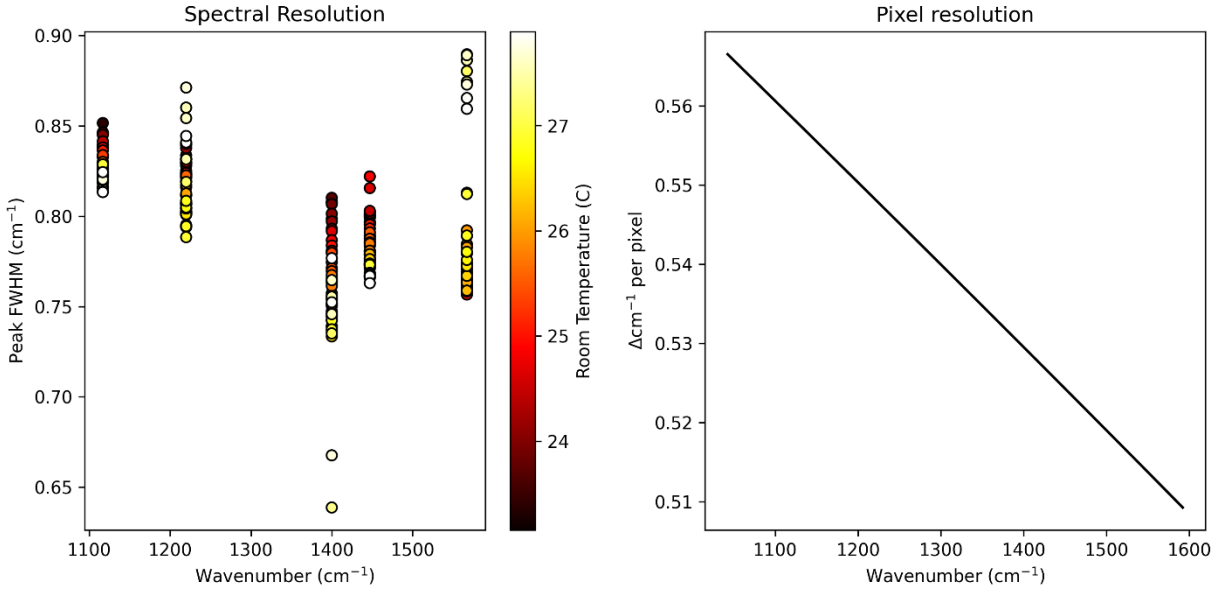

13

Supporting Figure S1 – We estimate the spectral resolution using the full width half maximum(FWHM) of Ne lines following Hagiwara et al. (2023). Spectra were collected during the increase in room temperature, and show a decrease in peak FWHM as room T increases. This assumes that the Ne lines are infinitely narrow, and the measured FWHM is a function of the spectral resolution of the spectrometer. There are complex changes in FWHM with maximum – with not all lines showing the same pattern. We compare this to the pixel resolution, calculated by subtracting the x coordinate of the n+1 pixel from the nth pixel.

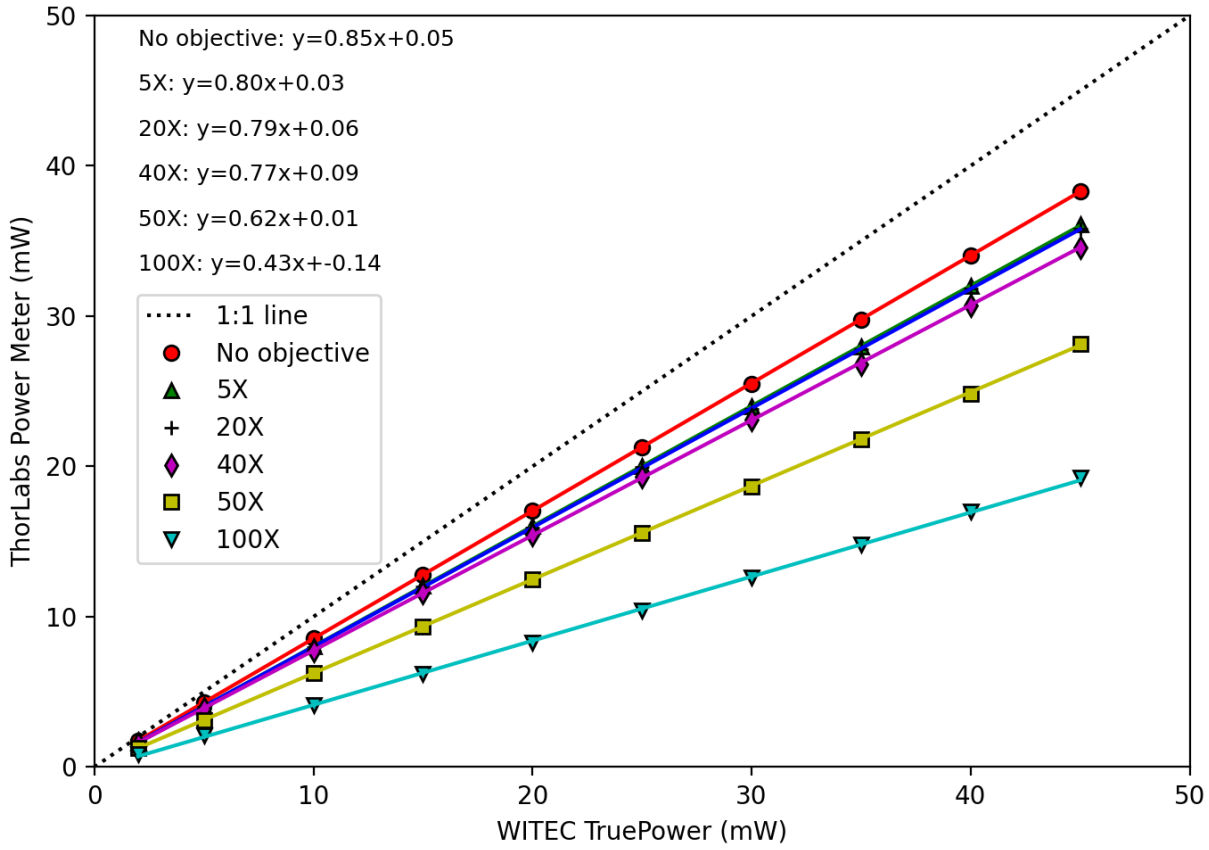

Supporting Figure S2 – Comparison of power from the WITec TruePower read out with the power measured by a ThorLabs power meter. For the 'No objective' measurement, the S121C sensor was pushed into the objective turret hole after unscrewing the objective (it fits perfectly). For the 5-100X measurements, the S121C sensor was set on the sample stage and the z height was varied until the maximum power reading was achieved on the sensor (this was very close to the optimal optical focus using reflected light). We found that x-y positioning of the laser on the sensor affected the laser power by roughly 2-3%.

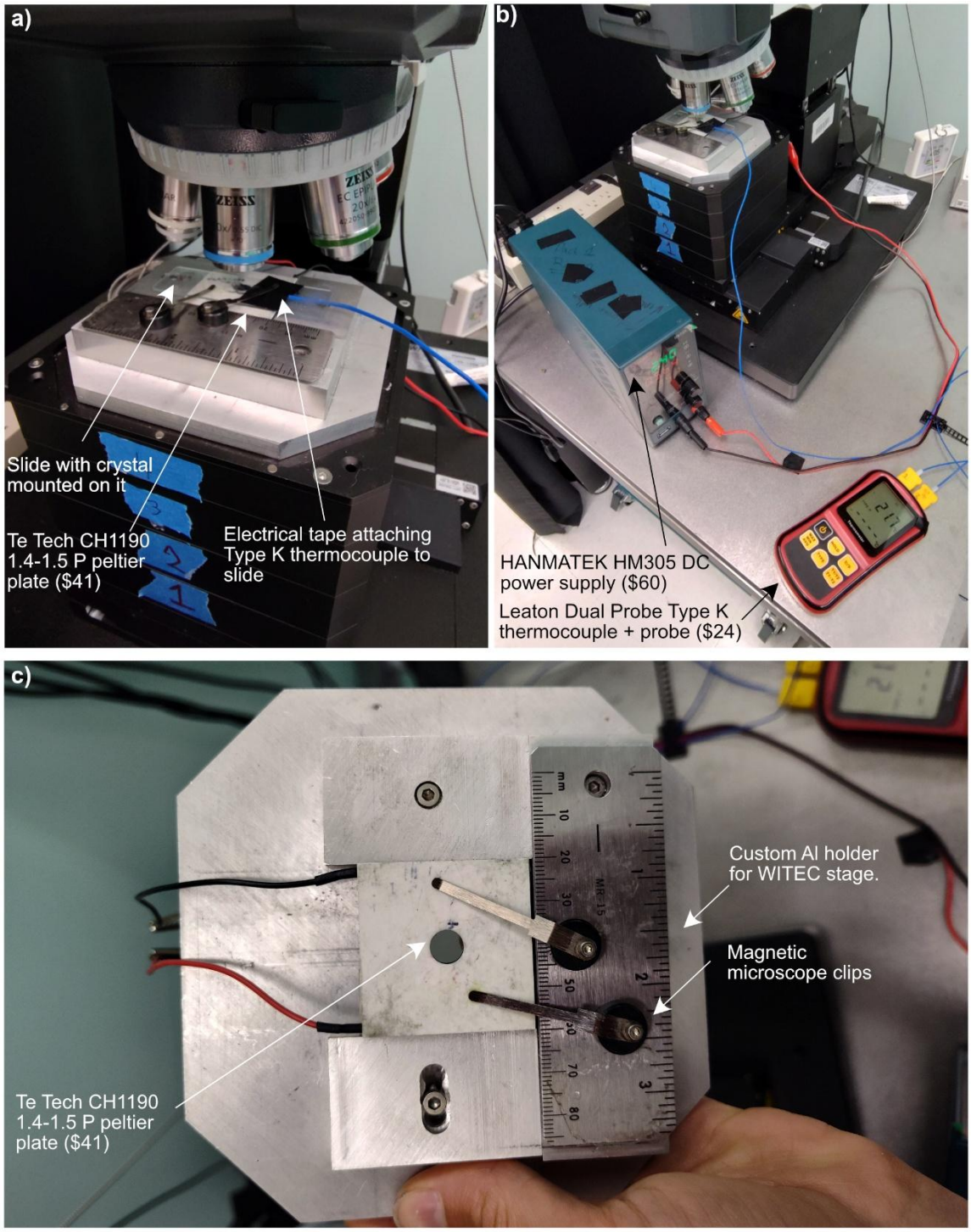

Supporting Figure S3 – Apparatus used for heating samples to 37℃. a) Picture showing a glass slide with a FI mounted in crystalbond under a 50X Zeiss objective. b) Picture showing the entire WITec system and the sample holder. A Type K thermocouple is taped on using electrical tape. This picture was taken while the slide was still warming up (hence the 21.7 ℃ temperature). c) Close up of the custom Aluminum holder that has the bottom machined out to slot onto the shape of the WITec base. There are 4 screws that attach to the magnets on the WITec stage (because Al is not magnetic). The ruler is glued to the top to provide a magnetic surface to attach a set of

magnetic microscope clips to help keep the sample in place. This holder was manufactured by our in-house machine shop (labour and material cost, $900). This holder keeps the peltier plate and sample still, making it possible to analyze very small inclusions without drift (1-2 μm).

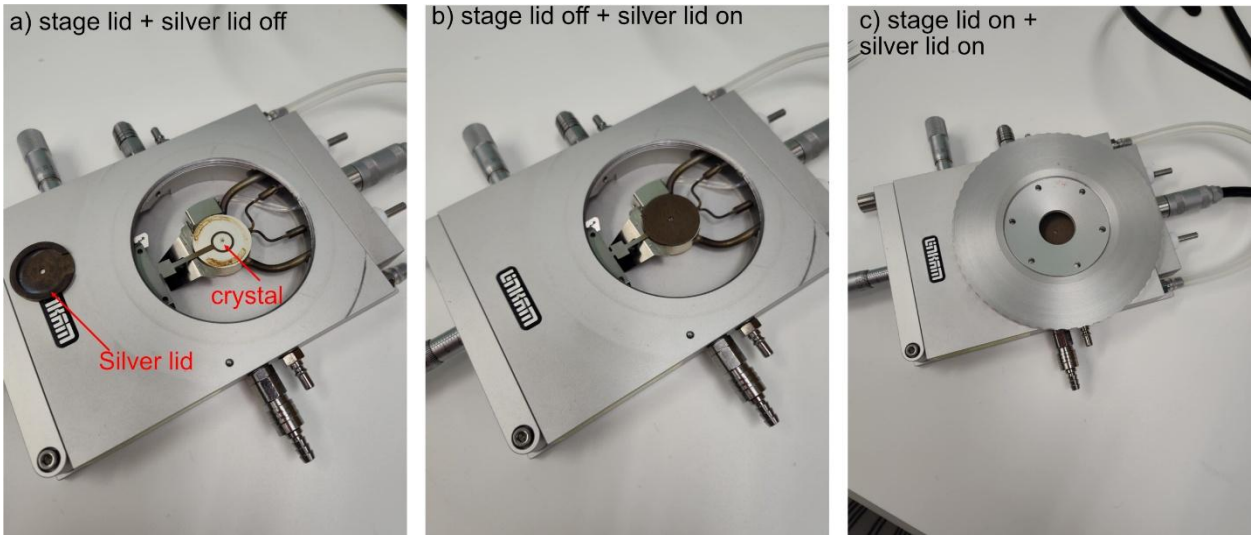

Supporting Figure S4 – Linkam apparatus which is mounted on the Raman for heating tests. a) The stage is entirely open, and the crystal of interest is placed on the glass circle. b) The silver lid is then placed ontop to help with temperature stability, but without sacrificing the Raman signal (as it has a hole in the top). In c), in addition to the silver lid, the stage lid is screwed on, leading to a drop in Raman signal.

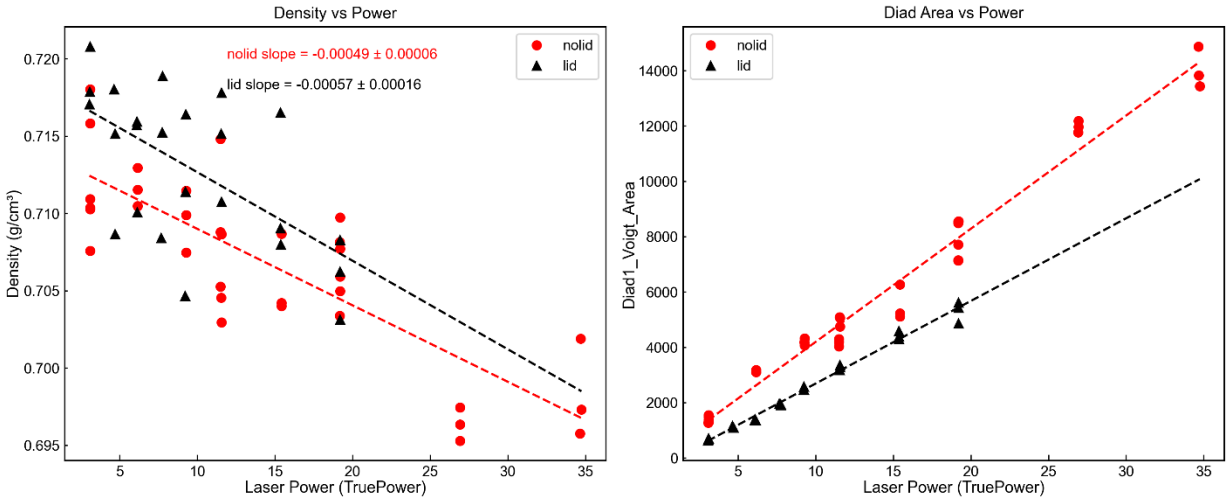

Supporting Figure S5 – Comparison of heating series for FI FG04_a13_12 performed with and without the stage lid. The gradient is within uncertainty when density is plotted against laser power. However, the intensity of Diad 1 (peak area) is significantly lower with the stage lid in place.

Peak fitting errors

DiadFit versions <=1.0.18 used a least squares cost function during peak fitting, where the deviation between each pixel intensity and the best fit model was given equal weight. This

simplification neglects the fact that Raman noise is heteroscedastic, where the error increases as a function of the intensity.

From v>= 1.0.19, DiadFit fit functions have a new input argument so that the weighting strategy can be changed. For reproducibility, we preserve an option to fit peaks with the old least squares approach (setting the parameter 'minimise' to 'least squares'), but by default the code now uses a weighted least square approach (minimise='least_squares'). According to the documentation, Lmfit defines the weights to use to calculate the fit residual as follows:

weights*(data-fit)

Following poisson statistics, we assume that σ = $\sqrt{N}$, where N is total counts. In lmfit, the weights are inputted as 1/error (python 3.x - Taking experimental errors into account in lmfit - Stack Overflow). Our code assigns a weight to each pixel as follows:

Weight = $\frac{1}{\sqrt{N}}$

When extracting errors from the covariance matrix, lmfit has two options: scale_covar=True, and scale_covar=False. The lmfit documentation suggests that in cases where the absolute value of the uncertainty is unknown on each point, but the peak fit is good, scale_covar should be set to True, which rescales the uncertainty in the data such that the reduced chi-square is 1.

First, we assess how changing the minimization regime from least-squares to weighted least squares affects the peak positions using the room heating test data shown in Fig. 6. The shift in peak position is very small, and within the uncertainty of the two fit routines (Supporting Fig. S6). We also fit a subset of 10 spectra in Fityk. Because of the effect of user-choice related to manual fitting in the Fityk GUI, both C. DeVitre and P. Wieser independently conducted the fits using psuedovoigt peaks. Where possible, a Gaussian was added under the peaks that were elevated above the background, but we found it very challenging to get a good fit in Fityk (where clicks are required), so for many spectra a Gaussian could not be reliably added as it resulted in a visually worse fit. The peak positions obtained from DiadFit are also extremely similar to Fityk, but more so for Diad1 where the Gaussian is not required, and less so for Diad2 where a gaussian is required (Fig. S7-S8). We turn off the Gaussian argument in DiadFit to better compare, which causes the diad2 peak positions to show a much better alignment (although the fits are now noticeably worse to the data, Supporting Figure S8).

We also compare our errors to those from Fityk to benchmark the new fitting routine. Like lmfit, Fityk can return two types of errors. The default output is labelled *'±standard errors: sqrt(WSSR/DoF COV_kk)*" which are equivalent to scale_covar=True in lmfit, and there is also an option to select errors labelled '*sqrt(COV_kk)*', which are equivalent to scale_covar=False in lmfit (Supporting Figure S8). The unscaled errors are completely implausible given agreement between lmfit and Fityk, and the long- and short-term laboratory stability we observe (Figure 5 and 6), but agree well between these two bits of software.

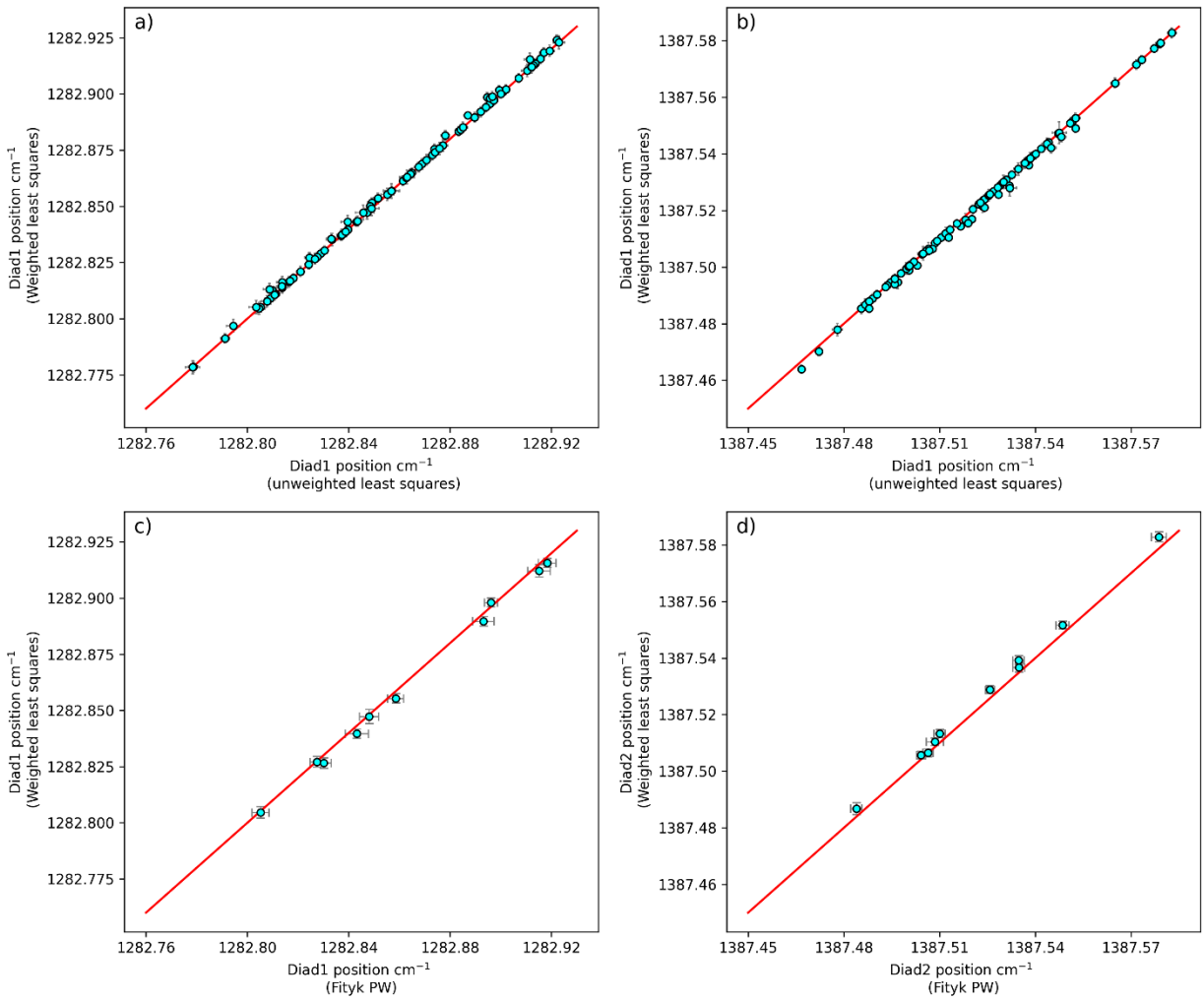

Supporting Figure S6 – Comparing different peak fitting routines. a-b) comparing peak positions determined from unweighted least squares (DiadFit v<1.0.18) and weighted least squares (DiadFit v≥1.0.19). The red line shows a 1:1 line, and the two methods do not deviation from the 1:1 line in a meaningful way considering the peak fitting errors. For a subset of 10 spectra, we also fit the data using Fityk.

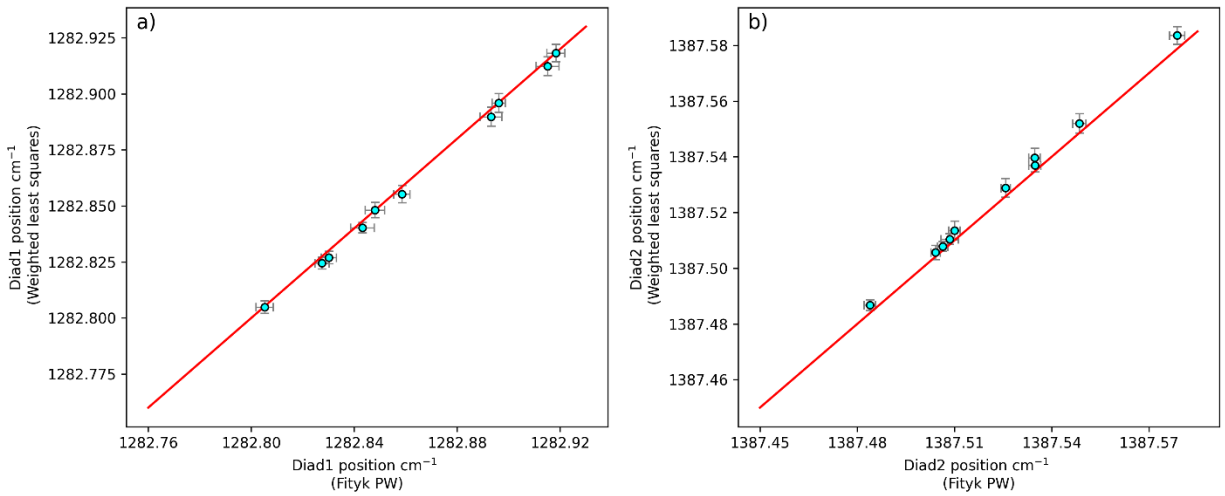

97
98 **Supporting Figure S7**- Comparing Fityk to DiadFit where no Gaussian was used to improve the
99 fit to stronger peaks.

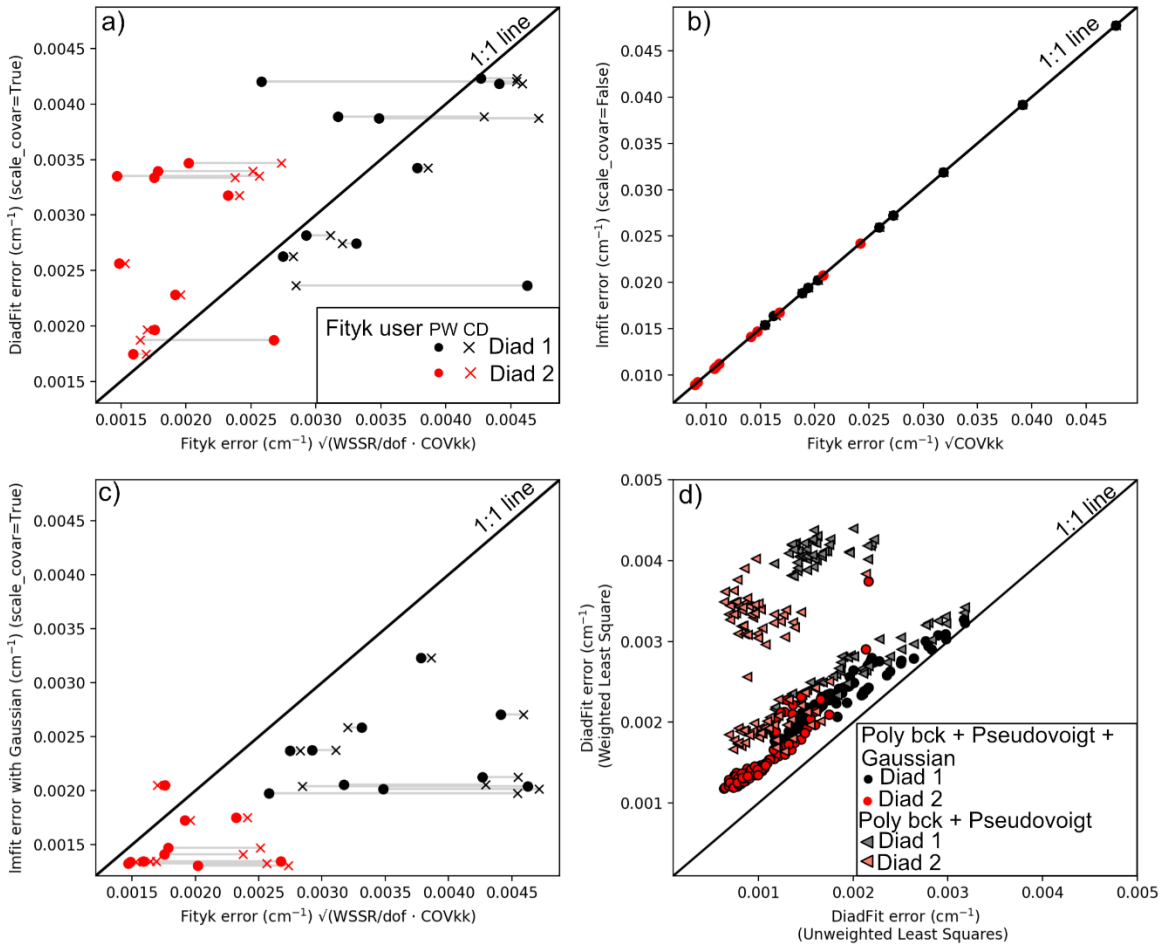

100

101 **Supporting Figure S8** – Comparison of errors determined from different methods. a) scaled
102 errors from DiadFit (excluding the Gaussian) and Fityk. For each spectra, errors determined from

P. Wieser (PW) and C. DeVitre (CD) are shown (dot and x joined by a line). It is clear that small changes in clicked parameters such as user backgrounds, peak positions have a large influence on the quality of the fit, and thus scaled errors. b) Unscaled errors are identical for Fityk and lmfit, regardless of user (because these errors are insensitive to the quality of the fit). c) Same comparison as in a), but using fits with the Gaussian function enabled in DiadFit. This reduces the errors. d) Comparison of errors from the unweighted least squares and weighted least squares approaches in Diadfit, with and without Gaussian peaks enabled.

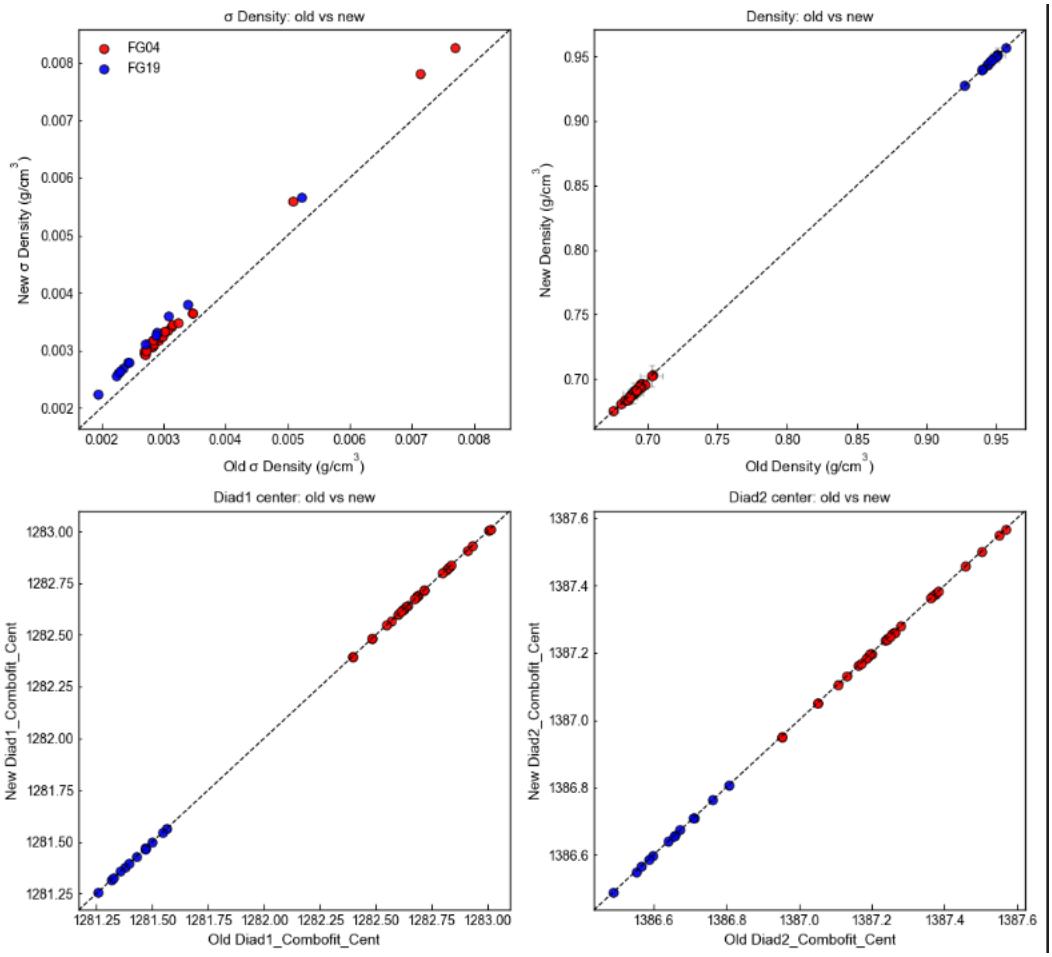

Supporting Figure S9 – Comparison of peak fitting positions and errors using least squares (old) and weighted least squares (new) for standard analyses from 13 analytical separate analytical session.

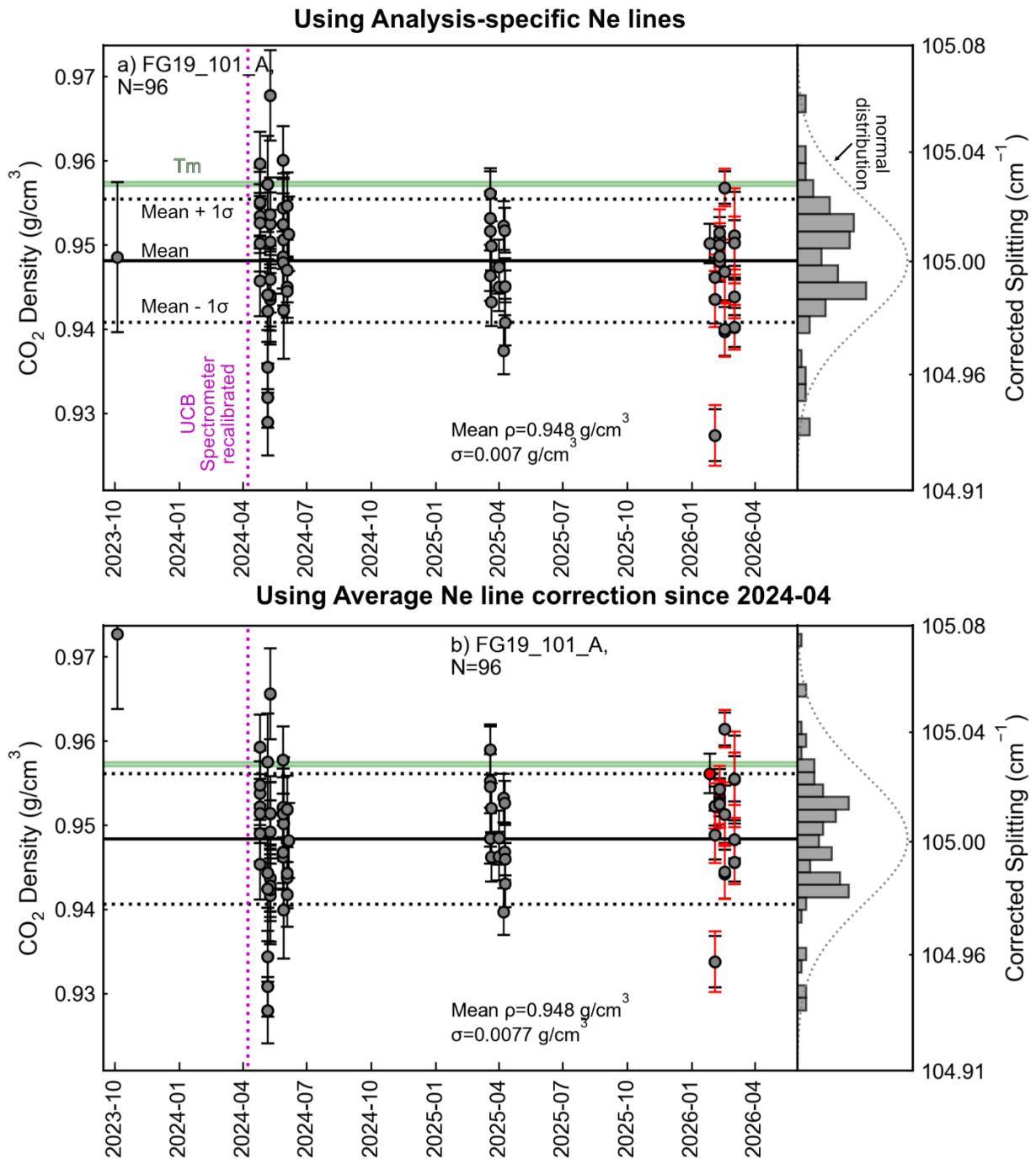

Supporting Figure S10 - Long-term variability in standard values collected at UCB for standard FG19_101_A. a) Data reduced using a drift correction model for each analytical session. b) Data reduced using the average Neon line correction factor for all standard acquisitions after the instrument recalibration (marked with a magenta line). The green bar shows the density determined by Microthermometry, accounting for the uncertainty in the temperature reading of the stage. The black solid line shows the mean Raman value for the standard, and the dotted black lines ±1 σ. The distribution of densities is shown as a histogram, compared to a normal distribution based on the mean and standard deviation.

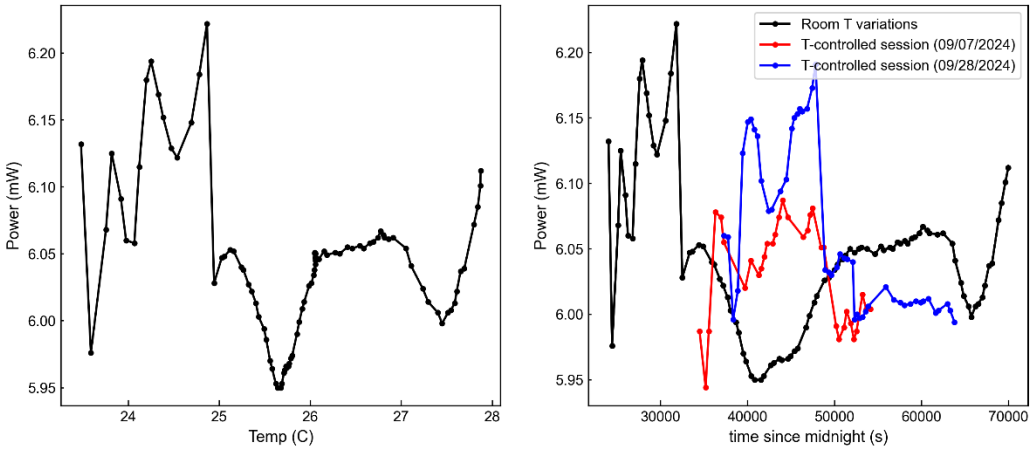

Supporting Fig. S11 – Plot of laser power measured with the TruePower meter against Temperature during the room temperature heating test to show there are no coherent variations outside of the ±0.1 mW read out precision of the TruePower meter. The variability seen is of similar magnitude to that seen during two analytical sessions with the HVAC system regulating temperature (red and blue lines from Kahl et al. 2025).

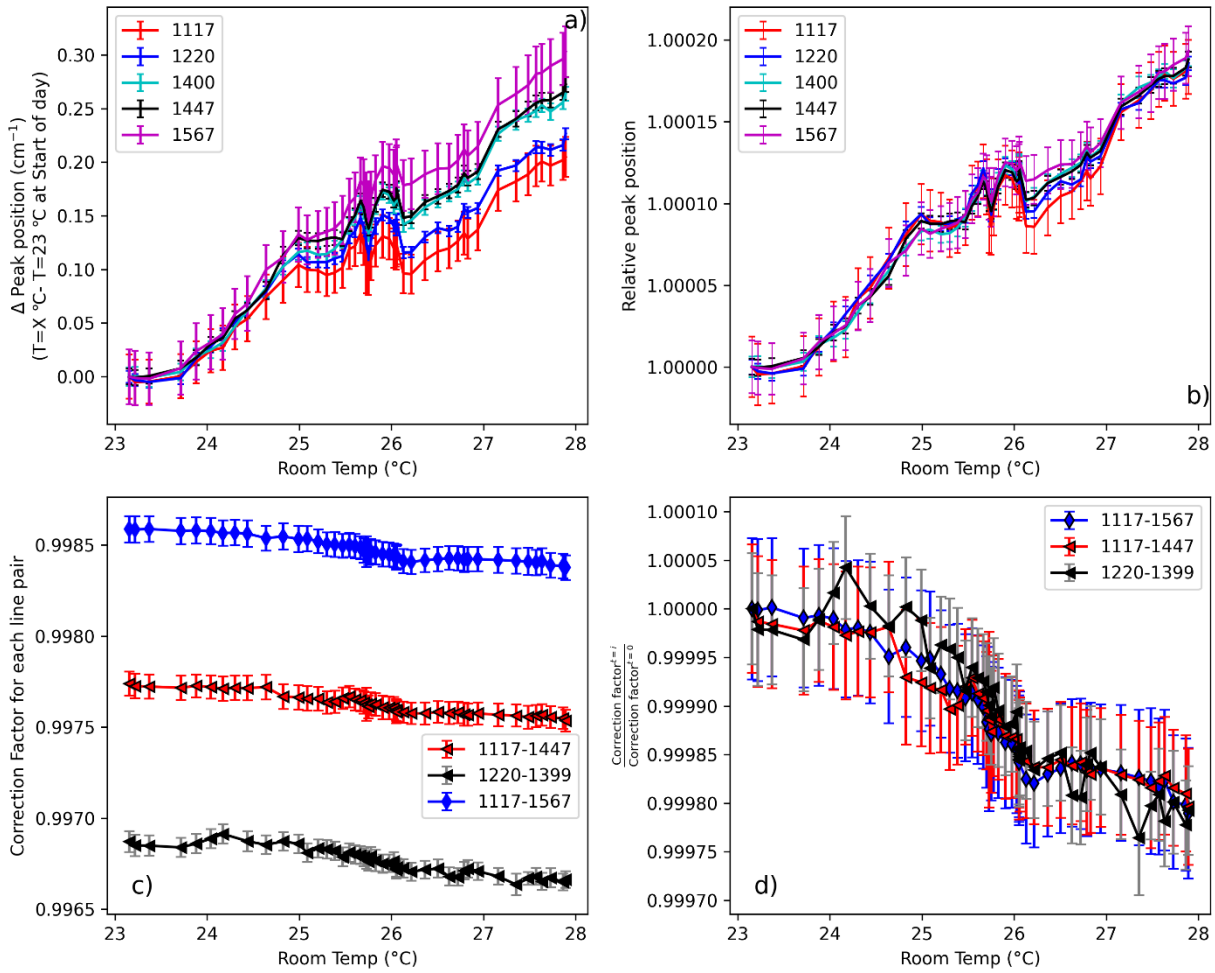

Supporting Figure S12 – Change in Neon line position, and correction factors calculated for different Neon line pairs during perturbations in the room temperature of 5 ℃. a) Absolute change in peak position, calculated as the peak position at T=X ℃ minus the peak position in the first Neon Acquisition b) Proportional change in peak position, calculated as the peak position at T=X ℃ divided by the peak position in the first Neon Acquisition. b) Absolute correction factor, calculated as the difference between the measured position of the two Neon lines and the theoretical distance. c) Change in correction factor, defined as the correction factor at each step divided by the correction factor in the first acquisition. All Neon lines follow the same trend within uncertainty so would have the same effect on removing instrument drift due to temperature fluctuations.

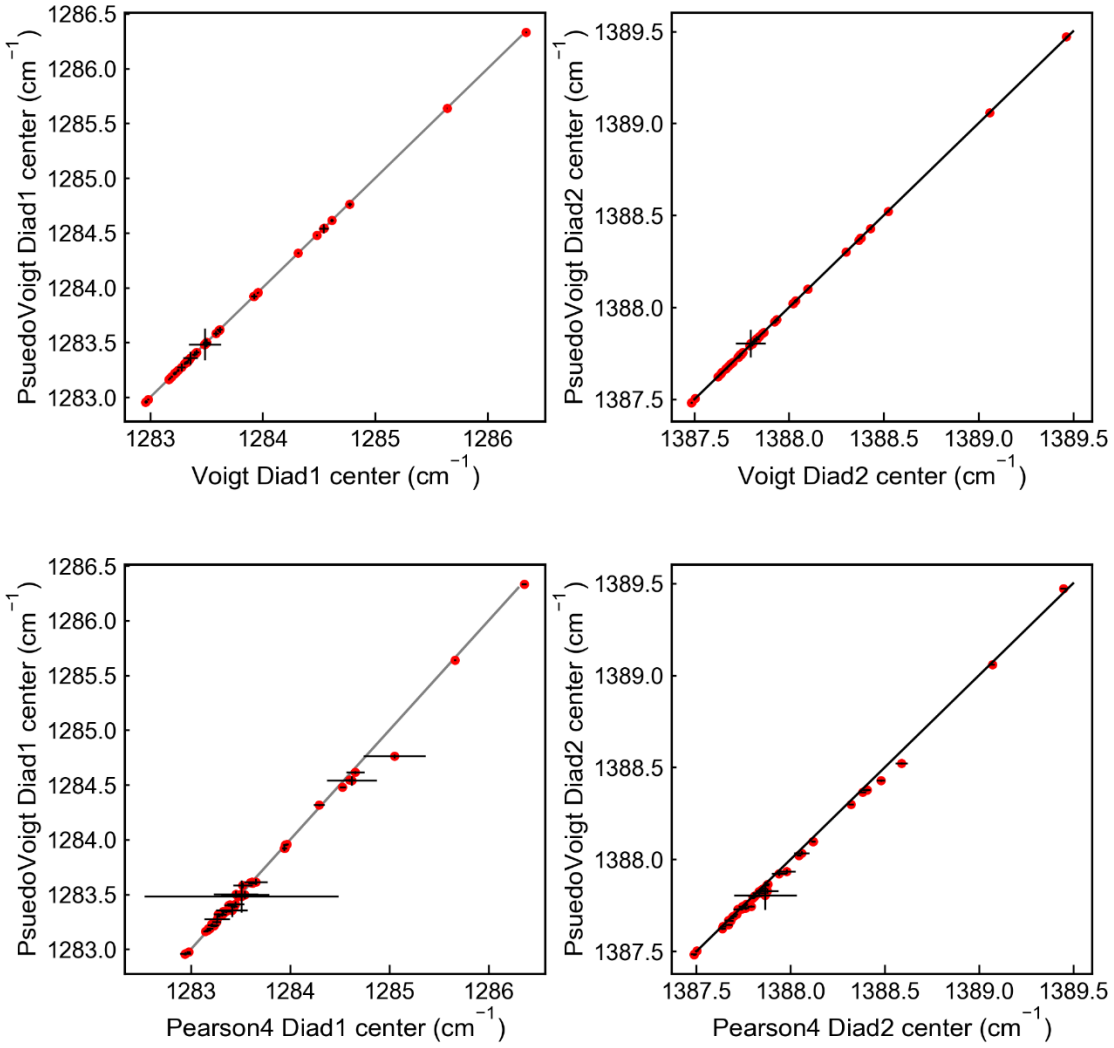

147

148 **Supporting Figure S13** – Comparison of different PDF fits for Fogo fluid inclusions (as for Fig 8
149 in the main text).

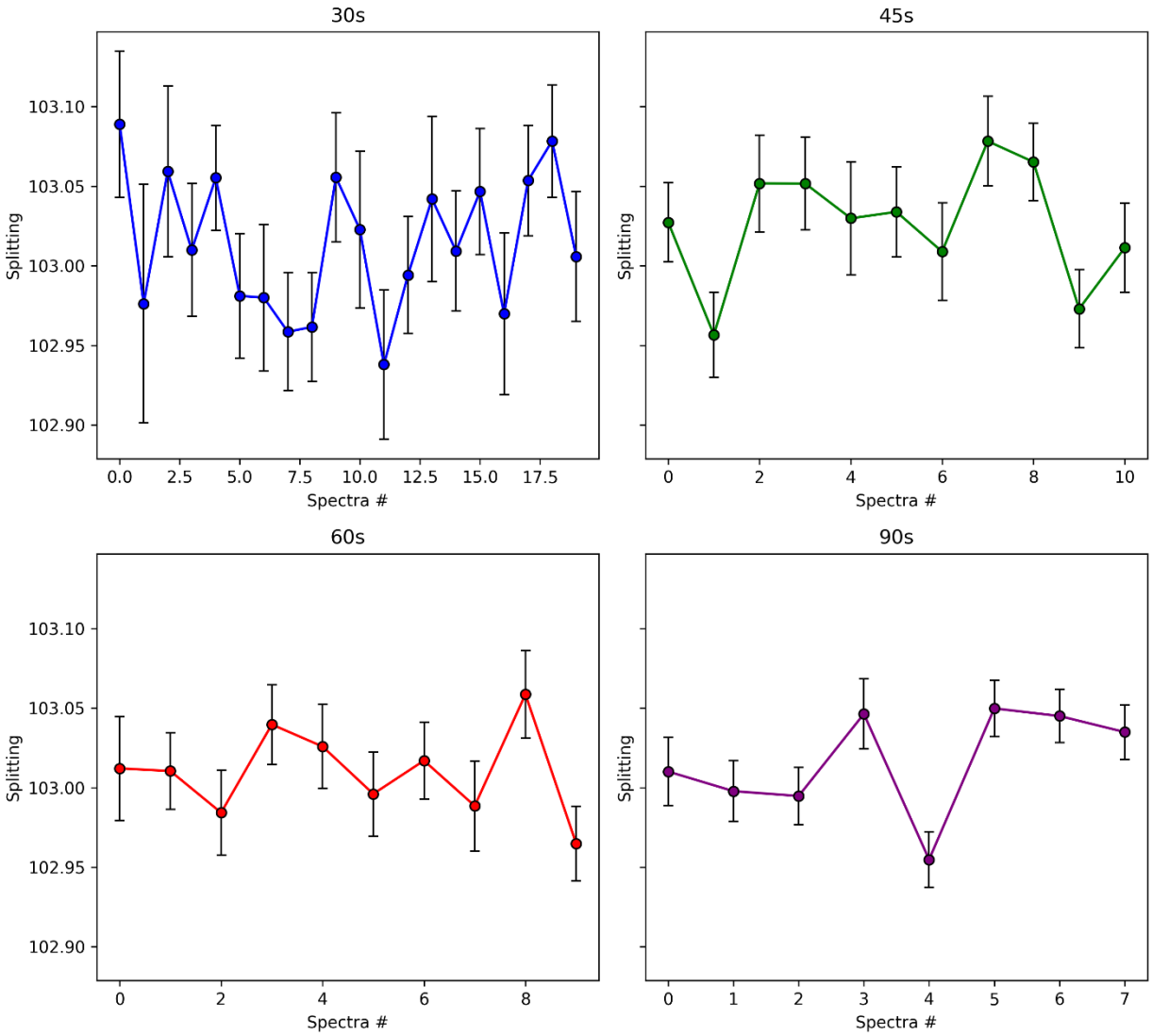

Supporting Figure S14 – Variability in splitting from each spectra for N=1 accumulation for a melt inclusion vapour bubbles from Mauna Ulu (MI1~0.015 g/cm^3, Wieser et al., 2019). The errors bars are 1 sigma errors from DiadFit.

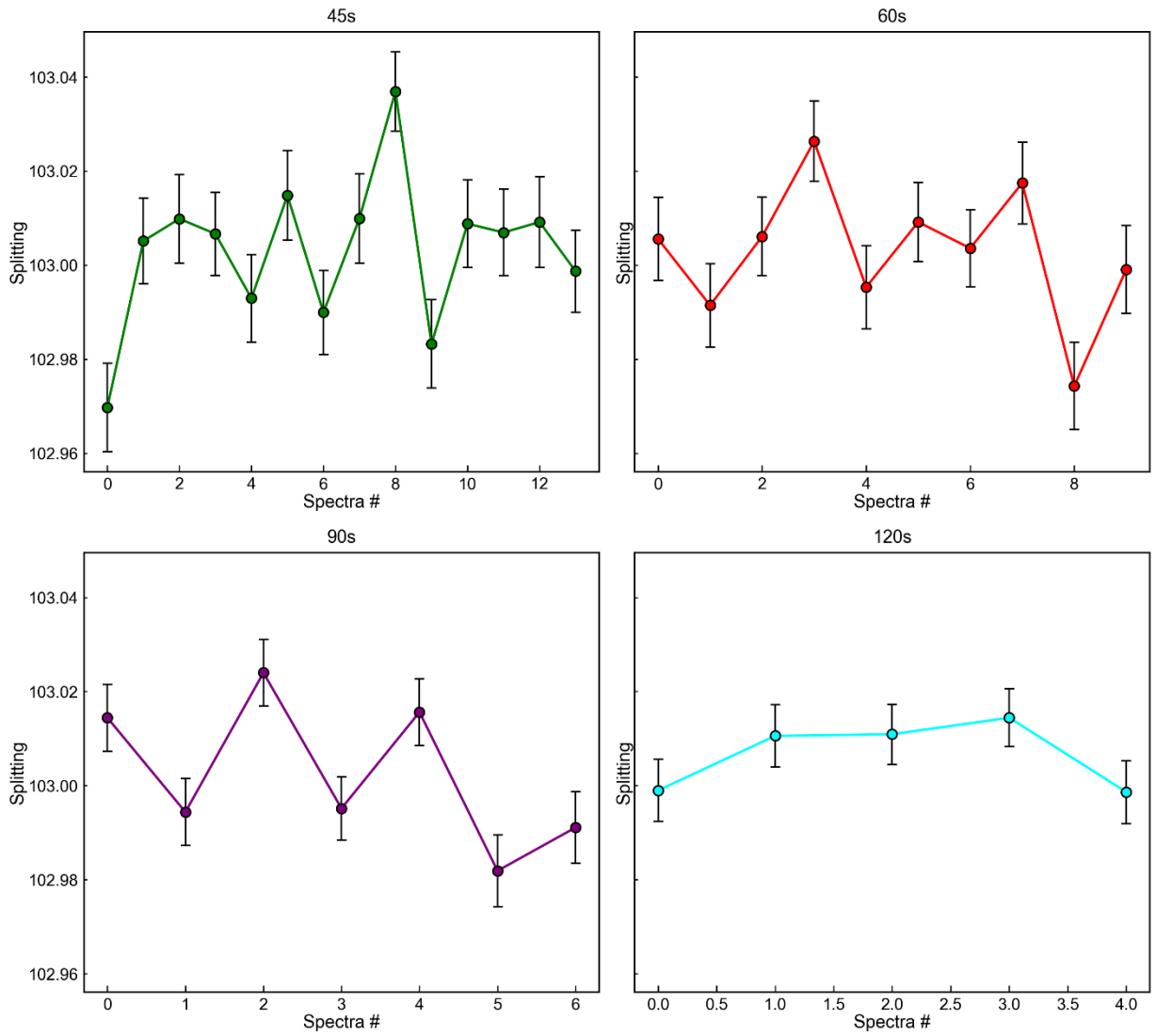

Supporting Fig. S15- Same for the Capillary capsule.

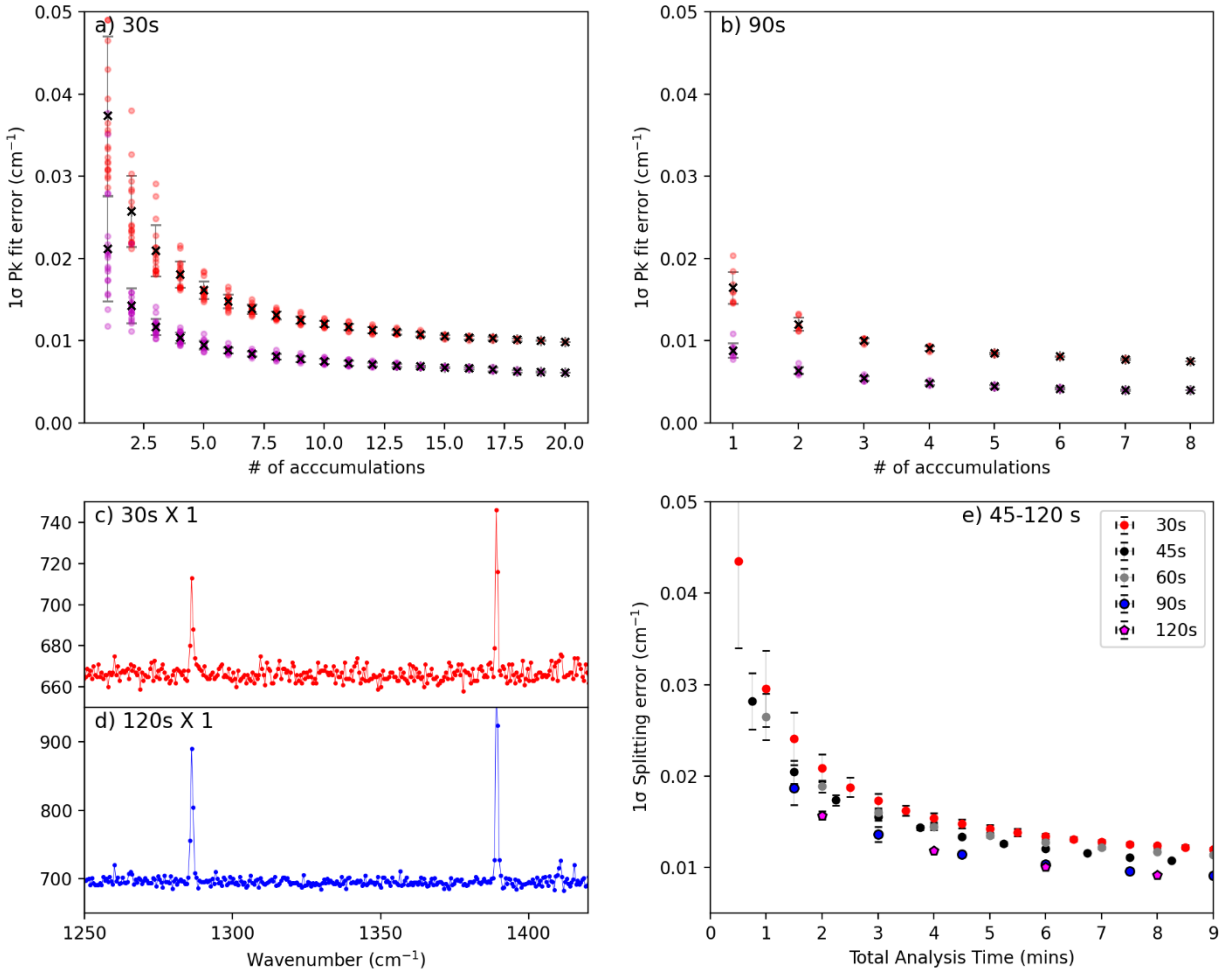

Supporting Figure S16 – Investigating peak fitting error as a function of integration time and accumulations using a melt inclusion vapour bubbles from Mauna Ulu (MI1~0.015 g/cm^3, Wieser et al., 2019). a-b) fitting error estimated from lmfit error for the peak position of diad1 and diad2 for 30 and 90s acquisitions. The x axis shows the number of spectra that were averaged prior to fitting the peaks (analogous to accumulation). The dots show an individual fitted spectra (e.g. spectra 1 to 10 for accumulations =1, average of spectra 1-2, 2-3 3-4 for n=2 accumulations etc.). The cross shows the mean lmfit error, and the errorbar shows the std. dev of the lmfit error for each number of accumulations (e.g. 14 individually fitted spectra for n=1 accumulations). c-d) Example spectra for 45s x 1 and 90s x 1. e) Error on calculated splitting after combining different numbers of individual acquisitions to give different acquisition times. For example, 5 different 60s acquisitions were averaged for the 5 minute total acquisition time.

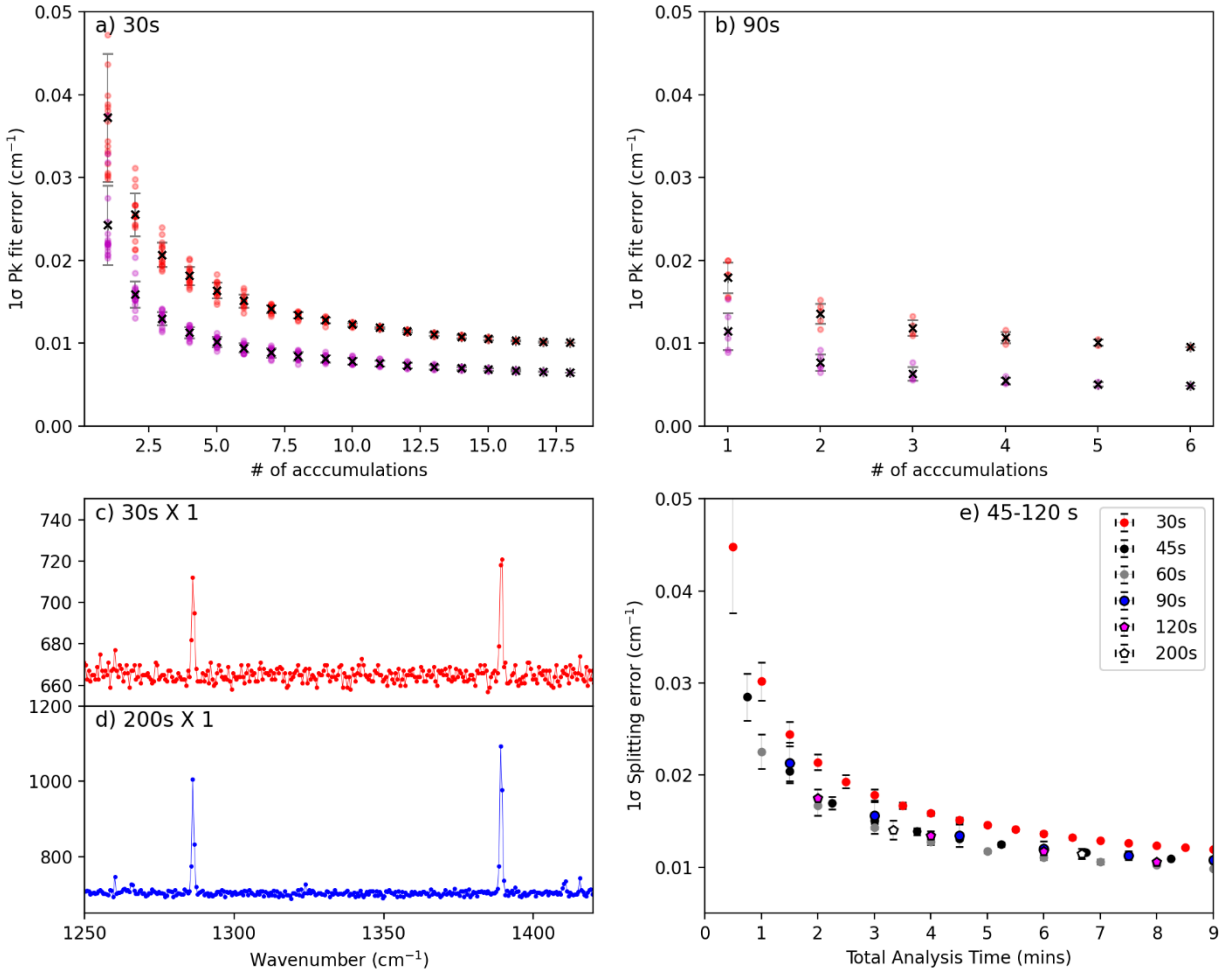

172

173 **Supporting Figure S17 –** Same as above but for MI2, including a 200s acquisition.

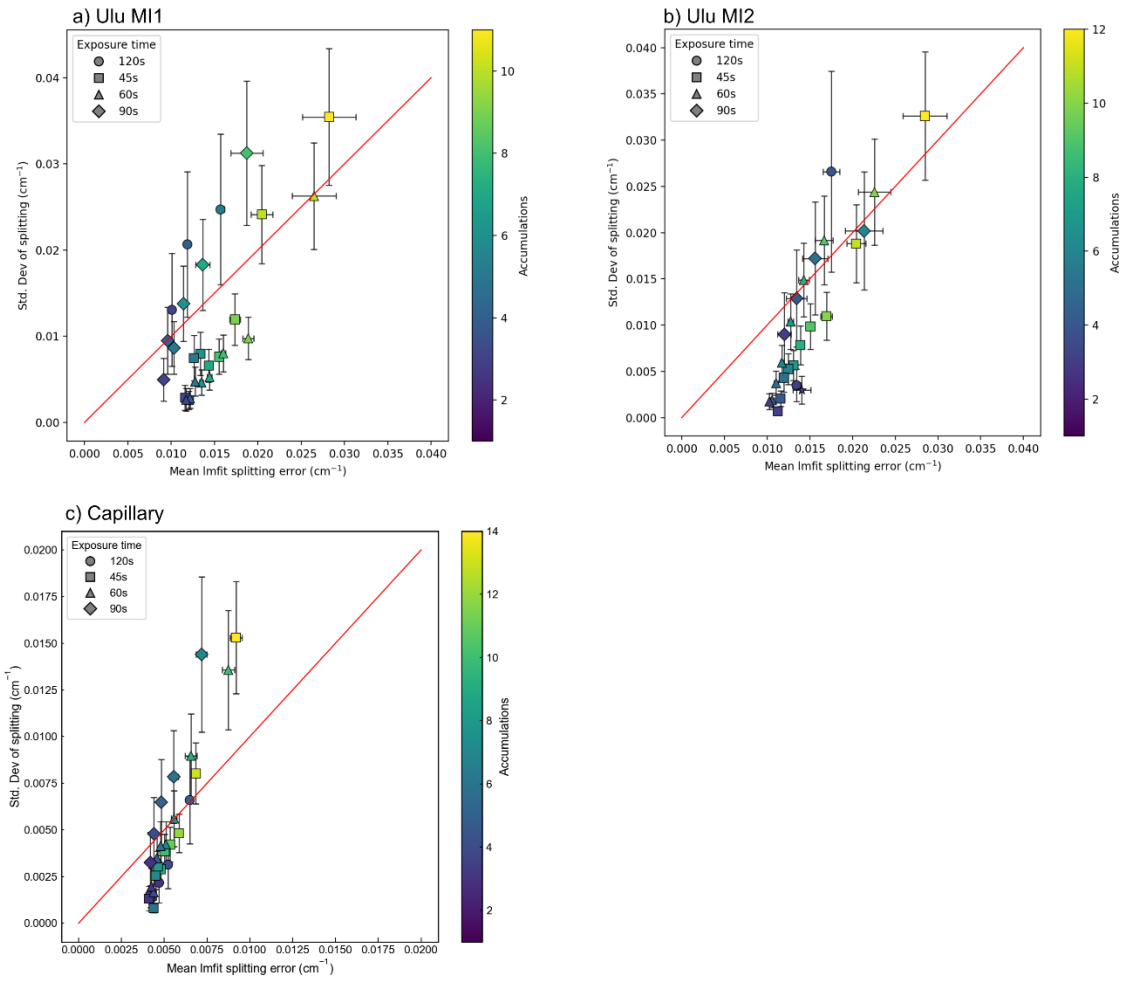

174

175 **Supporting Figure S18** – Comparison of mean lmfit splitting error (e.g. average error from N=5
176 spectra), and the standard deviation of the splitting determined from the 5 fits. The red line shows
177 a 1:1 line. The x error bar represents the standard deviation on the calculated lmfit error, and the
178 y error is calculated from the standard deviation based on the number of samples averaged.

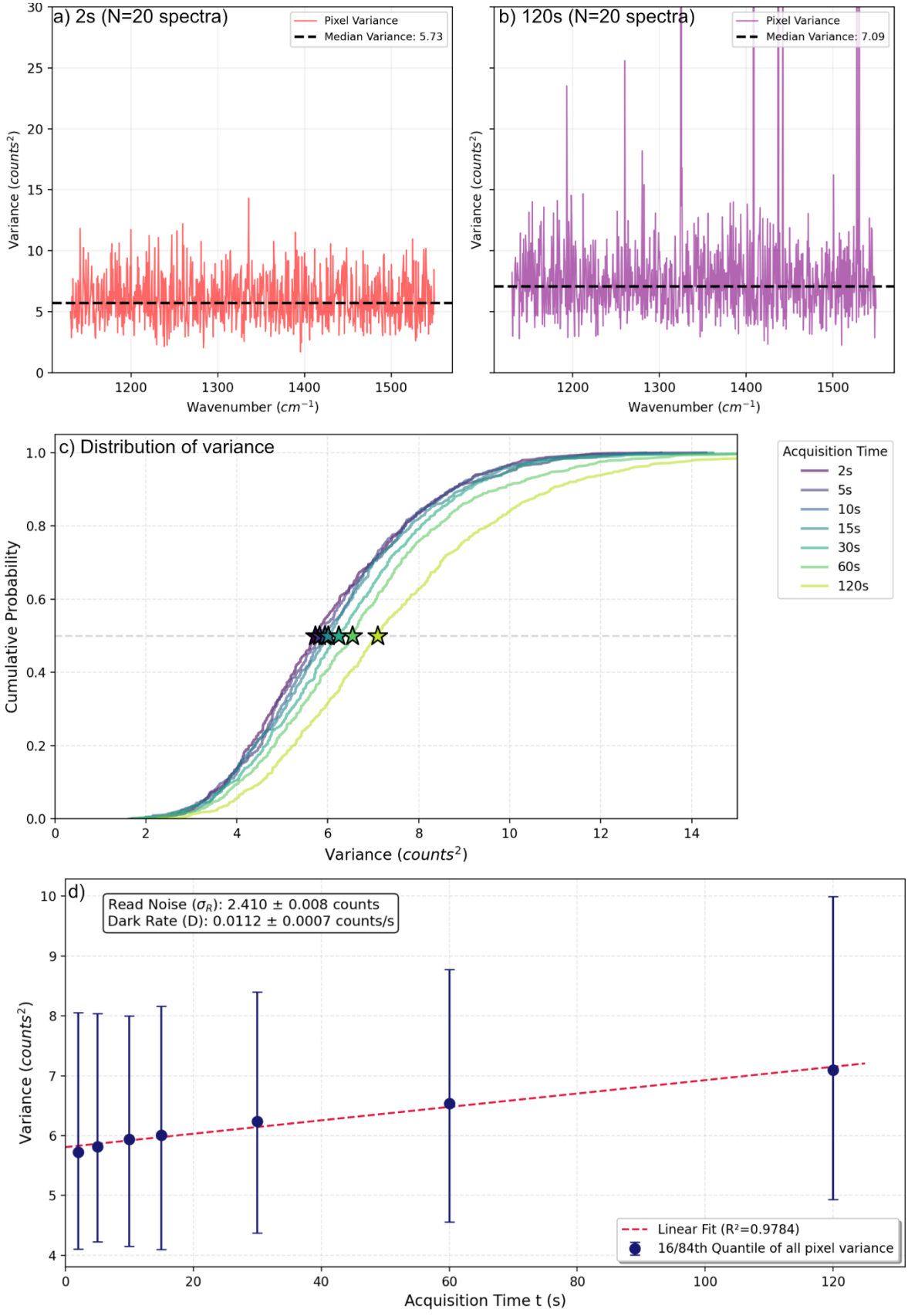
a) 2s (N=20 spectra)
Pixel Variance
Median Variance: 5.73
Variance (counts²)
Wavenumber (cm⁻¹)
b) 120s (N=20 spectra)
Pixel Variance
Median Variance: 7.09
Variance (counts²)
Wavenumber (cm⁻¹)
c) Distribution of variance
Cumulative Probability
Variance (counts²)
Acquisition Time
2s
5s
10s
15s
30s
60s
120s
d)
Read Noise (σR): 2.410 ± 0.008 counts
Dark Rate (D): 0.0112 ± 0.0007 counts/s
Variance (counts²)
Acquisition Time t (s)
Linear Fit (R²=0.9784)
16/84th Quantile of all pixel variance

Supporting Fig. S19 – Estimating dark and read noise from pixel variance with the laser and room lights off. a-b) Variance of each pixel across 20 repeated acquisitions at 2s and 120s acquisition times. The larger number of high variance pixels at 120s reflects cosmic rays (large ones were removed, but small ones remain). c) Distribution of variance as a function of acquisition time. The median clearly increases, even though the distributions overlap. d) Estimating read noise and dark noise from the increase in median variance with acquisition time. The fact that the trend is so subtle relative to the spread of each acquisition time indicates that dark noise is very small on this instrument.

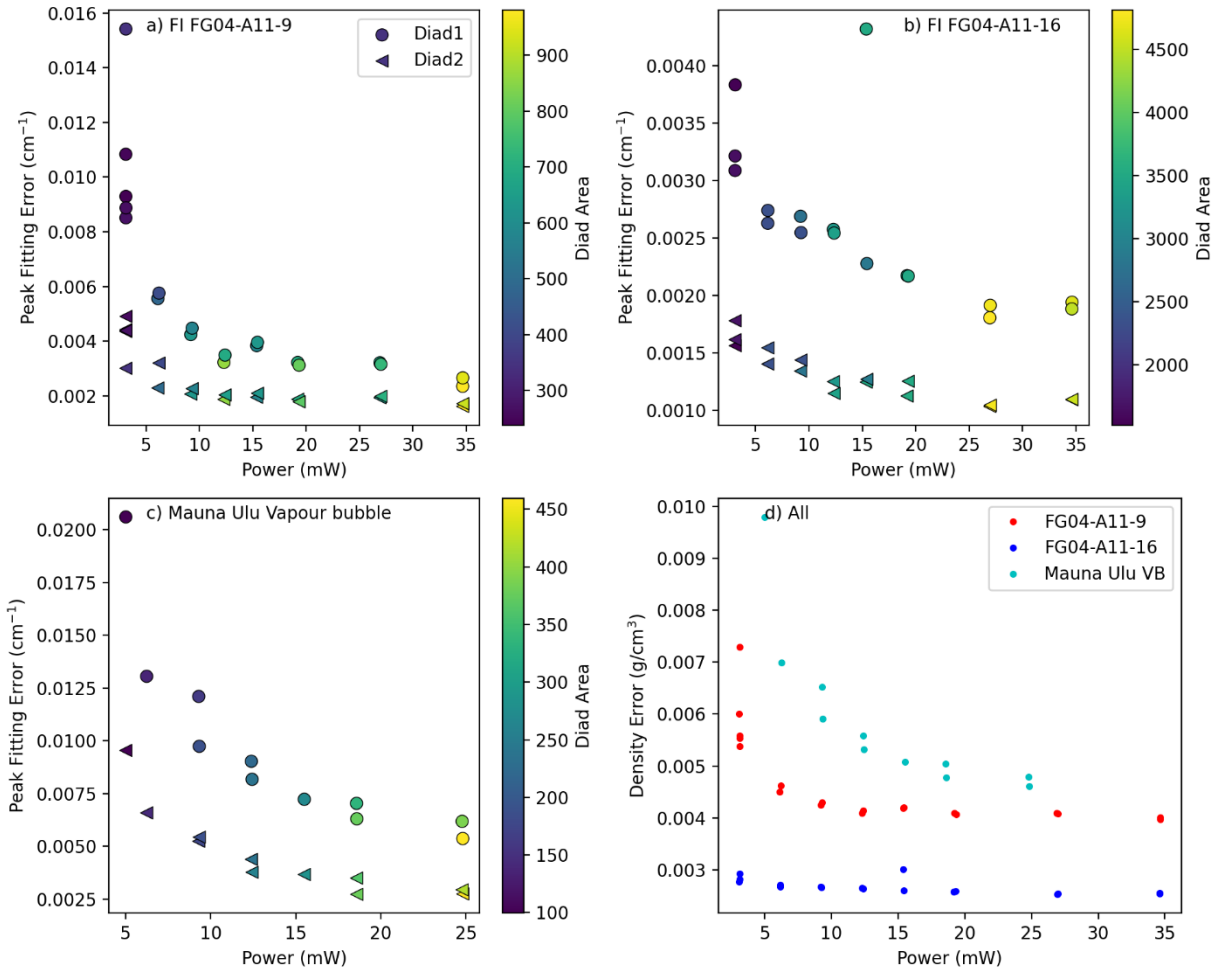

Supporting Figure S20– Change in peak fitting errors with increasing laser power. a-b) There is a clear drop in the peak fitting error for diad1 and diad2 as laser power is increased for Fogo fluid inclusion (FG04-A11-9), and for a melt inclusion vapour bubble from Mauna Ulu, Kīlauea (Wieser et al., 2019). (c). d) Same datasets but showing the error in calculated density. Laser power is at the sample, calculated from the TruePower reading multiplied by the correction factors for each objective measured using the laser power meter. This is true for all subsequent plots in this supplement.

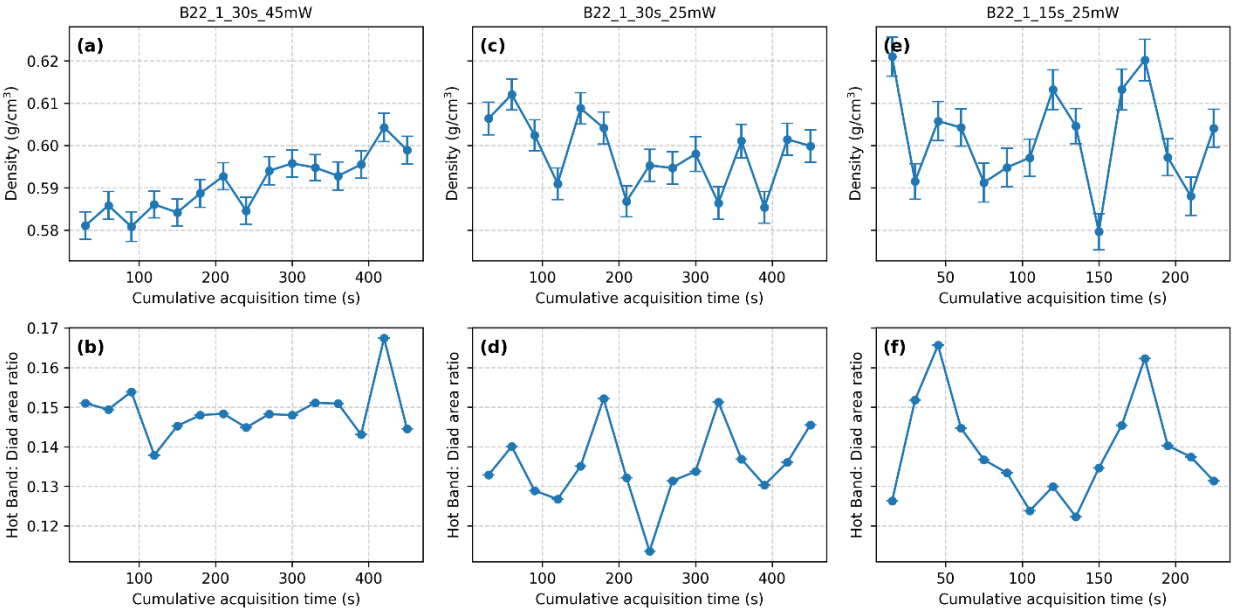
B22_1_30s_45mW
B22_1_30s_25mW
B22_1_15s_25mW
(a)
(c)
(e)
(b)
(d)
(f)
Density (g/cm³)
Hot Band: Diad area ratio
Cumulative acquisition time (s)

198

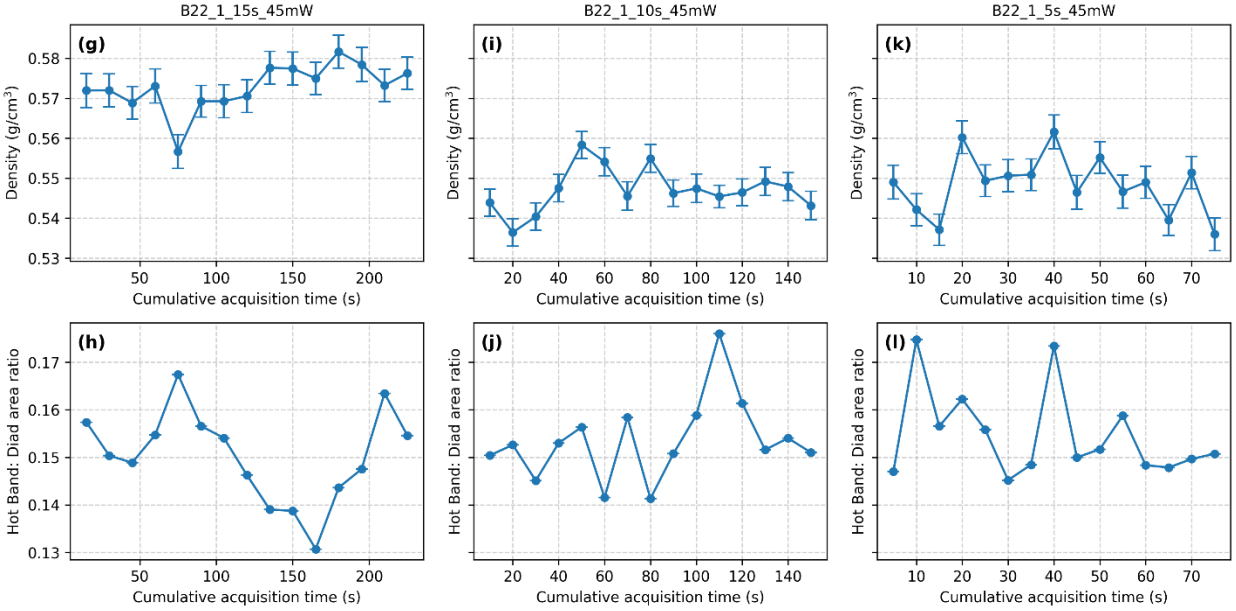
B22_1_15s_45mW
B22_1_10s_45mW
B22_1_5s_45mW
(g)
(i)
(k)
(h)
(j)
(l)
Density (g/cm³)
Hot Band: Diad area ratio
Cumulative acquisition time (s)

199

200

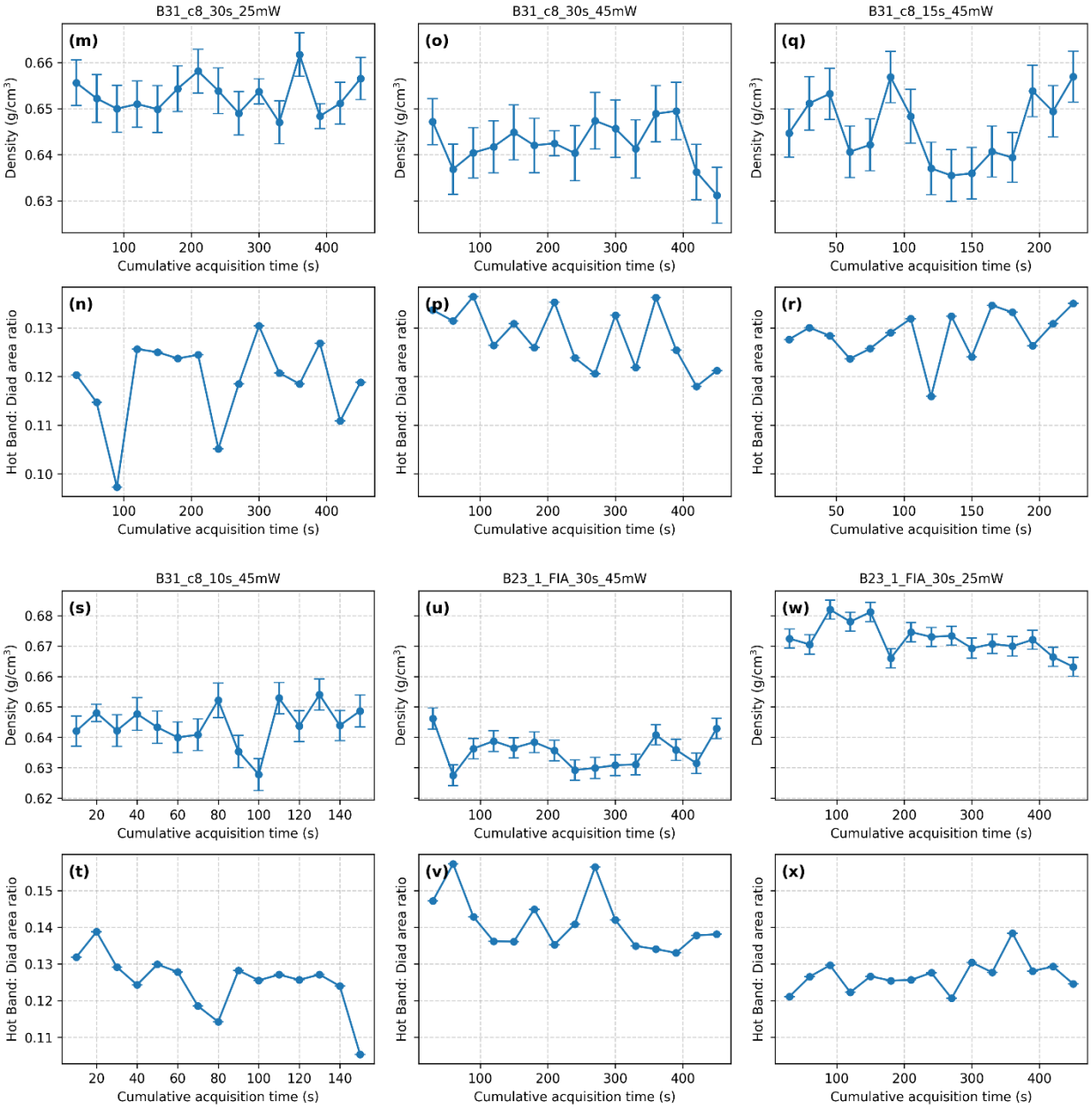

201

202

203 **Supporting Fig. S21** – Change in density and HB:diad area ratio from a WITEC slow series for
204 the acquisition times and laser powers shown in the title to investigate how long it takes a sample
205 to reach steady state. For example, the panel labelled B22_1_30s_45mW shows acquisitions
206 every 30s with the power set to 45 mW in the software using the TruePower meter. The laser is
207 continuously on during the acquisition. There is no clear change in these trends, indicating the
208 sample reaches a stable temperature very quickly after being exposed to the laser.

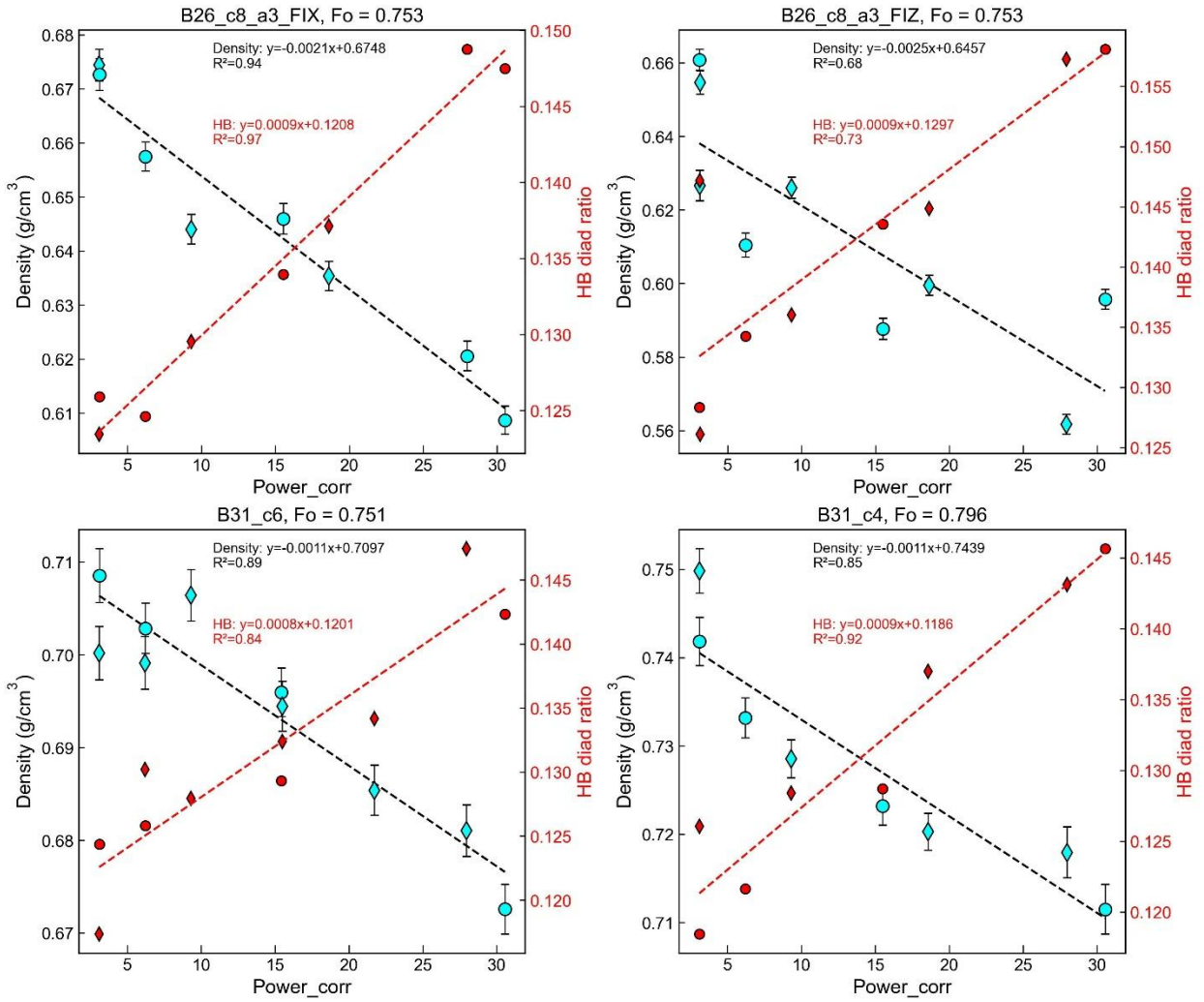

209

210 **Supporting Figure S22**–Comparison of Density vs. power, and HB:diad ratio vs power (defined
211 as (Area HB1 + Area HB2)/(Area Diad1 + Area of Diad2). The anticorrelation shows strong
212 evidence for laser heating.

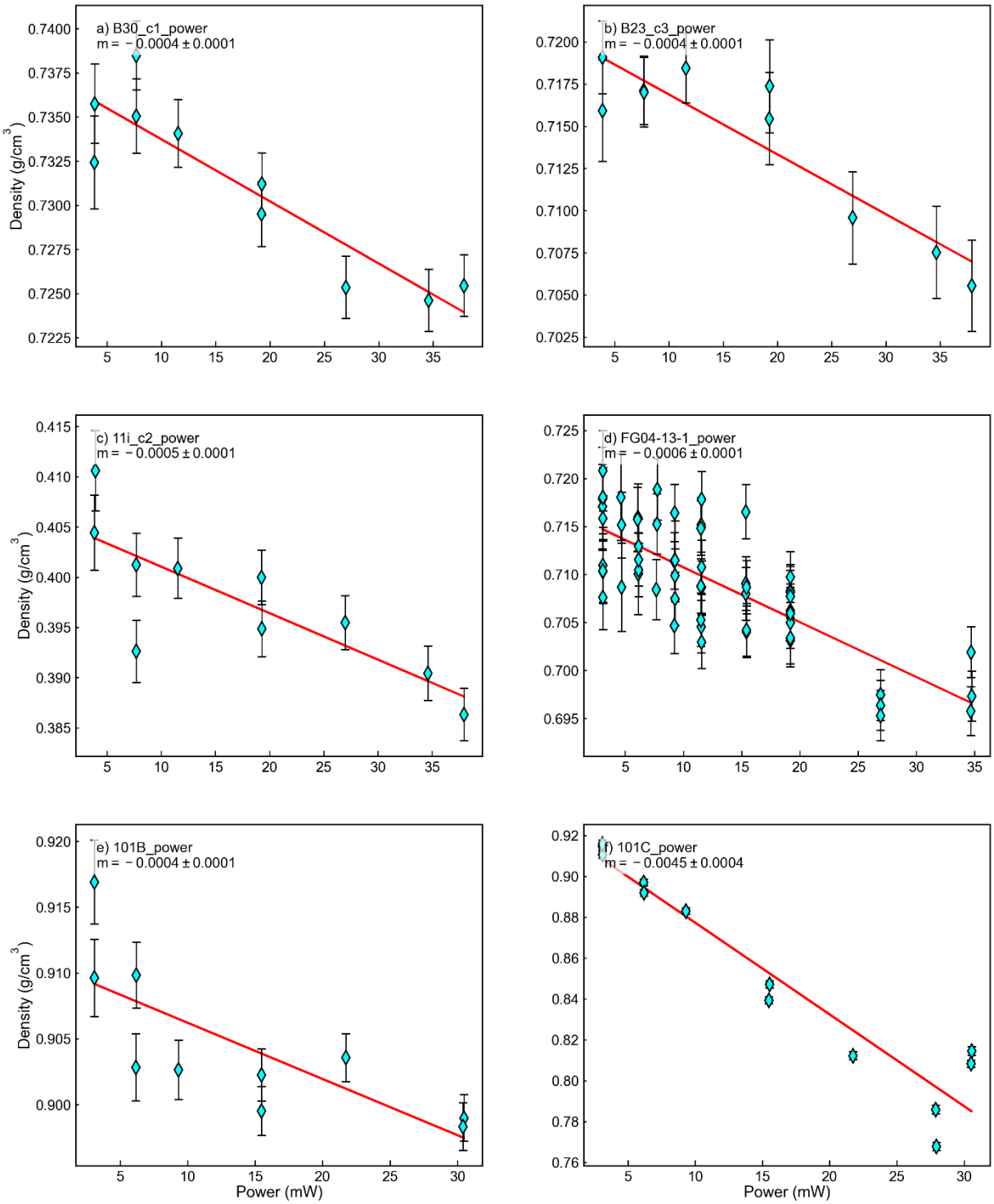
a) B30_c1_power
m = −0.0004 ± 0.0001
b) B23_c3_power
m = −0.0004 ± 0.0001
c) 11i_c2_power
m = −0.0005 ± 0.0001
d) FG04-13-1_power
m = −0.0006 ± 0.0001
e) 101B_power
m = −0.0004 ± 0.0001
f) 101C_power
m = −0.0045 ± 0.0004
Density (g/cm3)
Power (mW)

213

214

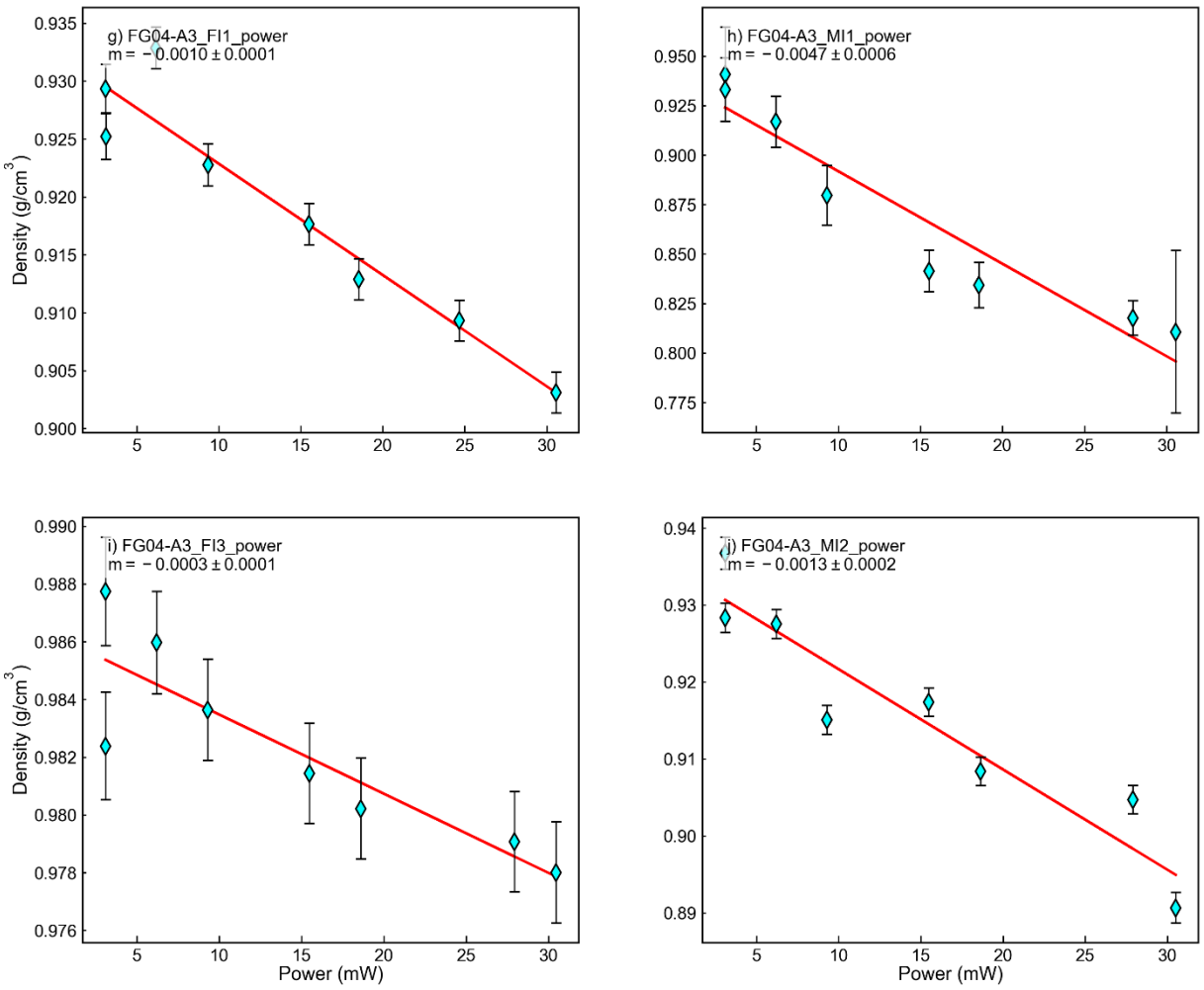

215

216 **Supporting Figure S23** – Power series for 10 FI/MI, 4 of which are shown in Fig. 14 of the main
217 text. The gradient and error on the slope is shown.

218

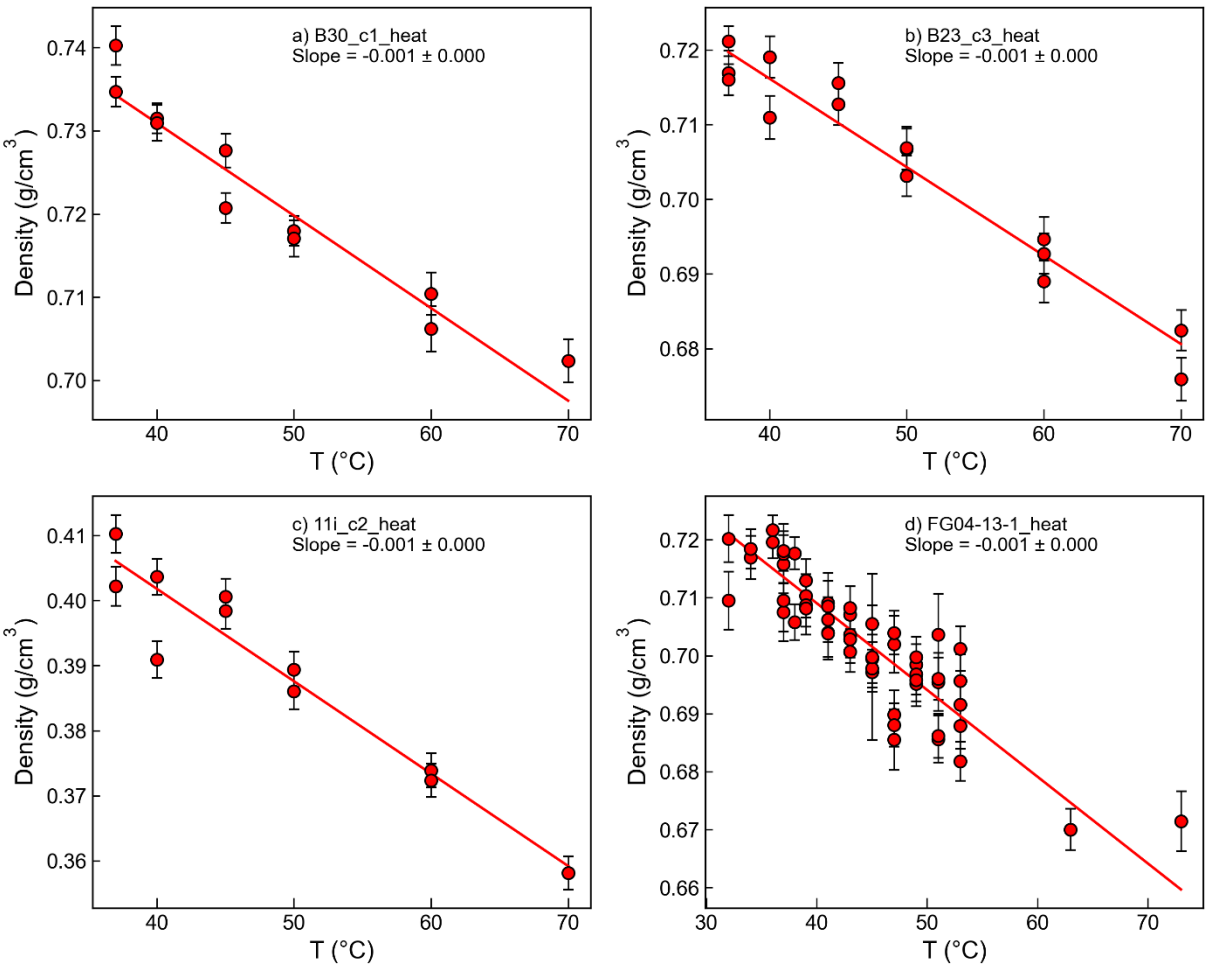
a) B30_c1_heat
Slope = -0.001 ± 0.000
b) B23_c3_heat
Slope = -0.001 ± 0.000
c) 11i_c2_heat
Slope = -0.001 ± 0.000
d) FG04-13-1_heat
Slope = -0.001 ± 0.000
Density (g/cm3)
T (°C)

219

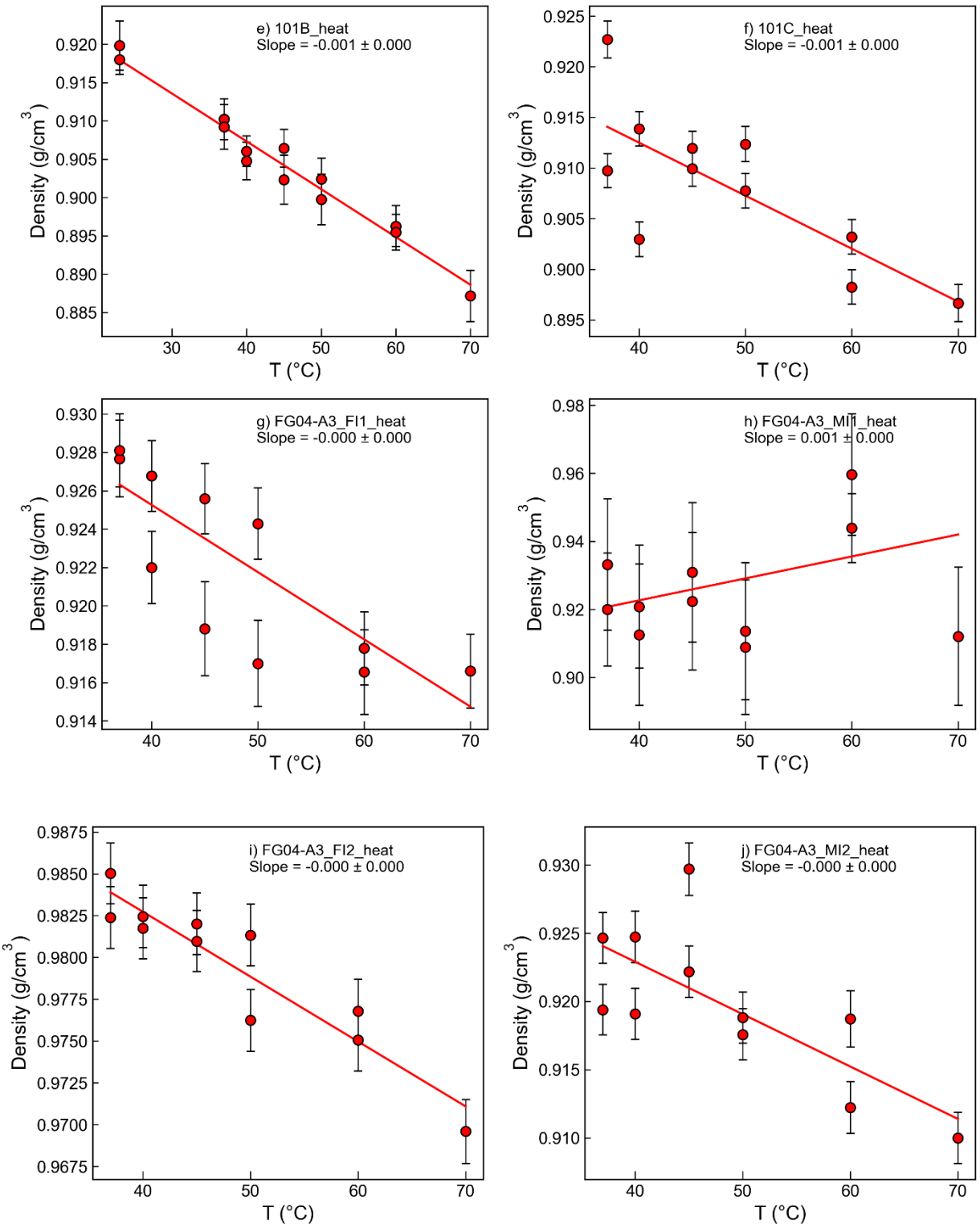

220

221

222 **Supporting Figure S24** – Heating series for 10 FI/MI, 4 of which are shown in Fig. 14 of the main
223 text. The gradient and error on the slope is shown.

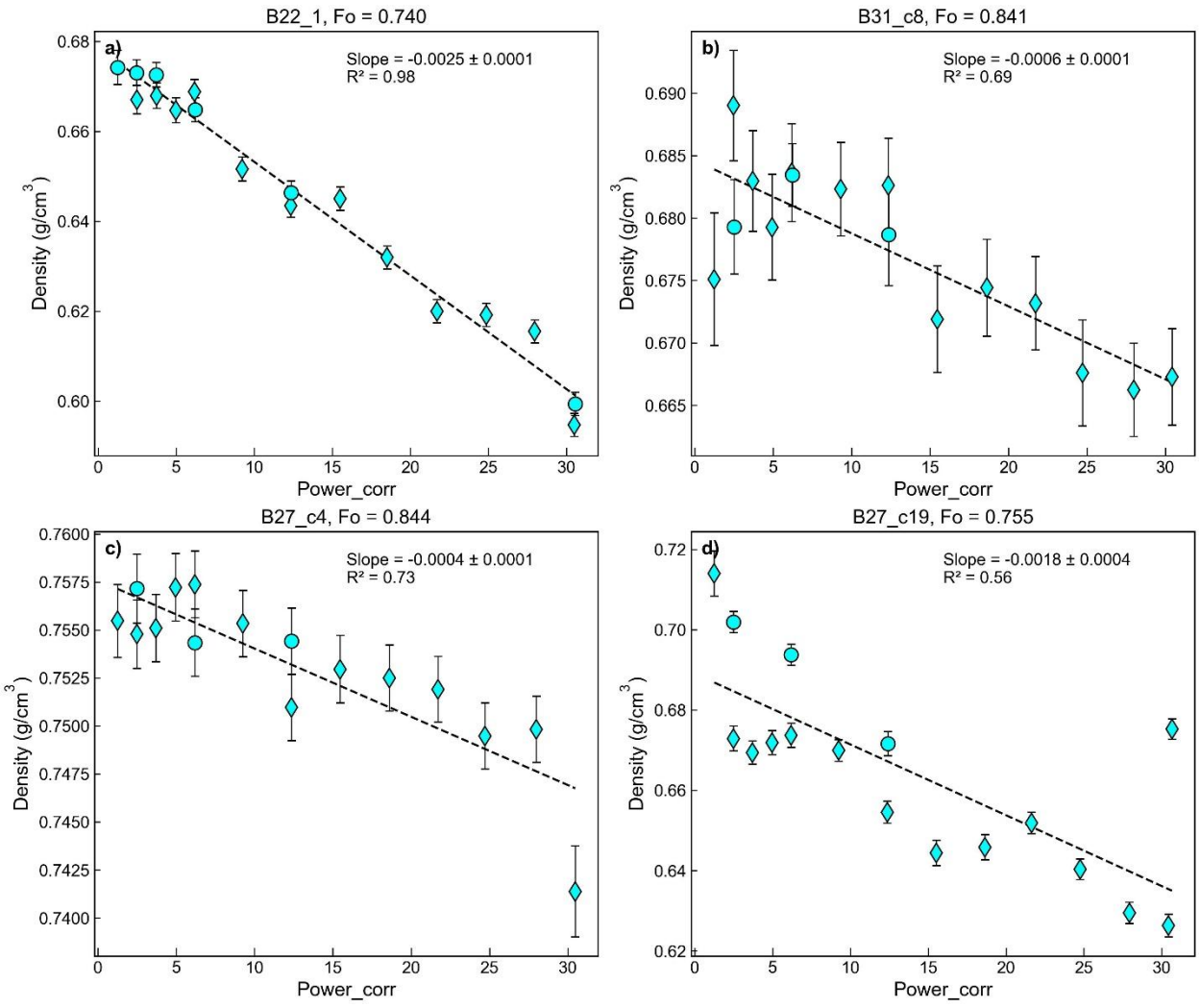
B22_1, Fo = 0.740
a)
Slope = -0.0025 ± 0.0001
R² = 0.98
Density (g/cm3)
Power_corr
B31_c8, Fo = 0.841
b)
Slope = -0.0006 ± 0.0001
R² = 0.69
Density (g/cm3)
Power_corr
B27_c4, Fo = 0.844
c)
Slope = -0.0004 ± 0.0001
R² = 0.73
Density (g/cm3)
Power_corr
B27_c19, Fo = 0.755
d)
Slope = -0.0018 ± 0.0004
R² = 0.56
Density (g/cm3)
Power_corr

224

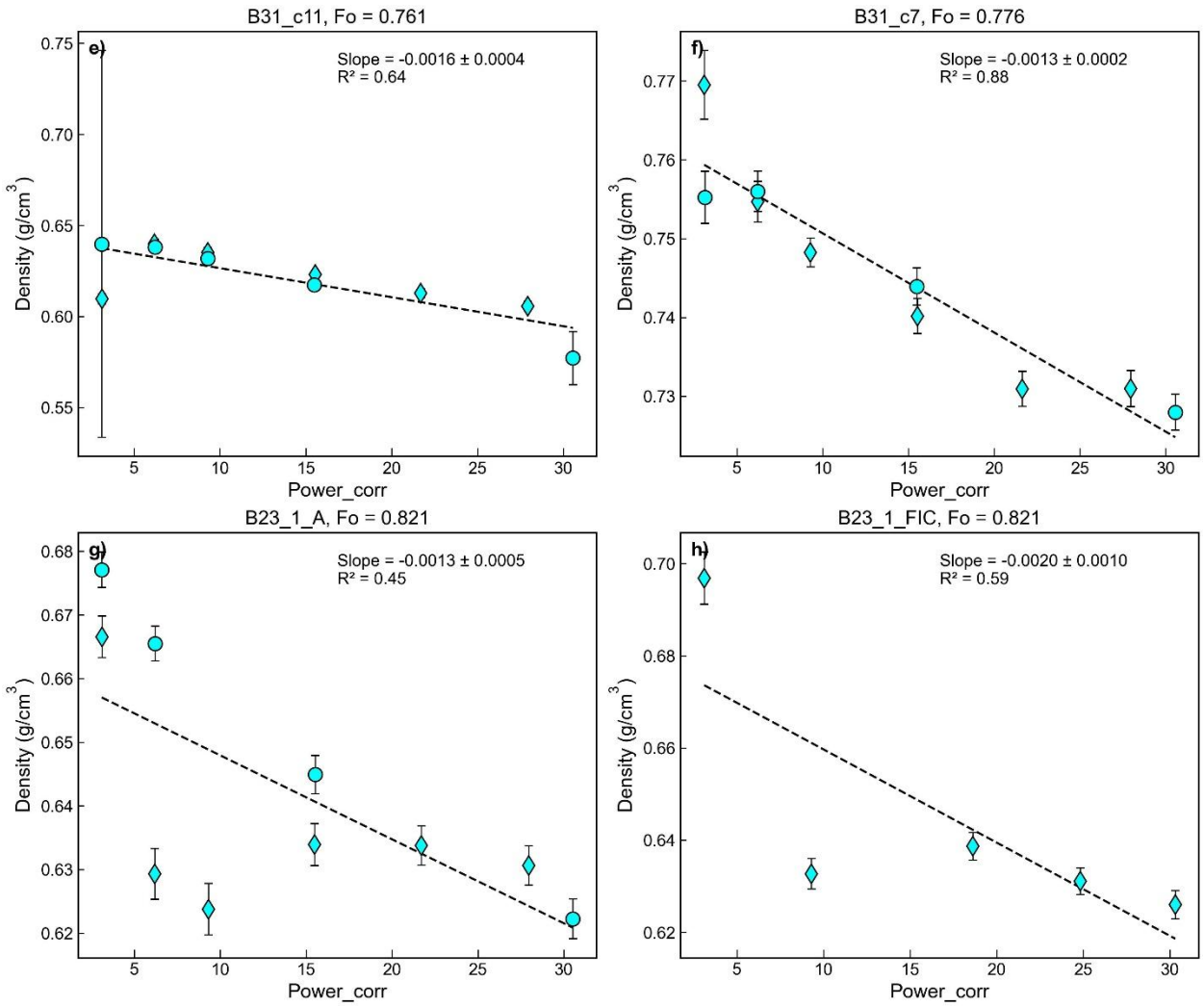
B31_c11, Fo = 0.761
e)
Slope = -0.0016 ± 0.0004
R² = 0.64
Density (g/cm 3)
Power_corr
B31_c7, Fo = 0.776
f)
Slope = -0.0013 ± 0.0002
R² = 0.88
Density (g/cm 3)
Power_corr
B23_1_A, Fo = 0.821
g)
Slope = -0.0013 ± 0.0005
R² = 0.45
Density (g/cm 3)
Power_corr
B23_1_FIC, Fo = 0.821
h)
Slope = -0.0020 ± 0.0010
R² = 0.59
Density (g/cm 3)
Power_corr

225

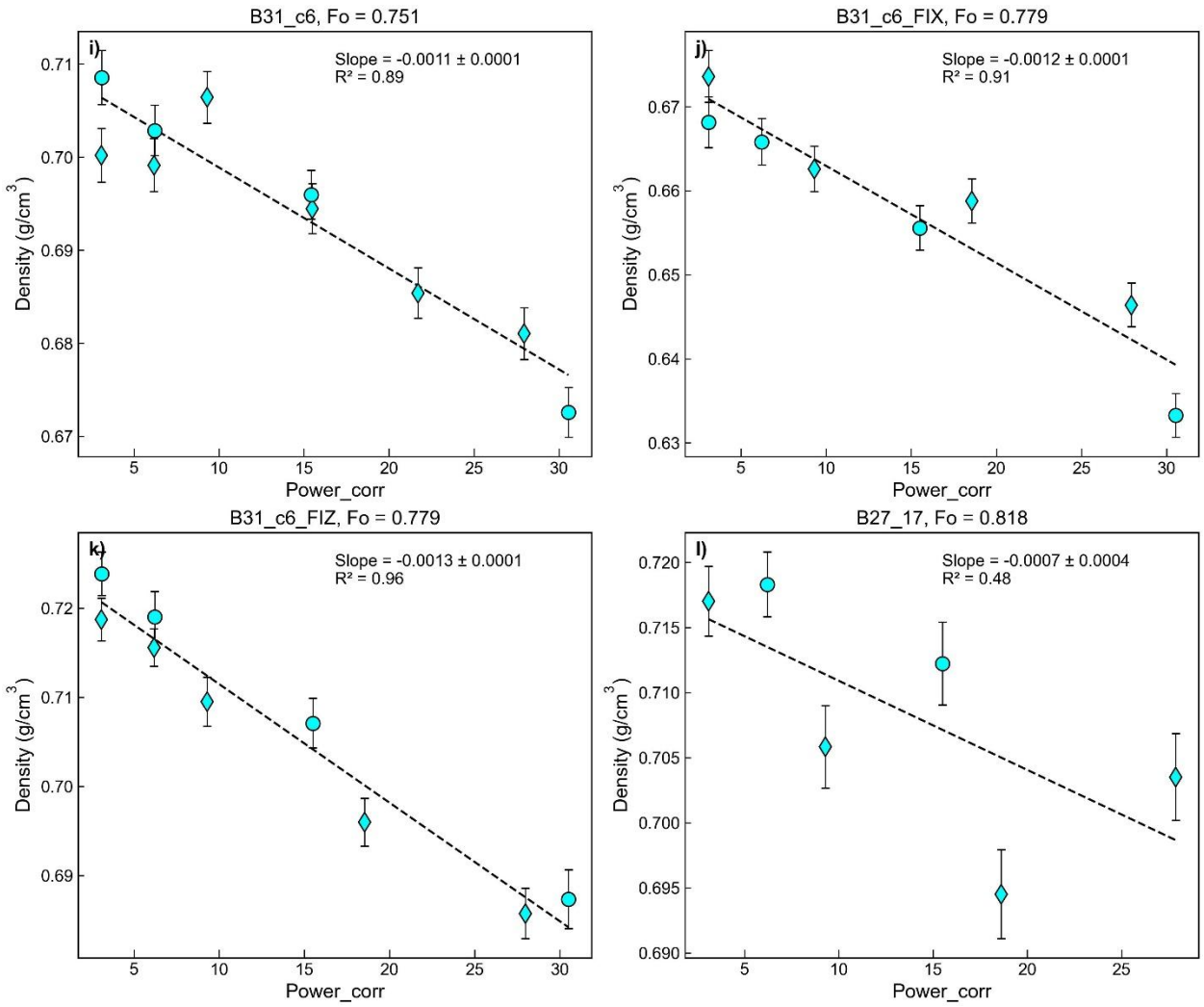
B31_c6, Fo = 0.751
i)
Slope = -0.0011 ± 0.0001
R² = 0.89
Density (g/cm3)
Power_corr
B31_c6_FIX, Fo = 0.779
j)
Slope = -0.0012 ± 0.0001
R² = 0.91
Density (g/cm3)
Power_corr
B31_c6_FIZ, Fo = 0.779
k)
Slope = -0.0013 ± 0.0001
R² = 0.96
Density (g/cm3)
Power_corr
B27_17, Fo = 0.818
l)
Slope = -0.0007 ± 0.0004
R² = 0.48
Density (g/cm3)
Power_corr

226

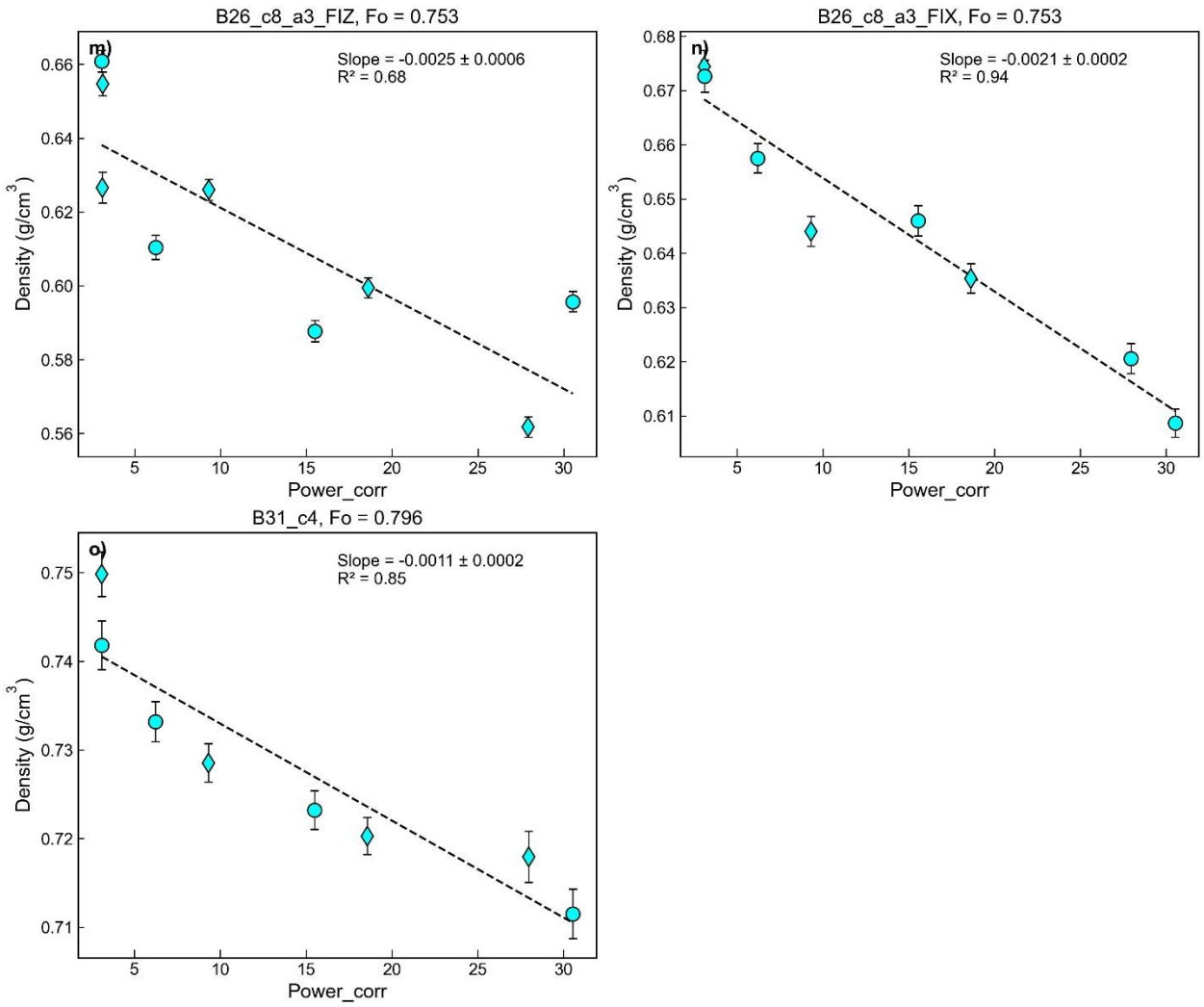

227

228 **Supporting Figure S25** – Power series for Icelandic fluid inclusions with known Fo contents. The
229 gradient, Fo content, and R^2 value is shown.

230

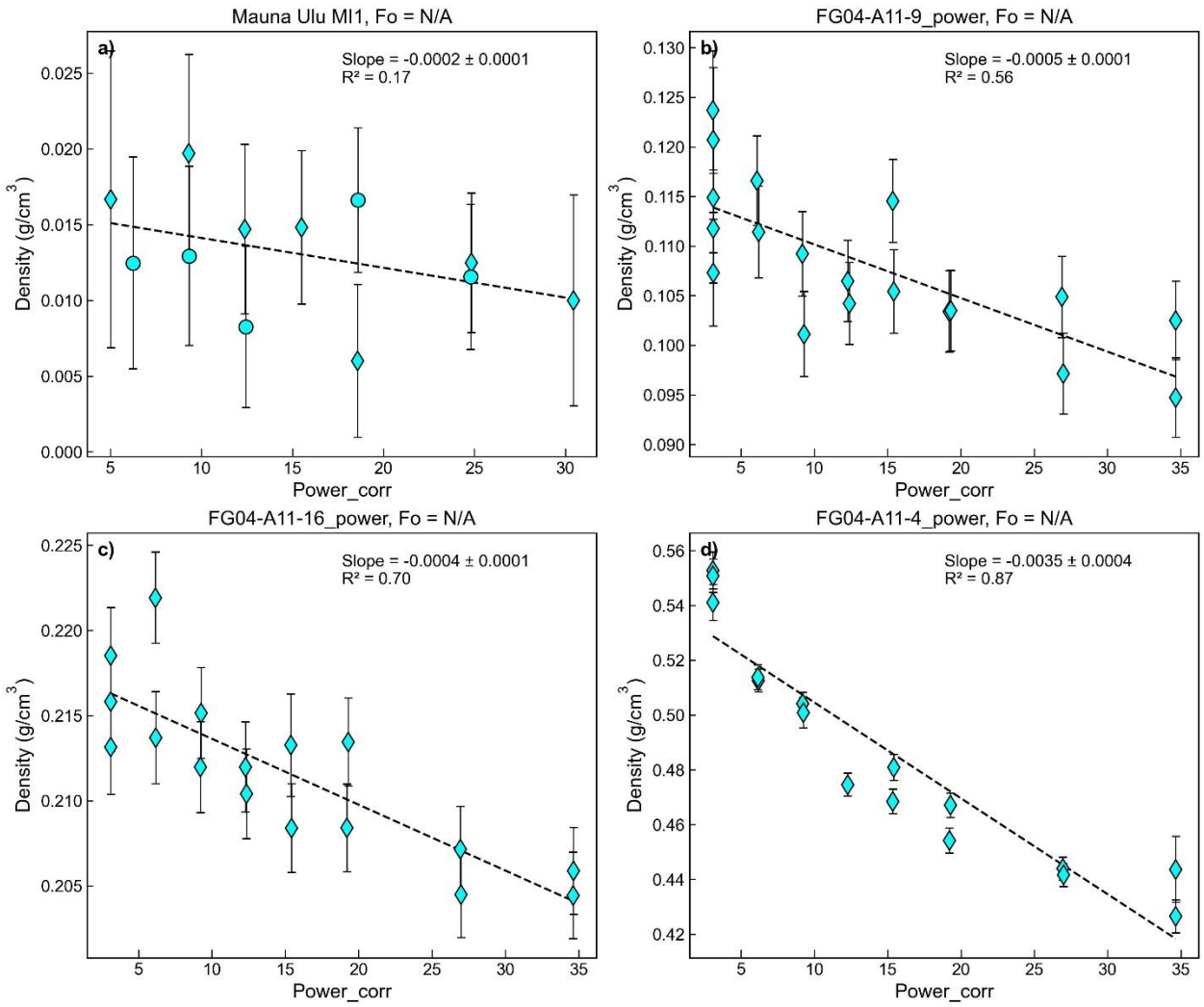
Mauna Ulu MI1, Fo = N/A
a)
Slope = -0.0002 ± 0.0001
R² = 0.17
Density (g/cm3)
Power_corr
FG04-A11-9_power, Fo = N/A
b)
Slope = -0.0005 ± 0.0001
R² = 0.56
Density (g/cm3)
Power_corr
FG04-A11-16_power, Fo = N/A
c)
Slope = -0.0004 ± 0.0001
R² = 0.70
Density (g/cm3)
Power_corr
FG04-A11-4_power, Fo = N/A
d)
Slope = -0.0035 ± 0.0004
R² = 0.87
Density (g/cm3)
Power_corr

231

232

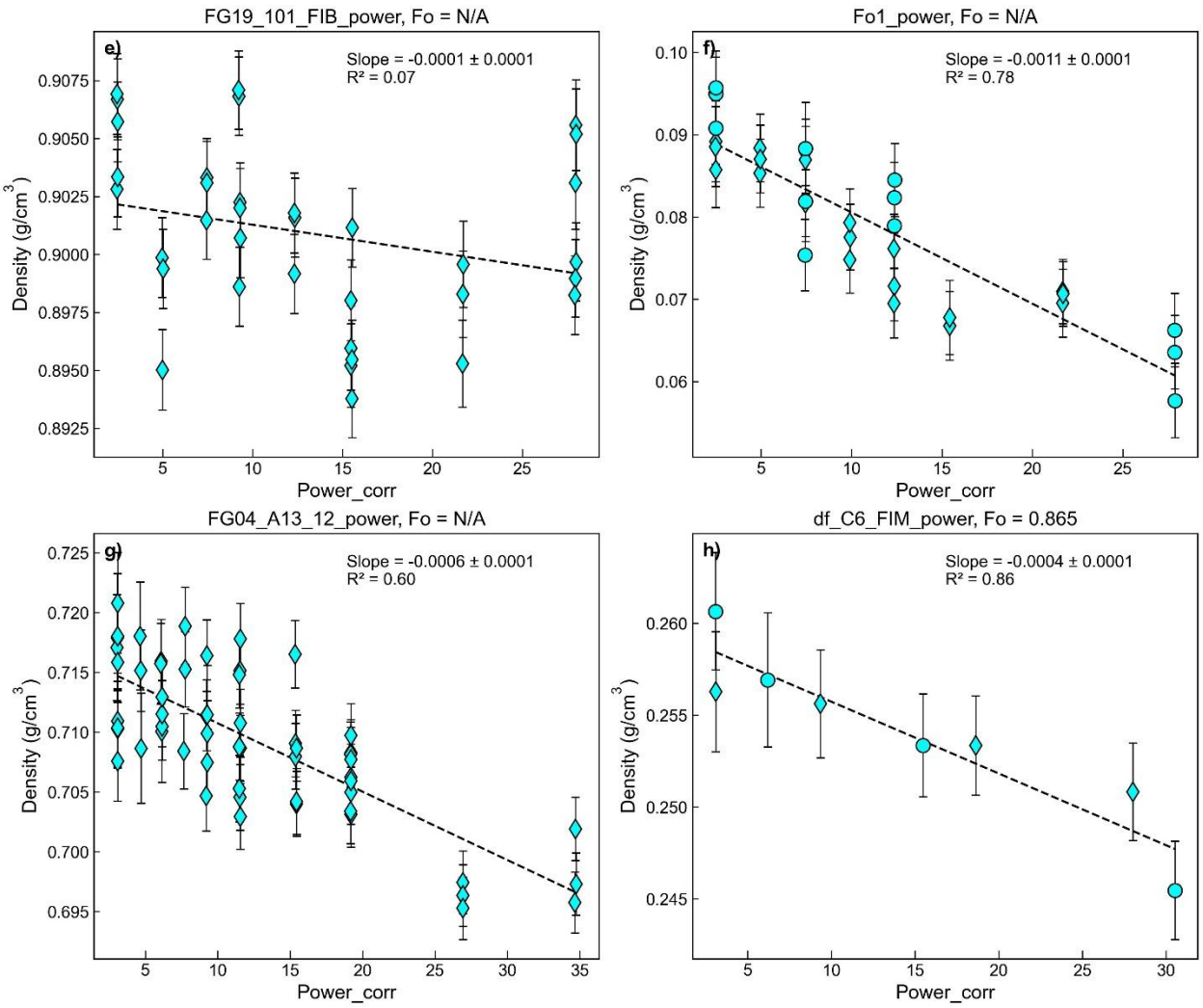
FG19_101_FIB_power, Fo = N/A
e)
Slope = -0.0001 ± 0.0001
R² = 0.07
Density (g/cm3)
Power_corr
Fo1_power, Fo = N/A
f)
Slope = -0.0011 ± 0.0001
R² = 0.78
Density (g/cm3)
Power_corr
FG04_A13_12_power, Fo = N/A
g)
Slope = -0.0006 ± 0.0001
R² = 0.60
Density (g/cm3)
Power_corr
df_C6_FIM_power, Fo = 0.865
h)
Slope = -0.0004 ± 0.0001
R² = 0.86
Density (g/cm3)
Power_corr

233

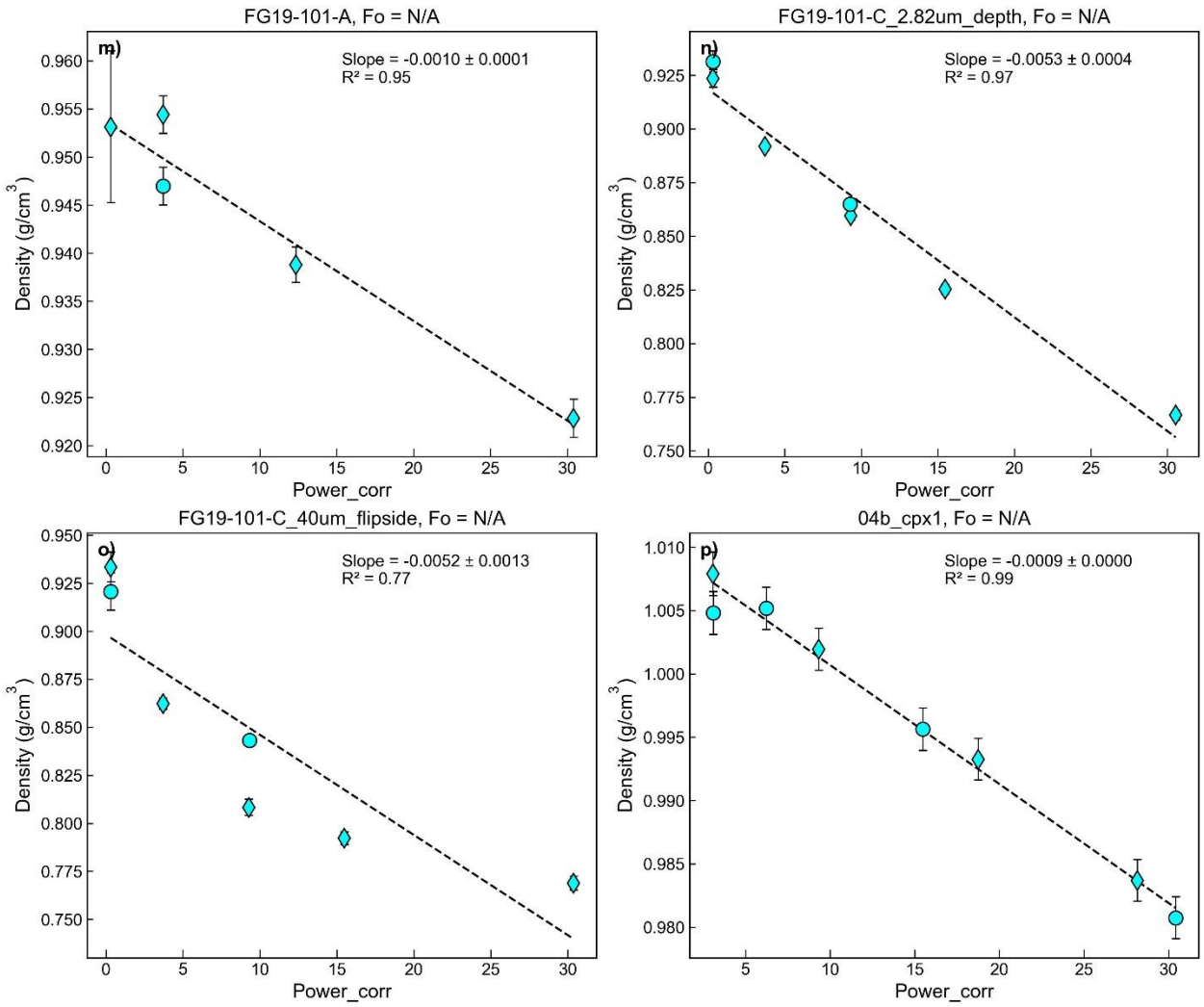
FG19-101-A, Fo = N/A
m)
Slope = -0.0010 ± 0.0001
R² = 0.95
Density (g/cm3)
Power_corr
FG19-101-C_2.82um_depth, Fo = N/A
n)
Slope = -0.0053 ± 0.0004
R² = 0.97
Density (g/cm3)
Power_corr
FG19-101-C_40um_flipside, Fo = N/A
o)
Slope = -0.0052 ± 0.0013
R² = 0.77
Density (g/cm3)
Power_corr
04b_cpx1, Fo = N/A
p)
Slope = -0.0009 ± 0.0000
R² = 0.99
Density (g/cm3)
Power_corr

234

235

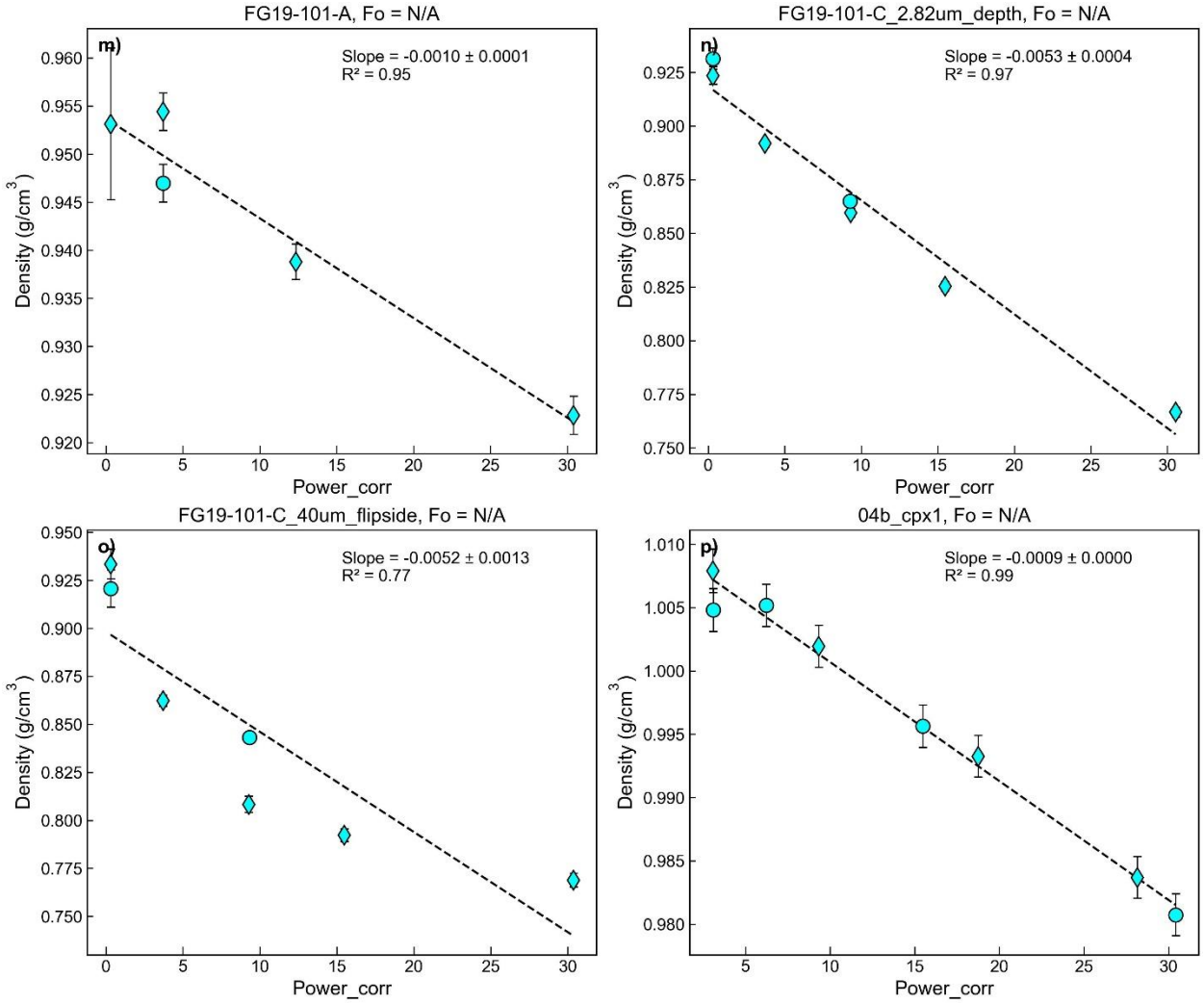
FG19-101-A, Fo = N/A
m)
Slope = -0.0010 ± 0.0001
R² = 0.95
Density (g/cm3)
Power_corr
FG19-101-C_2.82um_depth, Fo = N/A
n)
Slope = -0.0053 ± 0.0004
R² = 0.97
Density (g/cm3)
Power_corr
FG19-101-C_40um_flipside, Fo = N/A
o)
Slope = -0.0052 ± 0.0013
R² = 0.77
Density (g/cm3)
Power_corr
04b_cpx1, Fo = N/A
p)
Slope = -0.0009 ± 0.0000
R² = 0.99
Density (g/cm3)
Power_corr

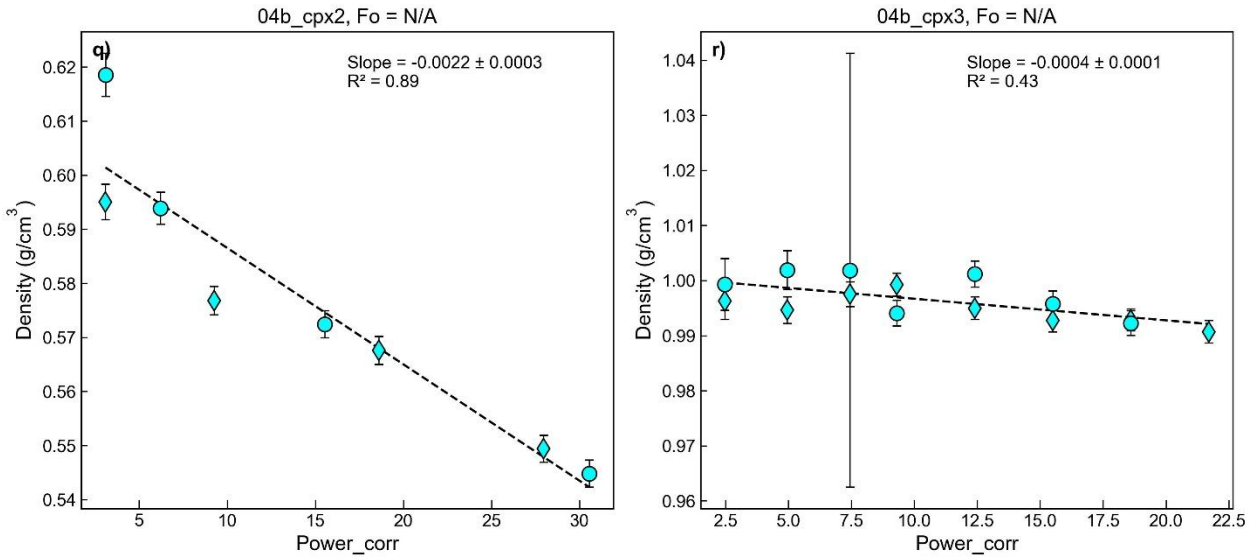

Supporting Figure S26 – Power series for all other fluid inclusions, and melt inclusions (a, f) shown in Fig. 12a of the main text.

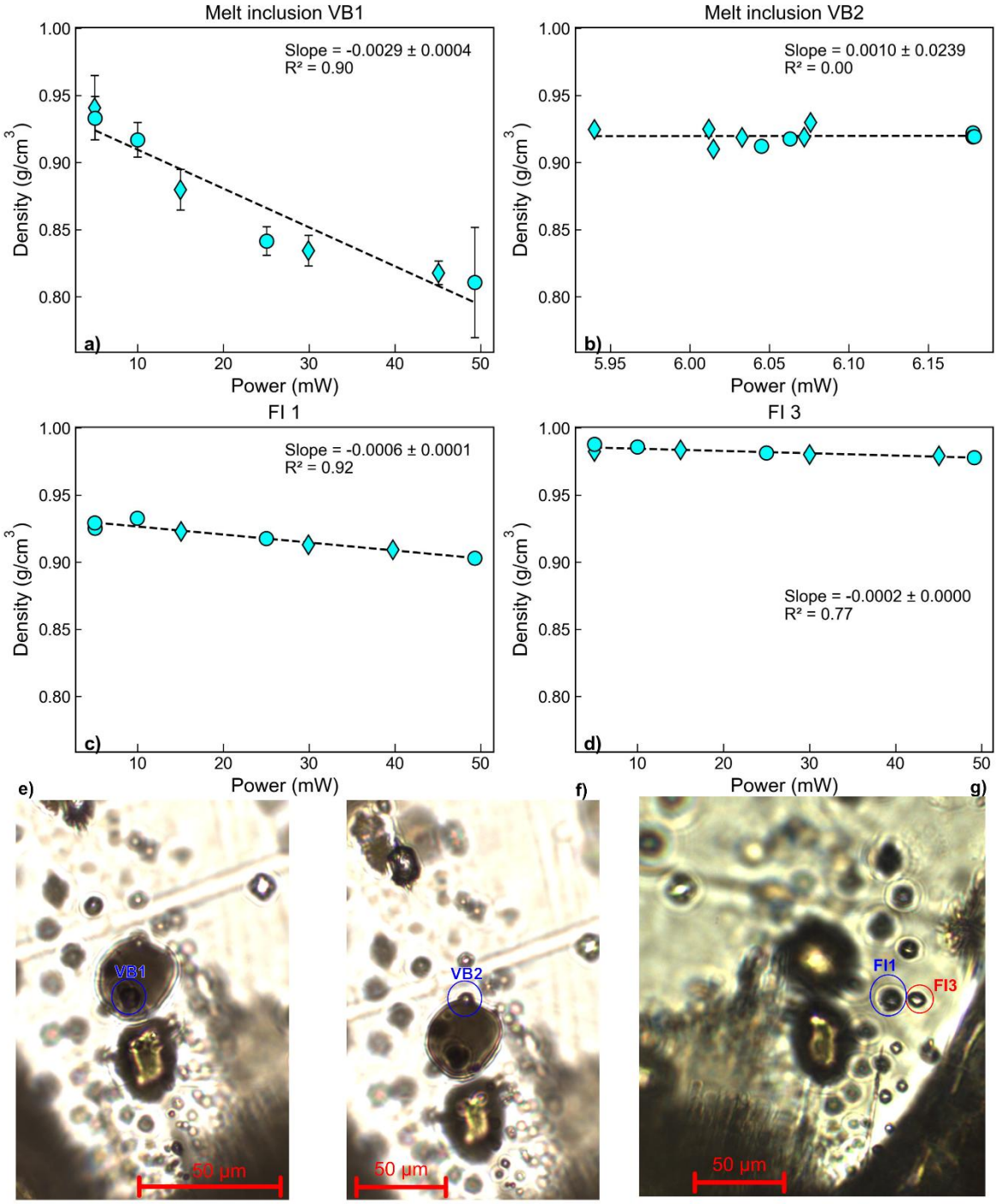

Supporting Figure S27 – Comparison of change in density as a function of laser power for two melt inclusion vapour bubbles and two fluid inclusions within the same crystal. VB1 is surrounded by melt (e) while VB2 is partially touching melt and partially touching olivine (f, see Supporting Fig. 11). The fact that VB2 is surrounded by olivine and melt accounts for its lower heating rate compared to VB1. It is noteworthy that the two FI, despite being in close proximity, show gradients that differ by a factor of 3.

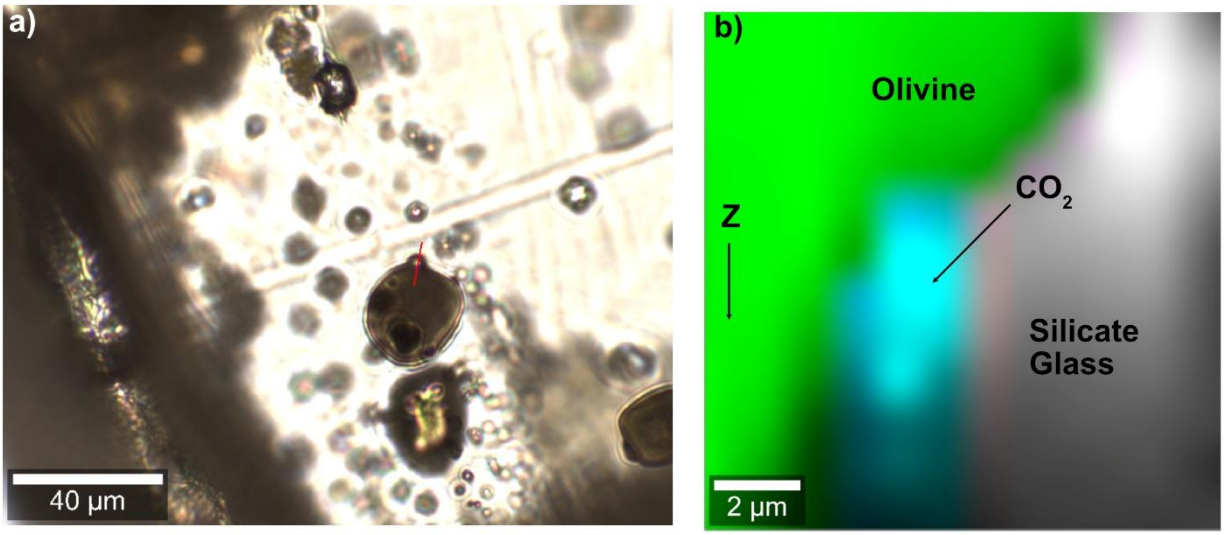

Supporting FigureS28– a) Transmitted light image of Bub2, with the red line showing the location of a vertical Raman map. b) Processed Raman map, showing that the bubble is partially touching the silicate glass of the melt inclusion (grey colors), partially touching the olivine (green). Map processed using the WITec software.

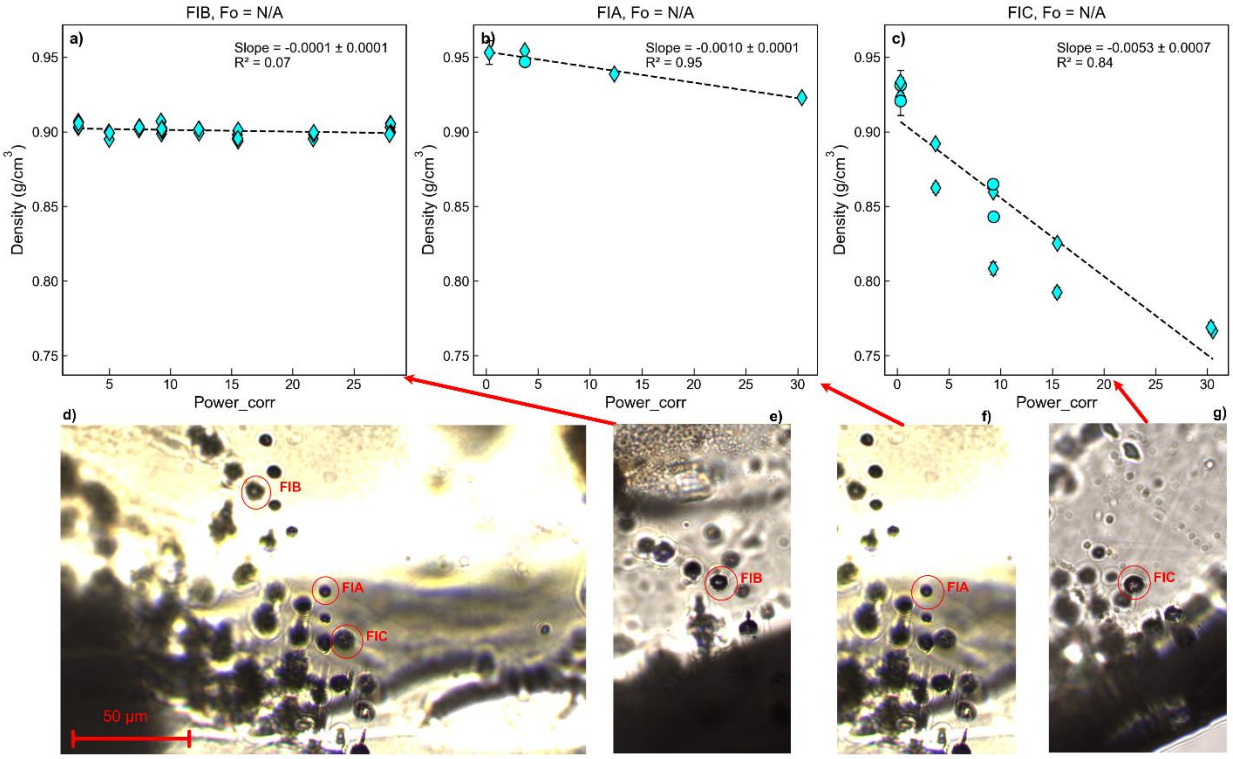

266

267 **Supporting Figure S29**. Comparison of change in density with increasing laser power (a-c) for 3
268 FI hosted within a single olivine crystal (FG19_101). d) Transmittted light image of the fluid
269 inclusion trail and the location of each FI. e-g) shows a focused picture of each FI. The scale is
270 the same for all pictures. Raman maps of A and C are shown in Supporting Figure 13.

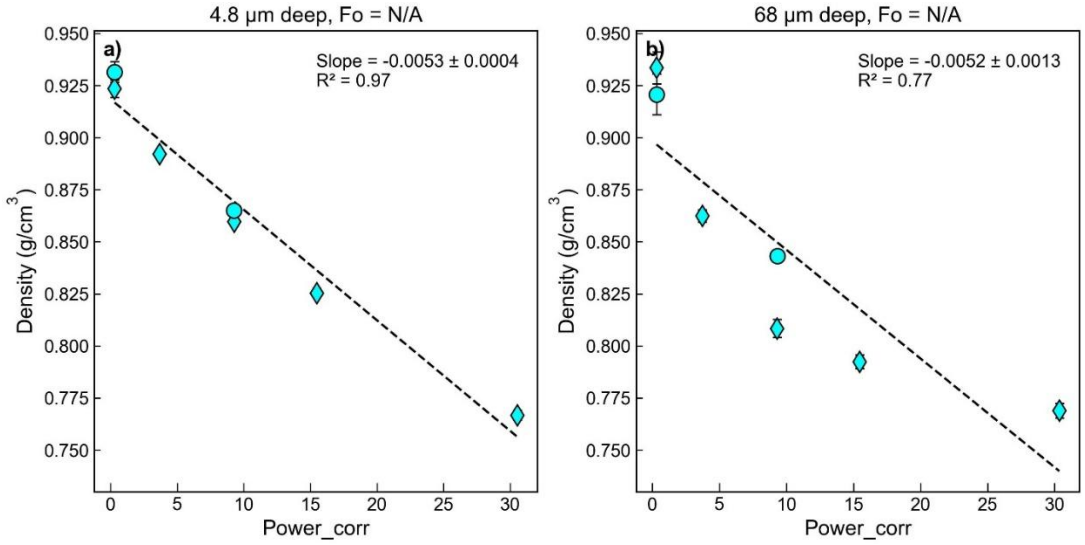

271

272 **Supporting Figure S30** – Comparison of heating rate for FI FG19-101C as a function of depth
273 below the surface. a) shows the heating rate when the FI was ~4.8 µm below the surface. The
274 crystal was then flipped over, and then a power series was conducted from the other side, such
275 that the FI was ~68 µm below the surface. The gradients of these series is within error of each
276 other. This supports the modelling work of Hagiwara et al. (2021) suggesting that depth in the
277 sample doesn't strongly affect heating rate.

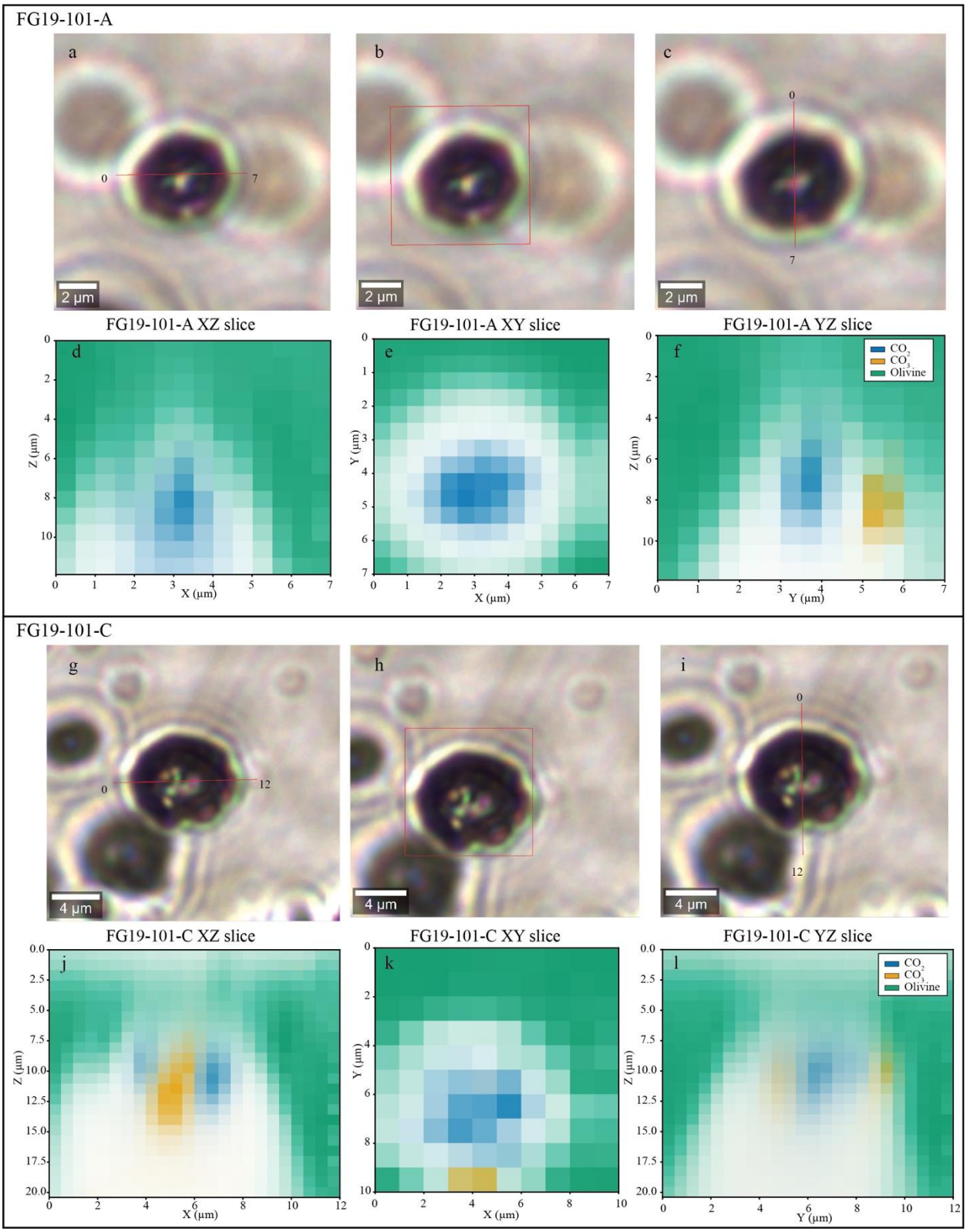

278

279 **Supporting Fig. S31**. Two dimensional Raman maps of FI FG19-101-A showing the presence
280 of CO_2 and carbonates in the FI. a-c) Transmitted light images of FG19-101-A. The red lines and
281 rectangles show the plane along which Raman mapping was conducted (shown in panels d-f). g-

i) Transmitted light images of FG19-101-A and corresponding 2D slice (red line). Both sets of Raman maps were collected using 50X objective, with a laser power of 49 mW, a integration time of 0.5 s, a 300 grooves/mm grating, and a 2350 cm-1 spectral center. Z dimension is recalculated accounting for the refraction index of olivine (1.7). In the Z slices, the bottom under the inclusions is white (very low intensity) due to loss of confocality at depth. Other white pixels are areas of highly mixed spectra which are difficult to reliably extract components from. Maps were processed using Ramanspy 0.2.10 (Georgiev et al., 2024). To produce the maps, we first denoise using savitzky golay filter with a window length of 4, and a polynomial of 3rd order, then apply ASLS baseline routine in Ramanspy and normalize each spectrum to using Min-Max normalization. We apply the whole preprocessing routine to all the maps. We extract "pure" endmember spectra for CO_2, CO_3 and Olivine from the map spectra and use Non-negative Constrained Least Squares (NNLS) abundance method in RamanSpy to extract abundance maps for each component at every pixel. These maps are not quantitative, but an approximation of the distribution of each component. It is evident that carbonate is much more abundant in 101-C than 101-A, though they are only ~20 um apart from each other (Supporting Fig. 11).

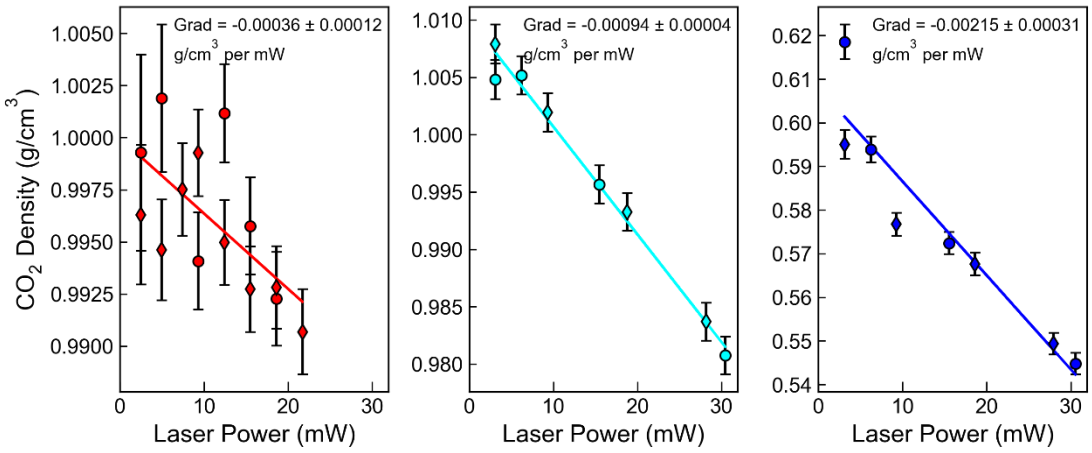

Supporting Figure S32 – Laser power series for ~Mg_{79}# clinopyroxenes for fluid inclusions from Gleeson et al. (2025). The gradient varies by a factor of ~3.8, despite the fact these samples are very chemically homogenous and there are no obvious color differences between the different crystals.

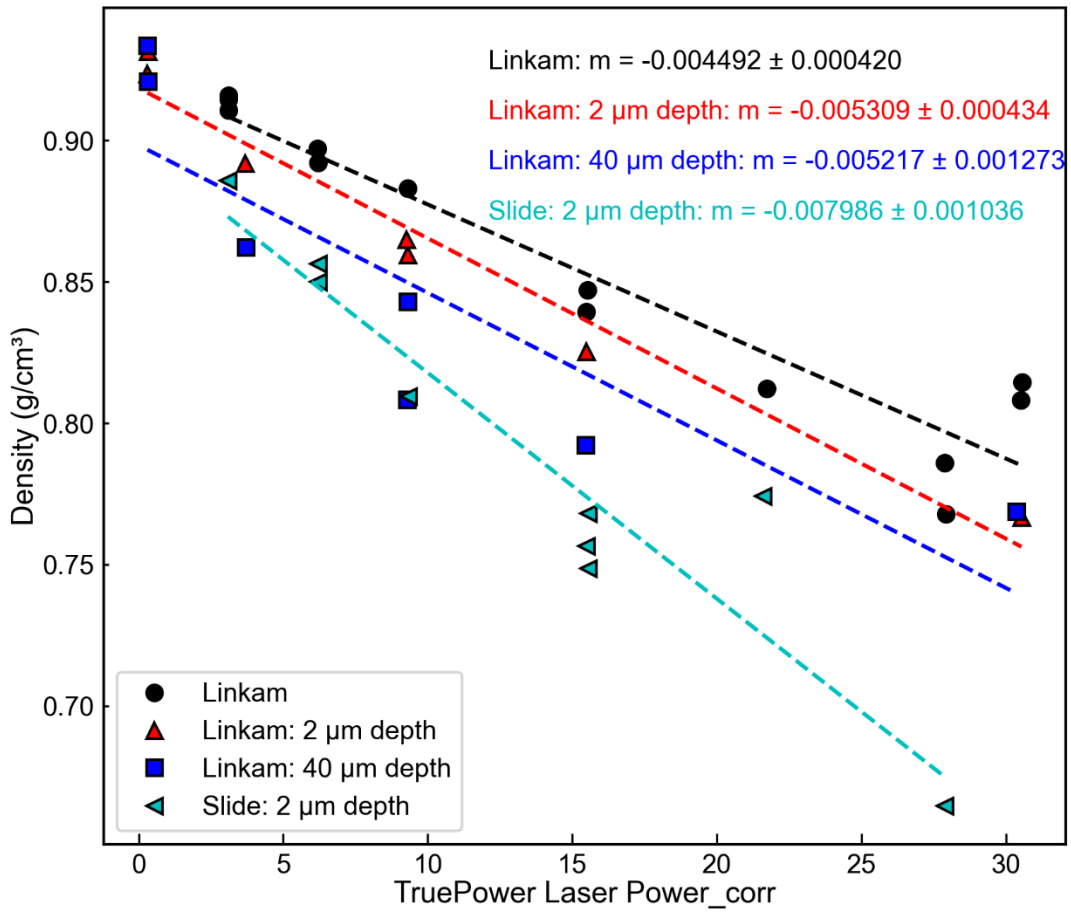

304

305 **Supporting Fig. S33** – Comparing heating rates for FG19_101C when the crystal is mounted in
306 the linkam stage (not surrounded by resin) at varying depths (black, red and blue), vs. when the
307 crystal is mounted on a glass slide in crystalbond resin (cyan colors).

308

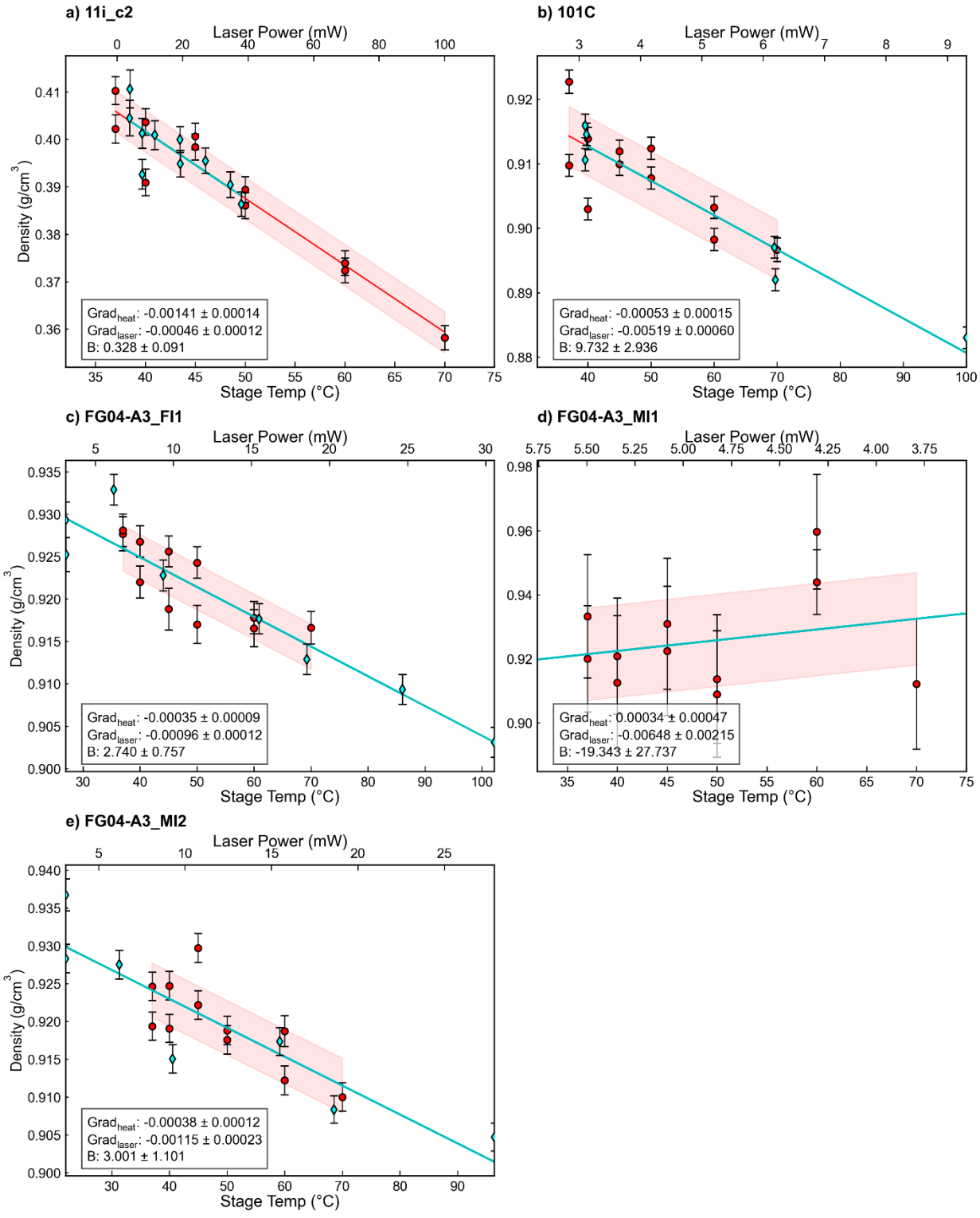

Supporting Figure S34 – Comparison of heating and power series as in Fig. 14 of the main text.

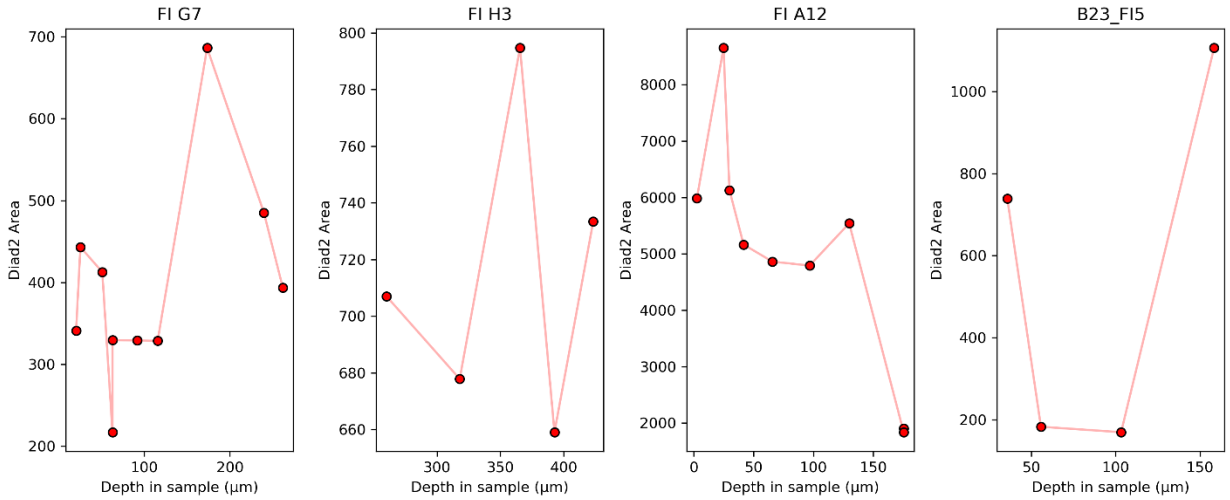

Supporting Figure S35– Changes in signal intensity as a function of depth in sample for 4 different olivine-hosted FI.

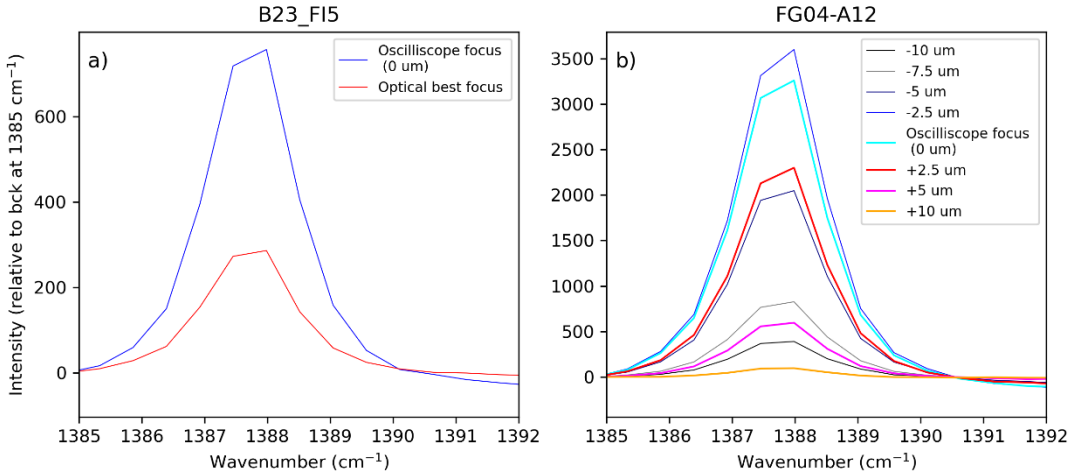

Supporting Figure S36 – Example of the effect of small focus changes on the intensity of diad 2. a) Compares the user-selected optical focus based on sharpness of the FI edges to the optimal focus position found by the oscilloscope. b) Compares the optimal focus position found by the oscilloscope to small perturbations from this position.

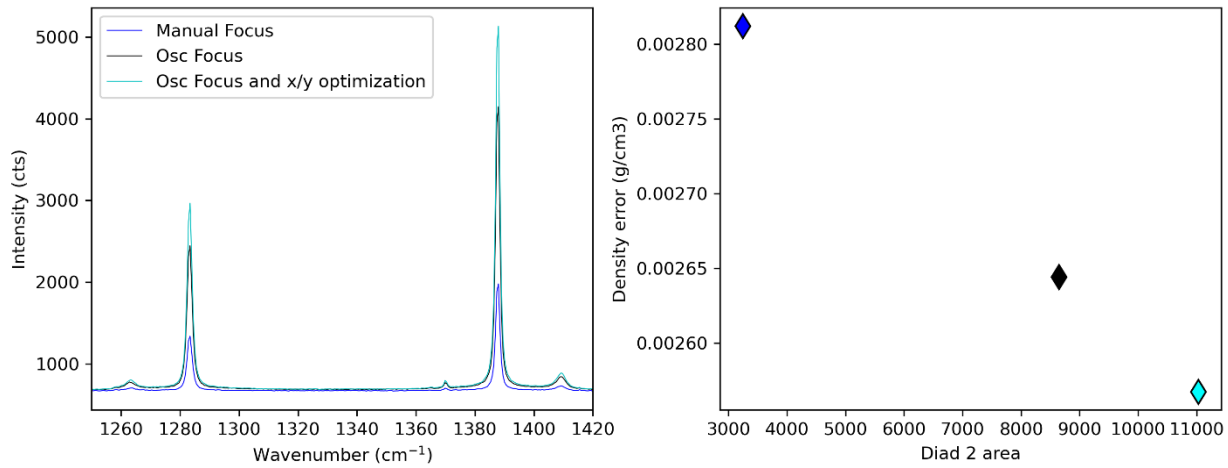

Supporting Fig. S37– Compares the user-selected optical focus based on sharpness of the FI edges to the optimal focus position found by the oscilloscope (dark blue), to the optimum Z position found by the oscilloscope (black), and the optimum Z and x-y position determined by Raman mapping for FG04-A12.

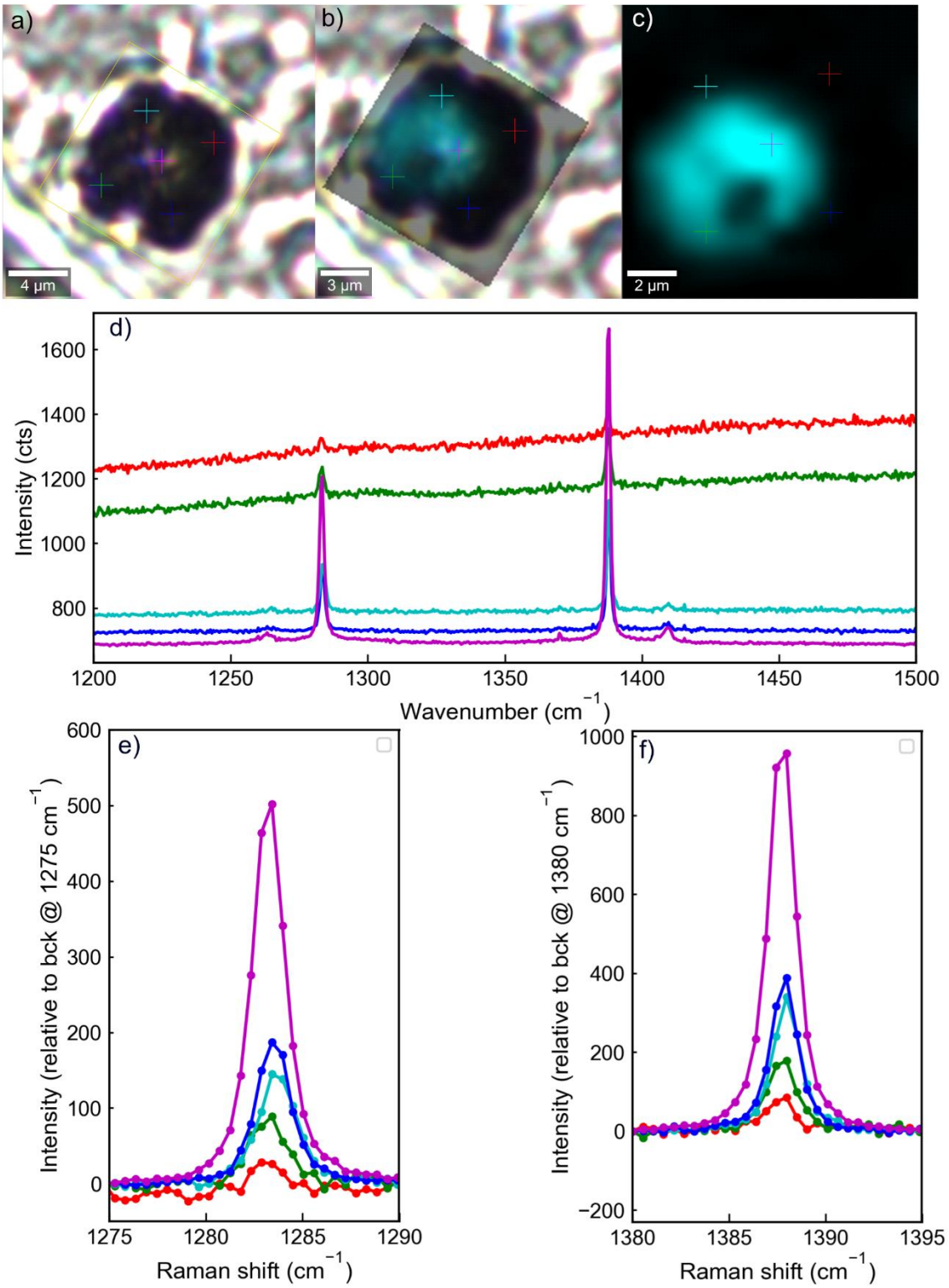

Supporting Figure S38 – Variation in signal intensity as a function of X-Y position within the fluid inclusion. a) Transmitted light image of fluid inclusion B23_FI5. The 5 colored crosses show the position of different spectral acquisitions shown in d-f. b) An 1800 g grating Raman map with the

intensity of the CO_2 signal shown as cyan colors overlain on this transmitted light image. c) shows the map with no underlay. d-f) Comparing the intensity of different acquisitions. While it is not surprising that the strongest signal is obtained from the center of the inclkusion, it is surprising that despite the cyan, red, green and blue cross being equidistance from the center, they yield vastly different intensities.

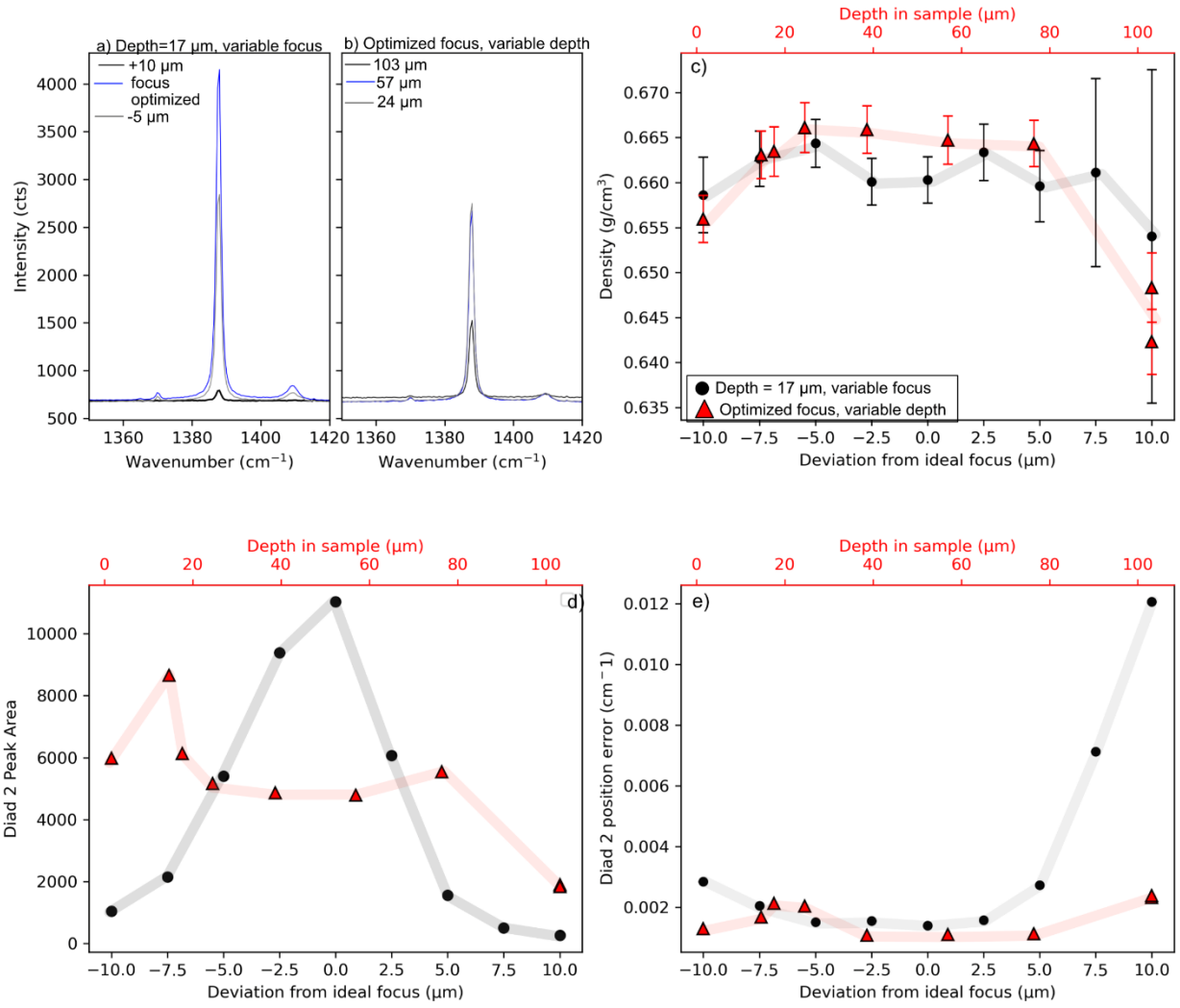

Supporting Figure S39 – Comparison of peak intensity and peak fitting errors with increasing depth in sample vs. a change in focus for FG04_A12. a) Spectra centered around diad2 showing the difference in intensity for the optimized focus (blue) vs. -5 µm deeper in the sample (grey) and 10 µm shallower (black). The fluid inclusion has a radius of ~7 µm. b) Change in intensity with depth of the fluid inclusion optimal focus below the sample. At 24 µm and 57 µm depth, the intensities are very similar, although they drop to above half for 103 µm depth. c) Change in density as a function of depth and ideal focus. Red triangles show variation in depth in sample (top red axis) and black circles show deviation from the ideal focus (black). Apart from the very worst focus and deepest depth, there is no change outside of uncertainty. Points are joined up

with lines to help separate the two series. d) Peak area of diad 2 (a measure of intensity) as a function of depth and focus. e) Error on the position of diad 2.

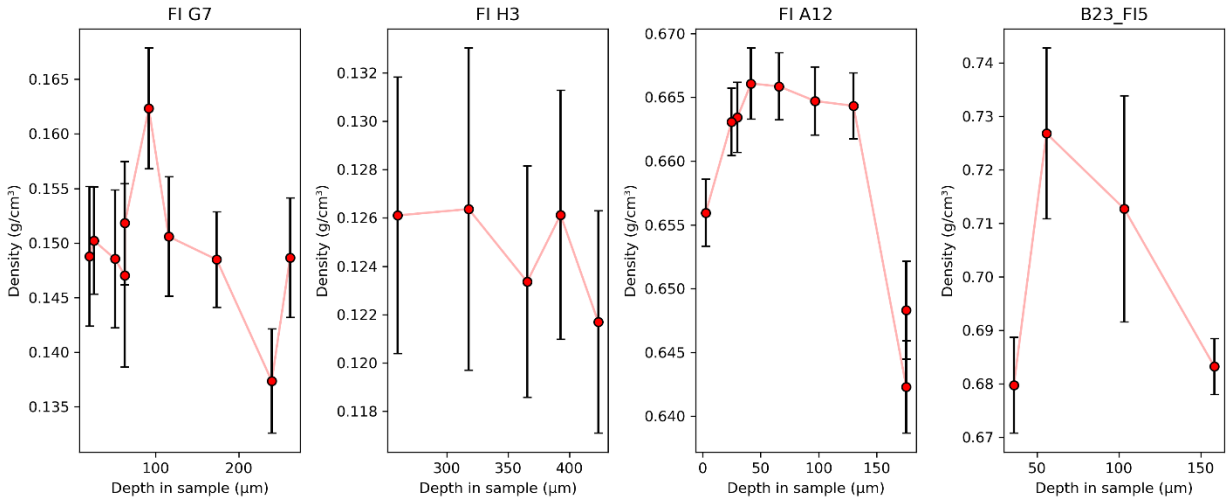

Supporting Figure S40- Density (and error) as a function of depth. The highly variable densities in B23_FI5 likely result from the very poor surface polish, resulting in backgrounds which were tricky to fit.

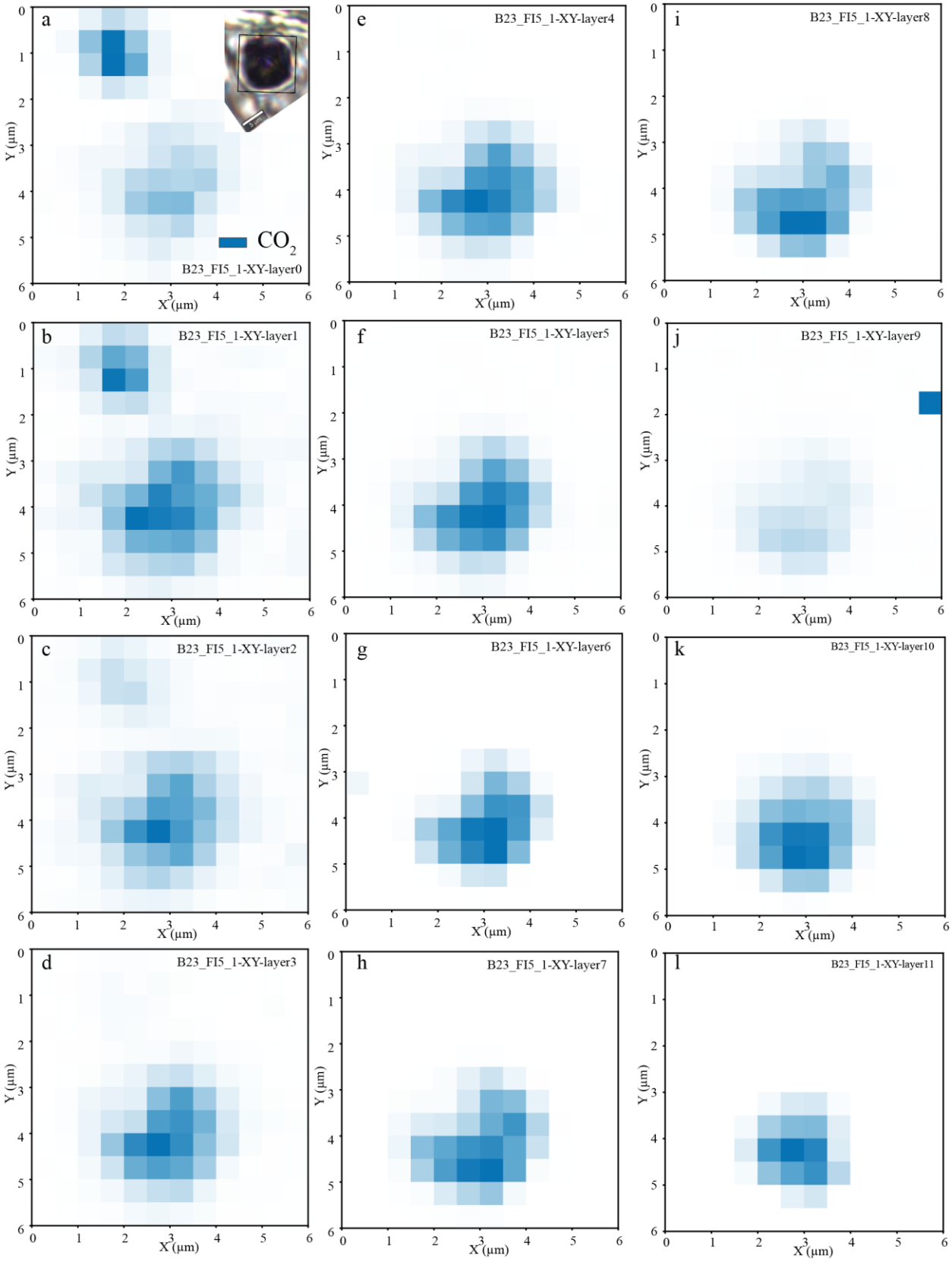
a
B23_FI5_1-XY-layer0
CO2
e
B23_FI5_1-XY-layer4
i
B23_FI5_1-XY-layer8
b
B23_FI5_1-XY-layer1
f
B23_FI5_1-XY-layer5
j
B23_FI5_1-XY-layer9
c
B23_FI5_1-XY-layer2
g
B23_FI5_1-XY-layer6
k
B23_FI5_1-XY-layer10
d
B23_FI5_1-XY-layer3
h
B23_FI5_1-XY-layer7
l
B23_FI5_1-XY-layer11
X (μm)
Y (μm)

355

Supporting Figure S41 – Raman map of CO_2 abundance in B23_FI5_1. The inset in a) shows the geometry of the map relative to the fluid inclusion. Each X-Y graph shows a different Z slice through the inclusion, with the stronger blue colors showing stronger CO_2 intensities. It is clear that the x-y distribution of max intensity varies with depth. The map geometry in the WITec software was set as 12x12x12 um, so each slice was separated by 1 um of stage movement. With the refractive index of olivine being 1.7 and CO_2 being 1, there is some vertical distortion. Maps were collected using 50X objective, with a laser power of 49 mW, an integration time of 1 s, the 1800 grooves/mm grating (so olivine is not visible), and a 1325 cm-1 spectral center. Processing was performed using Ramanspy 0.2.10 (Georgiev et al., 2024). To produce the maps, we first denoise using savitzky golay filter with a window length of 4, and a polynomial of 3rd order, then apply ASLS baseline routine and normalize each spectrum to using Min-Max normalization. We apply the whole preprocessing routine to all the maps. We extract “pure” endmember spectra for CO_2 from the map spectra and use Non-negative Constrained Least Squares (NNLS) abundance method in RamanSpy to extract abundance maps for CO_2 at every pixel. These maps are not quantitative, but an approximation of the distribution of CO_2.

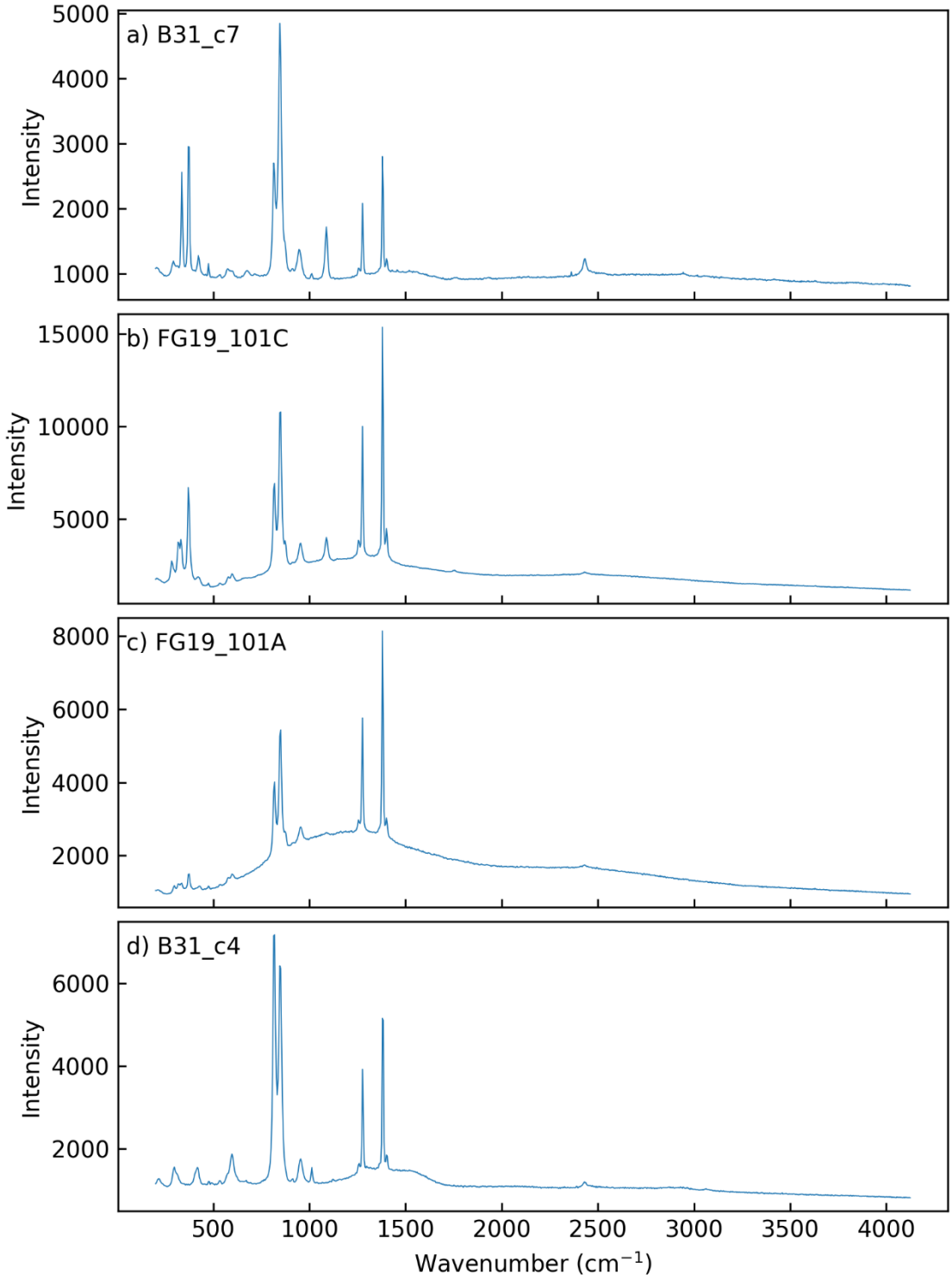

374

375 **Supporting Fig. S42**– 300 g wavelength scans of 4 inclusions targeted for laser heating tests.
376 There is not significant amounts of gas species other than CO2.

377

References

Allison, C.M., Roggensack, K., Clarke, A.B., 2021. Highly explosive basaltic eruptions driven by CO2 exsolution. Nat Commun 12, 217. https://doi.org/10.1038/s41467-020-20354-2

Dayton, K., Gazel, E., Wieser, P., Troll, V.R., Carracedo, J.C., La Madrid, H., Roman, D.C., Ward, J., Aulinas, M., Geiger, H., Deegan, F.M., Gisbert, G., Perez-Torrado, F.J., 2023. Deep magma storage during the 2021 La Palma eruption. Sci. Adv. 9, eade7641. https://doi.org/10.1126/sciadv.ade7641

DeVitre, C.L., Allison, C.M., Gazel, E., 2021. A high-precision CO2 densimeter for Raman spectroscopy using a Fluid Density Calibration Apparatus. Chemical Geology 584, 120522. https://doi.org/10.1016/j.chemgeo.2021.120522

DeVitre, C.L., Wieser, P.E., 2024. Reliability of Raman analyses of CO2-rich fluid inclusions as a geobarometer at Kīlauea. Geochem. Persp. Let. 29, 1–8. https://doi.org/10.7185/geochemlet.2404

Fall, A., Tattitch, B., Bodnar, R.J., 2011. Combined microthermometric and Raman spectroscopic technique to determine the salinity of H2O–CO2–NaCl fluid inclusions based on clathrate melting. Geochimica et Cosmochimica Acta 75, 951–964. https://doi.org/10.1016/j.gca.2010.11.021

Georgiev, D., Pedersen, S.V., Xie, R., Fernández-Galiana, Á., Stevens, M.M., Barahona, M., 2024. RamanSPy: An Open-Source Python Package for Integrative Raman Spectroscopy Data Analysis. Anal. Chem. 96, 8492–8500. https://doi.org/10.1021/acs.analchem.4c00383

Gleeson, M., Wieser, P.E., DeVitre, C.L., Shi, S.C., Millet, M.-A., Muir, D.D., Stock, M.J., Lissenberg, J., 2025. Persistent High-Pressure Magma Storage beneath a Near-Ridge Ocean Island Volcano (Isla Floreana, Galápagos). Journal of Petrology 66, egaf031. https://doi.org/10.1093/petrology/egaf031

Hagiwara, Y., Torimoto, J., Yamamoto, J., 2020. Pressure measurement and detection of small H_2 O amounts in high-pressure H_2 O–CO_2 fluid up to 141 MPa using Fermi diad splits and bandwidths of CO_2. J Raman Spectroscopy 51, 1003–1018. https://doi.org/10.1002/jrs.5865

Hagiwara, Y., Yokokura, L., Yamamoto, J., 2023. Unlocking ultimate precision of intensity and area ratio measurements in Raman spectroscopy: Insights from simulation, experimentation, and theory and implications for isotope ratio analysis. J Raman Spectroscopy 54, 1440–1464. https://doi.org/10.1002/jrs.6594

Hagiwara, Y., Yoshida, K., Yoneda, A., Torimoto, J., Yamamoto, J., 2021. Experimental variable effects on laser heating of inclusions during Raman spectroscopic analysis. Chemical Geology 559, 119928. https://doi.org/10.1016/j.chemgeo.2020.119928

Kawakami, Y., Yamamoto, J., Kagi, H., 2003. Micro-Raman Densimeter for CO_2 Inclusions in Mantle-Derived Minerals. Appl Spectrosc 57, 1333–1339. https://doi.org/10.1366/000370203322554473

Lamadrid, H.M., Moore, L.R., Moncada, D., Rimstidt, J.D., Burruss, R.C., Bodnar, R.J., 2017. Reassessment of the Raman CO 2 densimeter. Chemical Geology 450, 210–222. https://doi.org/10.1016/j.chemgeo.2016.12.034

Le, V.-H., Caumon, M.-C., Tarantola, A., Randi, A., Robert, P., Mullis, J., 2020. Calibration data for simultaneous determination of P-V-X properties of binary and ternary CO2 - CH4 - N2 gas mixtures by Raman spectroscopy over 5–600 bar: Application to natural fluid inclusions. Chemical Geology 552, 119783. https://doi.org/10.1016/j.chemgeo.2020.119783

Le, V.-H., Caumon, M.-C., Tarantola, A., Randi, A., Robert, P., Mullis, J., 2019. Quantitative Measurements of Composition, Pressure, and Density of Microvolumes of CO_2 –N_2 Gas

Mixtures by Raman Spectroscopy. Anal. Chem. 91, 14359–14367. https://doi.org/10.1021/acs.analchem.9b02803

Rosso, K.M., Bodnar, R.J., 1995. Microthermometric and Raman spectroscopic detection limits of C02 in fluid inclusions and the Raman spectroscopic characterization of C02. Geochimica et Cosmochimica Acta 59, 3961–3975. https://doi.org/10.1016/0016-7037(95)94441-H

Song, Y., Chou, I., Hu, W., Robert, B., Lu, W., 2009. CO2 Density-Raman Shift Relation Derived from Synthetic Inclusions in Fused Silica Capillaries and Its Application. Acta Geologica Sinica - English Edition 83, 932–938. https://doi.org/10.1111/j.1755-6724.2009.00090.x

Sublett, D.M., Sendula, E., Lamadrid, H., Steele-MacInnis, M., Spiekermann, G., Burruss, R.C., Bodnar, R.J., 2020. Shift in the Raman symmetric stretching band of N_2 , CO_2 , and CH_4 as a function of temperature, pressure, and density. J Raman Spectroscopy 51, 555–568. https://doi.org/10.1002/jrs.5805

Wang, W., Caumon, M.-C., Tarantola, A., Pironon, J., Lu, W., Huang, Y., 2019. Raman spectroscopic densimeter for pure CO2 and CO2-H2O-NaCl fluid systems over a wide P-T range up to 360 °C and 50 MPa. Chemical Geology 528, 119281. https://doi.org/10.1016/j.chemgeo.2019.119281

Wang, X., Chou, I.-M., Hu, W., Burruss, R.C., Sun, Q., Song, Y., 2011. Raman spectroscopic measurements of CO2 density: Experimental calibration with high-pressure optical cell (HPOC) and fused silica capillary capsule (FSCC) with application to fluid inclusion observations. Geochimica et Cosmochimica Acta 75, 4080–4093. https://doi.org/10.1016/j.gca.2011.04.028

Wieser, P.E., Edmonds, M., Maclennan, J., Jenner, F.E., Kunz, B.E., 2019. Crystal Scavenging from Mush Piles Recorded by Melt Inclusions. Nature Communications.

Wieser, P.E., Lamadrid, H., Maclennan, J., Edmonds, M., Matthews, S., Iacovino, K., Jenner, F.E., Gansecki, C., Trusdell, F., Lee, R.L., Ilyinskaya, E., 2021. Reconstructing Magma Storage Depths for the 2018 Kīlauean Eruption From Melt Inclusion CO_2 Contents: The Importance of Vapor Bubbles. Geochem Geophys Geosyst 22. https://doi.org/10.1029/2020GC009364

Yamamoto, J., Kagi, H., 2006. Extended Micro-Raman Densimeter for CO_2 Applicable to Mantle-originated Fluid Inclusions. Chem. Lett. 35, 610–611. https://doi.org/10.1246/cl.2006.610